EINDHOVEN
UNIVERSITY OF
TECHNOLOGY

Eindhoven University of Technology

MASTER

# Area-selective atomic layer deposition using inhibitor molecules in multi-step cycles

Jongen, Rick G.J.

*Award date:*
2018

Link to publication

**Disclaimer**
This document contains a student thesis (bachelor's or master's), as authored by a student at Eindhoven University of Technology. Student theses are made available in the TU/e repository upon obtaining the required degree. The grade received is not published on the document as presented in the repository. The required complexity or quality of research of student theses may vary by program, and the required minimum study period may vary in duration.

**General rights**
Copyright and moral rights for the publications made accessible in the public portal are retained by the authors and/or other copyright owners and it is a condition of accessing publications that users recognise and abide by the legal requirements associated with these rights.

- Users may download and print one copy of any publication from the public portal for the purpose of private study or research.
- You may not further distribute the material or use it for any profit-making activity or commercial gain

Eindhoven University of Technology

MSC. THESIS

# Area-selective Atomic Layer Deposition using inhibitor molecules in multi-step cycles

R.G.J. Jongen

27 September 2018

PMP 18-07

*Supervisors:*
Ir. M.J.M. Merkx
Dr. ir. A.J.M. Mackus

*Committee:*
Dr. ir. R. W. van der Heijden
Dr. ir. J. H. E. Proll
Prof. dr. ir. W.M.M. Kessels
Dr. ir. A.J.M. Mackus

Eindhoven University of Technology
Department of Applied Physics
Plasma & Materials Processing Group

**Abstract**

Currently, one of the main challenge in the fabrication of microelectronics is the alignment between subsequent patterning steps. In order to mitigate these alignment issues, bottom-up fabrication strategies, such as area-selective atomic layer deposition (ALD) have been gaining a lot of interest. Area-selective ALD aims at deposition on one specific material in the presence of other materials on the same substrate, by exploiting differences in surface chemistry between these materials. The main challenge for area-selective ALD is to increase the selectivity, which means increasing the maximum thickness that can be deposited in an area-selective manner.

In this work, area-selective ALD approaches that employ inhibitor molecules to selectively block ALD precursor adsorption in multi-step ALD cycles are investigated. Specifically, three- and four-step ALD cycles are studied to obtain area-selective ALD of $SiO_2$. A starting point for this project is previous work on area-selective ALD of $SiO_2$ using acetylacetone (Hacac) as the inhibitor (A), bis(diethylamino)silane (BDEAS) as the precursor (B) and an $O_2$ plasma as the co-reactant (C) in ABC-type cycles. The previous work mostly investigated inhibitor of growth on $Al_2O_3$. The goals of this project were: (i) to gain understanding of this area-selective ALD approach in order to improve the selectivity and (ii) to extend this approach to the blocking of deposition on a metallic surface. The most important application for area-selective ALD of $SiO_2$ is the *self-aligned* fabrication of interconnects, where the substrate comprises a metal/dielectric pattern.

For area-selective $SiO_2$ ALD in the presence of $Al_2O_3$ using ABC-type cycles, it was shown that the inhibitor molecules are not completely removed during the $O_2$ plasma exposure. The selectivity of this process was increased by adding a $H_2$ plasma step to the ALD cycle in order to fully remove the inhibitor molecules. For the resulting ABDC-type ALD cycles, ellipsometry showed an increase in nucleation delay from 15 to 30 cycles, which corresponds to area-selective deposition of $\sim$ 2.5 nm. The increased nucleation delay was corroborated using X-ray photoelectron spectroscopy, and quantified using a model based on the Avrami equation.

The knowledge gained from blocking ALD of $SiO_2$ on an $Al_2O_3$ surface was used to extend this approach to the blocking of deposition on a Co surface. During the fabrication of interconnects, the substrate consists of metal/dielectric patterns, where the metal is either Co or Cu. Both ABC-type and ABDC-type ALD of $SiO_2$ have been examined on Co, which resulted in a nucleation delay of 20 and 25 cycles, respectively. Since the ABDC-type ALD recipe include $O_2$ and $H_2$ plasma exposures, oxidation and reduction of the Co has to be taken into account. After more than 25 cycles, SEM images of the Co film showed dewetting, which exposes the underlying silicon substrate. This suggest that the actual nucleation delay might be longer than 25 cycles.

Furthermore, area-selective ALD of $Al_2O_3$ was investigated, which could be used to selectively deposit an etch stop layer. This etch stop layer protects the deposited barriers ($SiO_2$) from subsequent etching steps. Two different inhibitor molecules (acetylacetone and vinylphosphonic acid) were tested, showing adsorption on Co and $Al_2O_3$ but not on $SiO_2$. However, since the inhibitors did not completely block the subsequent TMA adsorption on Co, it was not possible to achieve area-selective ALD as desired. Altogether, these experiments afforded some useful knowledge and provided inspiration for future research.

# Contents

**1 Introduction** **5**
1.1 Patterning . . . 5
1.2 Atomic layer deposition . . . 7
1.3 Area-selective ALD . . . 9
1.4 Area-selective ALD using inhibitor molecules . . . 12
1.5 Application of area-selective ALD . . . 12
1.6 Goals . . . 17

**2 Methodology** **19**
2.1 Reactors . . . 19
2.1.1 FlexAL reactor . . . 19
2.1.2 ALD-I reactor . . . 21
2.2 ALD cyles . . . 22
2.3 Ellipsometry . . . 23
2.3.1 Ellipsometry modelling . . . 24
2.3.2 Modelling the nucleation for area-selective ALD . . . 25
2.4 FTIR . . . 28
2.5 Ex situ diagnostics . . . 30
2.5.1 XPS . . . 30
2.5.2 Atomic force microscopy . . . 32
2.5.3 Scanning electron microscopy . . . 32

**3 Review of previous work: Area-selective ALD of $SiO_2$ using ABC-type cycles** **33**
3.1 Area-selective ALD using ABC-type cycles . . . 33
3.2 Subcycle experiments . . . 35
3.3 Fourier transform infrared spectroscopy . . . 37
3.4 DFT calculations . . . 38
3.5 Open questions . . . 39

**4 Improving area-selective ALD of $SiO_2$ in the presence of $Al_2O_3$ using ABDC-type cycles** **41**
4.1 Removal of adsorbed acac species . . . 41
4.2 Improving the selectivity of $SiO_2$ ALD by using a four-step cycle . . . 44
4.2.1 Subcycle experiments on ABDC-type ALD cycles . . . 44
4.2.2 Determining the nucleation delay with *in situ* ellipsometry . . . 47

4.2.3 XPS corroboration of the nucleation delay . . . 50
4.3 Conclusion . . . 51

**5 Area-selective ALD of $SiO_2$ in the presence of Co 53**
5.1 Area-selective ALD of $SiO_2$ in the presence of oxidized cobalt . . . 54
5.2 Area-selective ALD of $SiO_2$ in the presence of reduced cobalt . . . 57
5.3 Oxidation and reduction of the cobalt substrate during ABDC-type ALD . . 59
5.3.1 AFM . . . 60
5.3.2 SEM . . . 61
5.4 Conclusion . . . 62

**6 Area-selective ALD of $Al_2O_3$ on $SiO_2$ in the presence of Co 65**
6.1 Selection of the inhibitor . . . 65
6.2 Investigating Hacac as the inhibitor for area-selective ALD of $Al_2O_3$ . . . 67
6.3 Delaying nucleation of $Al_3O_3$ ALD by on Co by using VPA as the inhibitor . 69
6.4 Conclusion and outlook . . . 71

**7 Conclusion and outlook 73**
7.1 Conclusion . . . 73
7.2 Outlook . . . 74
7.2.1 Reduction of oxidized cobalt . . . 74
7.2.2 Eliminate dewetting of Co substrates for ABDC-type ALD cycles . . . 75
7.2.3 Combining ALD and ALE to reset the nucleation delay . . . 76
7.2.4 Alternating complementary area-selective ALD schemes . . . 77

**Acknowledgements 79**

**A Precursors and inhibitors 89**

**B XPS Si 2p peak reference for $SiO_2$ deposition 91**

**C Characterization of the cobalt substrate 93**

**D Saturation of the $O_2$ plasma exposure for ALD of $SiO_2$ 95**

# Chapter 1

# Introduction

As the semiconductor industry advances to smaller and smaller features, new challenges in integrated circuit (IC) fabrication arise. To fabricate multilayer ICs, a large number of deposition, lithography and etching steps is required. Currently, the key challenge in downscaling is the alignment for each sequential patterning step.[1] In order to avert these alignment issues, the industry is trying to complement traditional top-down fabrication schemes with bottom-up approaches. Bottom-up fabrication can be achieved using area-selective atomic layer deposition (ALD). Next to mitigating the alignment issues, area-selective ALD can also reduce the number of processing steps in semiconductor fabrication.[2]

This chapter introduces the conventional patterning approach, and discusses the current issues of this approach with respect to downscaling. Furthermore, ALD and area-selective ALD are introduced, and the goals of this work are stated.

## 1.1 Patterning

For microelectronics, patterned structures consisting of a multilayer stack of various materials are needed. Figure 1.1 shows an example of a patterned structure from the semiconductor industry. On the bottom, the individual transistors are fabricated on a silicon wafer. On top of that, a stack of layers of wiring are deposited, to connect these individual parts into an integrated circuit (IC). The big feature on the top left, is where the connection to a physical wire can be attached.

Conventionally, a uniform film of material is deposited, which is subsequently patterned using several patterning steps. The process flow for conventional top-down patterning, is shown in figure 1.2. In the conventional patterning process, a full layer of material is first deposited. Then the substrate is coated with a photoresist, which is a photo-active layer that is patterned using lithography. Subsequently, the printed pattern is transferred to the material deposited in the first step by etching. After transferring the pattern to the layer of material, the residual resist layer is chemically removed.

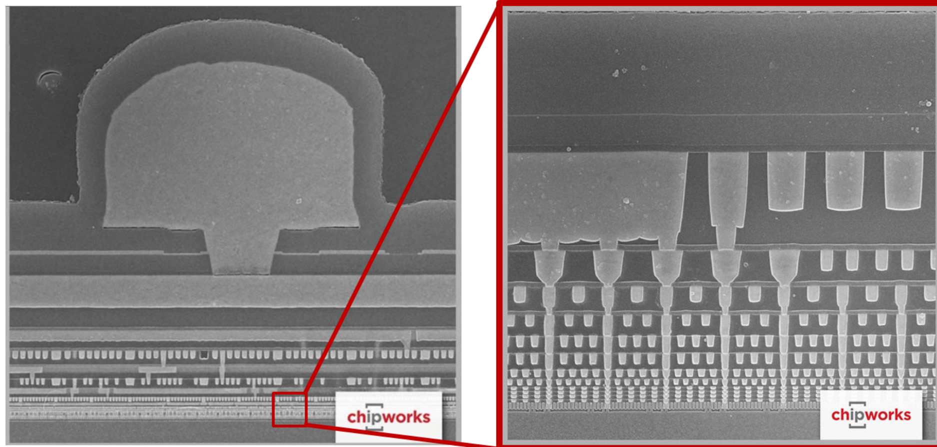


**Figure 1.1:** Cross-section of an Intel 14-nm chip with 13 metal layers, showing multilayer patterns needed in IC fabrication.[3] These metal layers are used to connect individual devices (at the bottom), forming an integrated circuit.

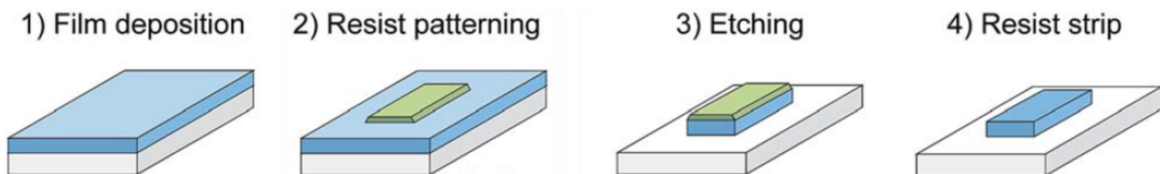


**Figure 1.2:** Process flow for conventional patterning based on etching.[2] A film is deposited, which is coated with photoresist. Next, the photoresist layer is patterned using lithography. The pattern is transferred using an etching step, which, after removal of the remaining resistive layer, gives the desired pattern.

The number of processing steps to form an IC increases with every new generation of technology.[4] Each step can introduce errors, resulting in differences between the designed integrated circuit and the fabricated one. Especially alignment between subsequent patterning steps has become increasingly difficult, resulting in so-called edge placement errors (EPEs). Figure 1.3 shows a TEM cross-section of an 'Intel 3D Xpoint' memory chip, where EPEs are visible. EPEs affect device performance, and can even cause shorts between two neighbouring metal lines inducing device failure.[5] Advanced deposition techniques (such as area-selective ALD) can potentially enable self-aligned processing, and thereby mitigate alignment issues as explained in section 1.5.

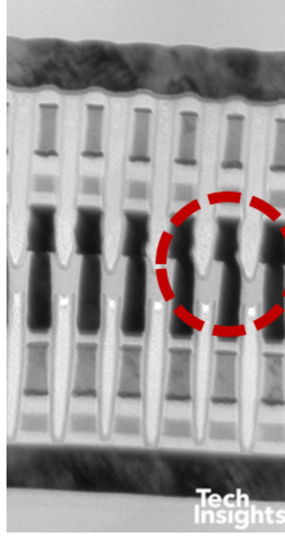


**Figure 1.3:** TEM cross-section of Intel X-point Memory Array showing EPEs. The EPEs (circled in red) are caused by misalignment between subsequent patterning steps.[6]

## 1.2 Atomic layer deposition

Atomic layer deposition (ALD) is a vapour-phase deposition technique used to grow high-quality thin films with high uniformity, high conformality and atomic-level control of thickness.[7] ALD is a cyclic process which consists of at least two sequential self-limiting half-cycles, made up of either the precursor or the co-reactant dose, and a purge step. In this research, processes for ALD of $Al_2O_3$ and $SiO_2$ are investigated. Therefore, the characteristics of ALD are explained on the basis of these two processes.

A schematic representation of ALD of $Al_2O_3$ is given in figure 1.4. For this process, typically $Al(CH_3)_3$ (trimethylaluminium or TMA, see appendix A) is used as the precursor and $H_2O$ as the co-reactant. The half-cycle reactions are given in equations 1.1 and 1.2:

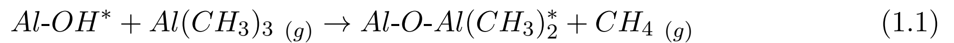

$$Al\text{-}OH^* + Al(CH_3)_3\ _{(g)} \rightarrow Al\text{-}O\text{-}Al(CH_3)_2^* + CH_4\ _{(g)} \tag{1.1}$$

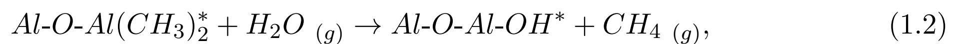

$$Al\text{-}O\text{-}Al(CH_3)_2^* + H_2O\ _{(g)} \rightarrow Al\text{-}O\text{-}Al\text{-}OH^* + CH_4\ _{(g)}, \tag{1.2}$$

where the asterisk indicates surface species.

In the first half-reaction, the TMA precursor molecules react with -OH groups on the surface. The methyl ligands from the precursor react with -OH groups forming Al-O bonds, and $CH_4$ is produced as a volatile by-product. After this half-cycle, the surface is terminated by $-CH_3$ groups, preventing the adsorption of more precursor molecules, which makes this half-reaction self-limiting. A purge step is used to remove both excessive gas-phase precursor molecules and the volatile by-products formed. In the subsequent step, the co-reactant ($H_2O$) is dosed. When the $-CH_3$ surface groups are exposed to $H_2O$, the $H_2O$ molecules adsorb on the surface, reacting with the $-CH_3$ groups and forming new -OH groups. Again, $CH_4$ is formed as a

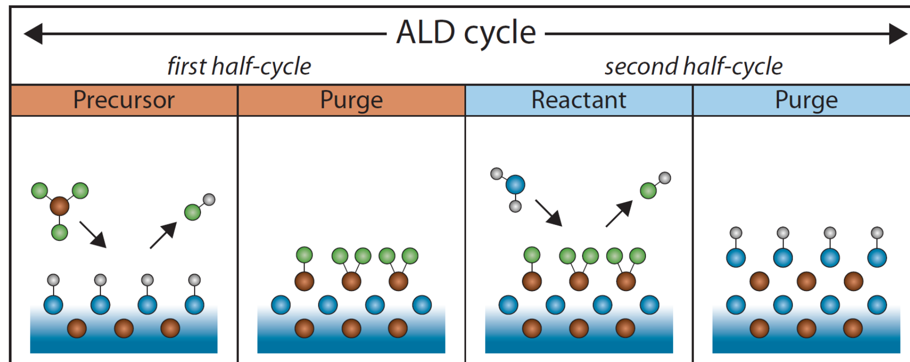


**Figure 1.4:** Schematic representation of the ALD process for $Al_2O_3$. Precursor and co-reactant pulses are alternated, combining two self-limiting surface reactions to obtain ALD. The exposures of precursor and co-reactant are seperated by purge steps to prevent gas-phase reactions.[8]

volatile by-product. Since this reaction ceases when all the -$CH_3$ groups are removed from the surface, this reaction is also self-limiting.

By combining two self-limiting surface reactions into a cyclic process, ALD allows for sub-monolayer thickness control of the deposited material. Additionally, this also means that the films grow very uniformly, are deposited with high conformality on demanding (e.g. high aspect ratio) topologies.[7,9] These three characterizing features are illustrated in figure 1.5.

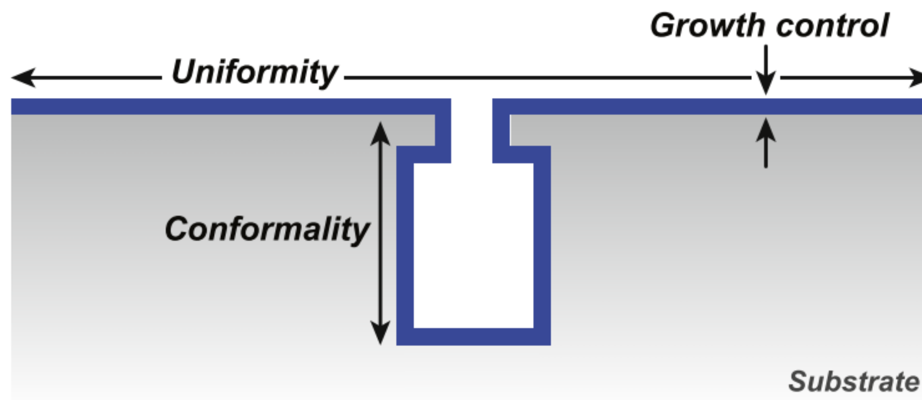


**Figure 1.5:** Illustration of ALD growth on a substrate with demanding topology. Three key features of ALD (high uniformity, high conformality and accurate growth control) are indicated.[10]

Aside from so-called thermal ALD (which uses heat energy for chemical reactions to deposit films) as described above, it is also possible to use a plasma as the co-reactant. This technique is called plasma-assisted ALD, and has several advantages over thermal ALD. For example, the high reactivity of the plasma species allows for more freedom in processing conditions and for a wider range of material properties.[11]

In addition to thermal ALD of $Al_2O_3$, plasma-assisted ALD of $SiO_2$ has been studied in this research. The process used to deposit $SiO_2$ was reported previously by Dingemans *et al.*[12] Although thermal ALD processes are available for $SiO_2$ ALD, these require relatively high substrate temperatures (600 K).[13] In the plasma-assisted ALD process of $SiO_2$, $H_2Si[N(C_2H_5)_2]_2$ (bisdiethylamino silane or BDEAS) is used as the precursor, and the co-reactant is an $O_2$ plasma exposure. The structural formula of BDEAS is shown in figure 2.4 A. The proposed chemical half-cycle reactions are given in equations 1.3 and 1.4:

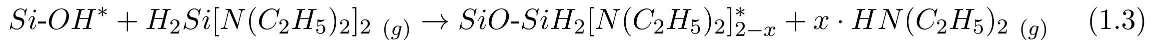

$$Si\text{-}OH^* + H_2Si[N(C_2H_5)_2]_{2\ (g)} \rightarrow SiO\text{-}SiH_2[N(C_2H_5)_2]^*_{2-x} + x \cdot HN(C_2H_5)_{2\ (g)} \quad (1.3)$$

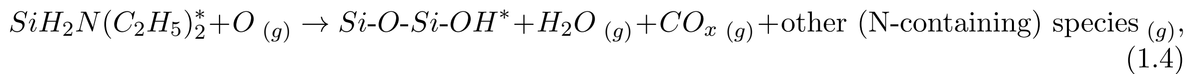

$$SiH_2N(C_2H_5)^*_2 + O_{\ (g)} \rightarrow Si\text{-}O\text{-}Si\text{-}OH^* + H_2O_{\ (g)} + CO_{x\ (g)} + \text{other (N-containing) species}_{\ (g)}, \quad (1.4)$$

where the asterisk indicates surface species. In reaction 1.3, either only one (x=1) or both (x=2) of the precursor ligands may react.

During the precursor step, it is most likely that the precursor ligands react with -OH groups on the surface, producing volatile $HN(C_2H_5)_2$. In the second half cycle, the surface reactions involve O radicals delivered by the plasma. As observed for other ALD processes,[14] the $O_2$ plasma combusts the precursor ligands and forms -OH surface groups.

## 1.3 Area-selective ALD

In addition to the precise control of the layer thickness of ALD, there is growing interest in controlling the lateral dimensions of the deposited material by an area-selective ALD process.[15] Area-selective ALD is based on the fact that ALD heavily relies on the surface chemistry of the substrate. For metal-oxides for example, ALD nucleation starts in most cases readily on an OH-terminated surface, while there is a short nucleation delay on hydrogen-terminated[16,17] or metal surfaces.[18] Considering a starting surface consisting of two materials, the material on which deposition should take place is referred to as the growth area and the material on which no deposition should take place is referred to as the non-growth area. Using the differences in surface chemistry, ALD nucleation may be delayed exclusively on the non-growth area, achieving area-selective ALD (as shown in figure 1.6.) However, at some point the growth initiates on the non-growth area, causing a loss of selectivity. Here, the selectivity ($S$) is defined as:

$$S = \frac{\theta_1 - \theta_2}{\theta_1 + \theta_2} \quad (1.5)$$

where $\theta_1$ is the amount of deposited material on the growth area, and $\theta_2$ is the amount of deposited material on the non-growth area.[19] One of the challenges of area-selective ALD is to delay the nucleation on the non-growth area as long as possible.

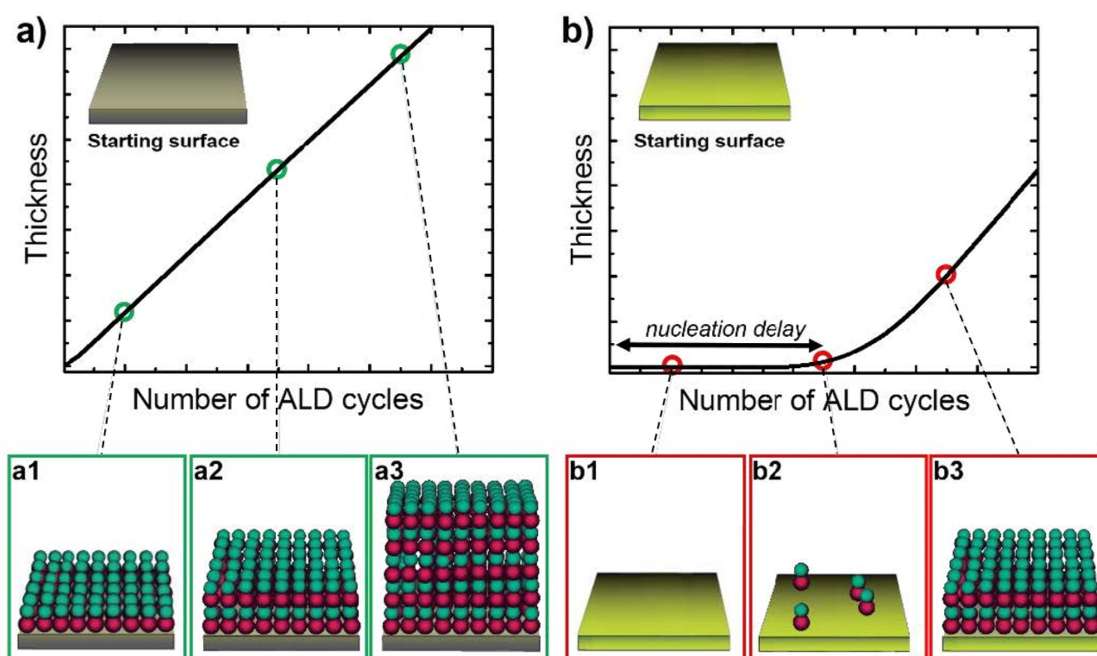


**Figure 1.6:** Schematic illustration of the film thickness as a function of the number of ALD cycles on two different starting surfaces. Performing ALD cycles results in a) immediate and linear film thickness increase or b) a nucleation delay. Pictures a1-a3) and b1-b3) schematically illustrate three different stages of the film deposition on the respective starting surfaces.[20]

Figure 1.6 shows the film thickness as a function of the number of ALD cycles for both the growth area (a) and the non-growth area (b).[20] On the growth area, a linear thickness increase with the number of ALD cycles indicates immediate film nucleation on the starting surface, resulting in controlled layer-by-layer deposition of the desired material. On the non-growth area, film deposition is delayed for several ALD cycles. During this nucleation delay, ideally the starting surface remains free from nucleation sites. However, typically selectivity breaks down after a certain number of ALD cycles. Deposition starts at some point due to for instance nucleation on defect sites or uncontrolled changes (e.g. oxidation, precursor physisorption) of the surface due to the ALD process. After the nucleation delay, and once the surface is fully covered by the deposited material, the thickness of deposited material should increase linearly with the number of cycles, producing a constant GPC. The difference between the nucleation delays on the non-growth and growth areas in terms of the number of cycles is defined as the selectivity window. In order to maximize the selectivity, it is essential to extend the nucleation delay, increasing the amount of material deposited on the growth surface before nucleation occurs on the non-growth surface.[21]

The differences in surface chemistry used to achieve area-selective ALD can either be intrinsic, or induced. Area-selective ALD can be achieved by choosing a precursor or co-reactant that inherently adsorbs selectively on certain surfaces. This has been done by for example Tao *et al.*, who selectively deposited $HfO_2$ on Si in the presence of Cu.[18] However, the possible

combinations of substrates and precursors are very limited using inherent selectivity. A solution to this limitation is inducing area-selective ALD. Induced area-selective ALD can be achieved by chemically modifying the surface, deactivating the non-growth area.[22,23] So far, most of the area-selective ALD studies reported on area-deactivation using self-assembled monolayers (SAMs).

SAMs are organic monolayer films that form spontaneously on solid surfaces and are used to modify the properties of these surfaces.[24] SAM monomers usually consist of a headgroup that selectively adsorbs on the non-growth area, a long alkyl-chain to form an ordened SAM though van der Waals interactions and a non-reactive tail group to block precursor adsorption. One example of area-selective ALD using SAMs is the work done by Hashemi *et al.*, who showed area-selective ALD on metal-dielectric patterns.[25] As depicted in figure 1.7, a molecule with a long alkyl chain and a phosphonic acid headgroup (octadecylphosphonic acid) was used to form a SAM. The molecule adsorbs selectively on Cu in the presence of $SiO_2$. After deactivation of the surface with the SAM, ZnO was deposited using ALD. The SAM blocks precursor adsorption and therefore selective deposition on the $SiO_2$ surface is achieved.

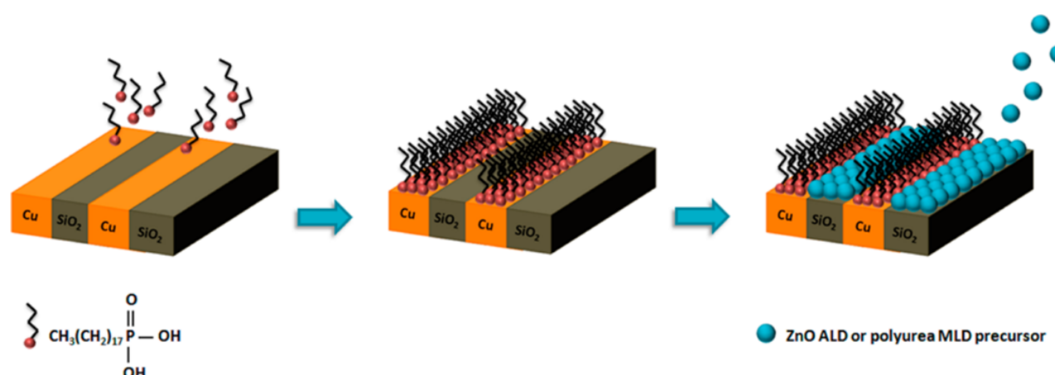


**Figure 1.7:** Schematic illustration of an area-selective ALD approach based on the use of SAMs.[25] The SAM adsorbs selectively on the metal surface, and locally blocks precursor adsorption in the subsequent ALD process.

Although SAMs have shown good results in obtaining area-selective ALD, there are some key disadvantages. Firstly, forming a well-packed SAM either by immersion of the sample in a solution or by vapor deposition, generally takes more than 24 hours.[23,26,27] When the SAM preparation is too short, the density of the SAM is too low resulting in defects where deposition can take place. Secondly, SAMs are susceptible to degradation. Degradation of the SAM occurs when exposed to plasma or ozone gas.[28] Therefore, plasma-assisted and ozone-based ALD processes can generally not be used for area-selective ALD using SAMs. Moreover, SAMs are not compatible with high temperatures (most SAMs are only thermally stable up to 100 °C.) Taken together, SAMs have shown good results in obtaining area-selective ALD, but the limited compatibility with ALD processes and the long formation time make this technique not easily applicable in the microelectronic industry.

## 1.4 Area-selective ALD using inhibitor molecules

Recently, a new approach for area-selective ALD was introduced in our research group by Mameli *et al.*[29] In this approach, small molecules are used as inhibitors in order to achieve area-selective ALD by area-deactivation. The process uses ABC-type ALD cycles, where the inhibitor is dosed during every cycle. Since this work is a follow-up on that research, some elaboration is given in this section, while a more detailed description is given in chapter 3.

Area-selective ALD was demonstrated using acetylacetone (Hacac) as the inhibitor (A), bis(diethylamino)silane (BDEAS) as the precursor (B) and an $O_2$ plasma exposure as the co-reactant (C). A schematic of this process is given in section 3.1. The process relies on chemoselective adsorption of the inhibitor on the non-growth area, where the adsorbed inhibitor subsequently blocks the precursor adsorption. A nucleation delay of approximately 15 cycles was achieved, which corresponds to $\sim$ 1 nm of selective deposition. This was corroborated in detail by *in situ* ellipsometry and infrared spectroscopy experiments as well as by density functional theorem (DFT) calculations, which will be shown in chapter 3.

Using inhibitor molecules, the non-growth area is chemically deactivated for precursor adsorption. In principle, this is similar to SAMs, but with a few differences. The key difference between area-selective ALD using inhibitor molecules and SAMs is apparent from the dosing sequence. Where a SAM is formed before deposition, inhibitor molecules are dosed in ABC-type cycles. By reapplying the inhibitor molecules during every cycle, degradation of the inhibiting layer is not an issue. This increases the compatibility of area-selective deposition with different ALD recipes. Furthermore, inhibitor molecules are usually small and volatile. Therefore, the inhibitors can be dosed in vapor-phase, forming a complete inhibiting layer in the order of seconds. In conclusion, obtaining area-selective ALD using inhibitors instead of SAMs is less time-consuming and compatible with more ALD processes. Overall, this increases the range of possible applications of area-selective ALD.

## 1.5 Application of area-selective ALD

$SiO_2$ was proven to be useful in integrated circuits, and is currently employed in field-effect transistors, capacitors and memory devices.[30–32] Traditionally, $SiO_2$ has been used as a gate dielectric, but due to increasingly straining material requirements it has been replaced with high-k materials. Nowadays, $SiO_2$ is used as spacer and liner material between conducting materials, acting as a barrier that isolates the conducting material in the layer stack.

The application of area-selective ALD of $SiO_2$ that is considered in this research is the mitigation of alignment issues in the back-end-of-line (BEOL.) Figure 1.8 shows a schematic cross-section of an integrated circuit. The front-end-of-line (FEOL) and back-end-of-line (BEOL) are indicated.

The FEOL, indicated at the bottom, is where the individual devices (e.g. transistors) are present. On top of that, in the BEOL, the individual devices are connected through Cu or Co wiring. This wiring is used to connect the individual transistors, forming an integrated circuit. Moreover, the transistors are thereby brought in contact to the physical connections, depicted as the back-end. The BEOL consists of layers of horizontal metal lines, connected

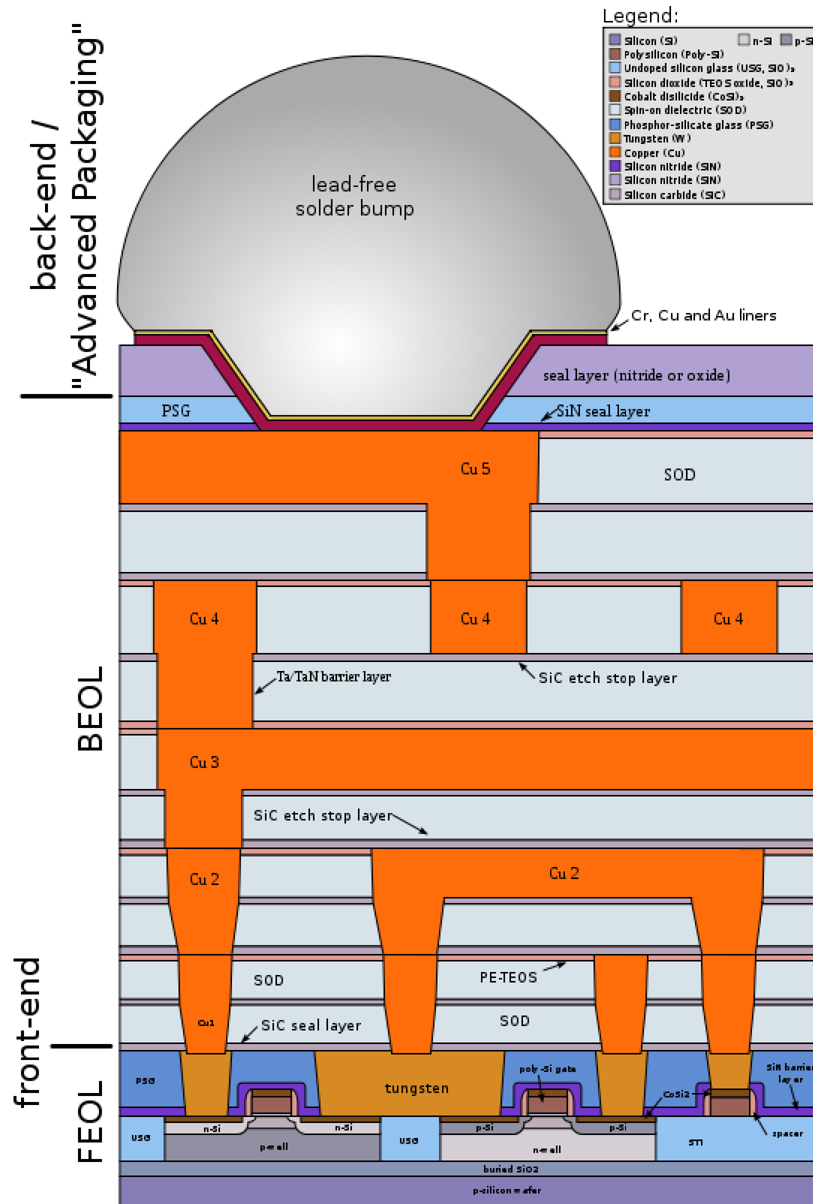


**Figure 1.8:** Schematic of a cross-section of an IC, showing from the bottom up the individual devices in the FEOL, connected though layers of wiring in the BEOL to the physical connections in the back-end.[33]

vertically through layers of interconnects. For every layer in the BEOL, multiple patterning steps are needed to form either the metal lines or the interconnects between the layers. The connections between two metal lines in different levels are called vertical interconnect accesses (VIAs).

Since the individual transistors are becoming smaller and smaller, the wiring in the BEOL turns out more densely packed. Smaller and more closely-packed metal lines require more precise alignment of the VIA, which makes alignment between subsequent patterning processes

increasingly challenging with the current patterning techniques.[22,34] In order to mitigate these alignment issues, self-aligned processes such as area-selective deposition and selective etching can provide vital solutions. One application of area-selective ALD of $SiO_2$ to mitigate alignment issues in the BEOL, is self-aligned VIAs.

Figure 1.9 gives a schematic of current alignment issues in VIA fabrication (A-C) and how this can be mitigated using area-selective deposition (D-F). Before VIA fabrication (A), the surface consist of a pattern of conducting metal lines (e.g. Cu or Co) separated by dielectric barriers. When the VIA is fabricated in the subsequent layer, the desired result is that the VIA is in perfect alignment with the underlying line (figure 1.9 B) to maximize the contact area and to prevent shorts to a neighbouring line. However, in practice, alignment is not perfect, defining an edge placement error (EPE) between the desired position and the actual position (C). Due to this EPE, the contact area between the line and the VIA is smaller, causing an increase in resistance. Also, the VIA is closer to the neighbouring line, causing an increase in capacitance. The increased resistance and capacitance cause a so-called RC-delay, which affects both device performance and efficiency. If the dielectric barrier between a VIA and a neighbouring trench is too small, the EPE can even result in a short, causing the device to fail. Figure 1.10 shows a TEM image of a VIA with an EPE, where the dielectric between the VIA and the neighbouring trench is too thin such that it can cause a short.

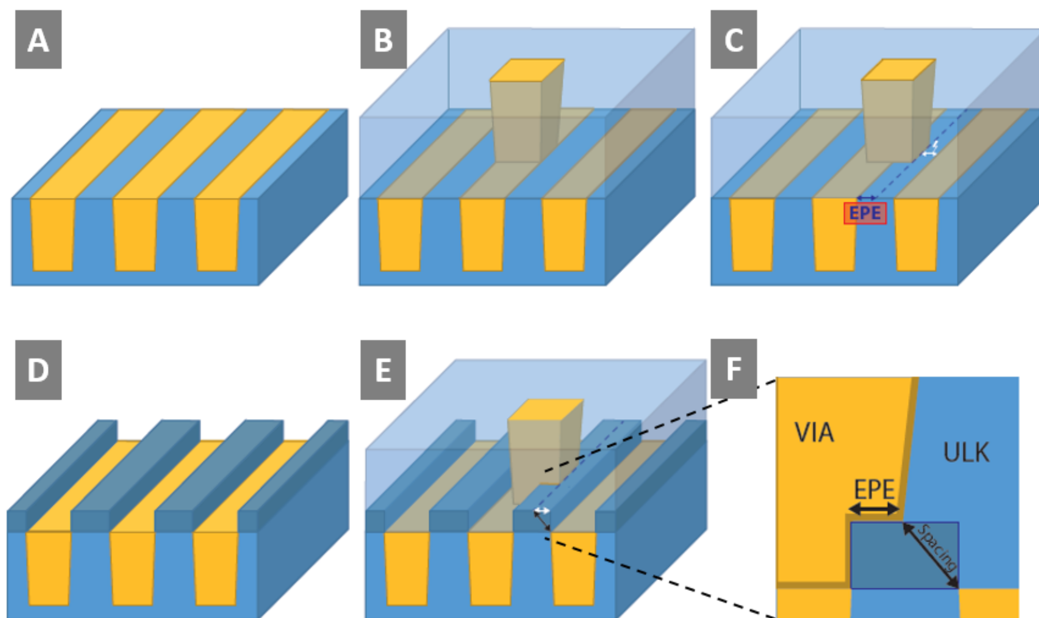


**Figure 1.9:** (Top) schematic of issues in VIA alignment, (bottom) the proposed solution . (A) Starting surface consisting of a pattern of metal lines and dielectric spacing. (B) Desired position of the VIA. (C) Difference in desired and actual position due to alignment issues, defining the EPE. (D) Dielectric barriers deposited in an area-selective manner. (E) VIA is fabricated with the same EPE as before. (F) Additional spacing to the neighbouring line provided by the dielectric barriers, thereby preventing possible shorts.

The bottom part of figure 1.9 shows how area-selective ALD could mitigate this problem. Area-selective deposition of dielectric-on-dielectric in the presence of Cu/Co as the non-growth area, could create an additional dielectric barrier to a neighbouring line (D). Even if the

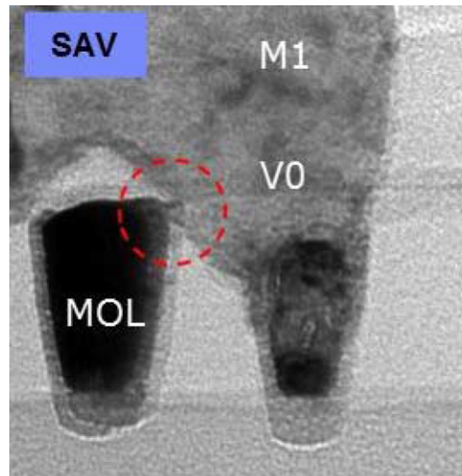


**Figure 1.10:** TEM image of a VIA fabricated with an EPE. The VIA (V0) is in contact with the neighbouring metal line, which can cause a short.[35]

VIA is patterned with the same EPE as before (E), the topography of the surface provides an additional physical barrier between the conducting trenches (F). This allows for larger EPEs without significantly influencing the RC-delay. Currently, a selective recess etch of the conducting material is used to form a similar topography. The recess etch is achieved by oxidizing the Cu using a $H_2O_2$-containing solution, and the oxidized Cu is etched with a HF-based solution.[5,36] Although this process is able to form the desired structure similar to figure 1.9D, atomic level control of thickness is no achieved by using wet-chemical processes. Moreover, using wet etches is not scalable for device fabrication in industry. Therefore, using either an atomic layer etch or ALD process, would improve thickness control.

Next to area-selective ALD of $SiO_2$, this work also focuses on area-selective ALD of $Al_2O_3$. Area-selective ALD of $Al_2O_3$ could be used in self-aligned VIA fabrication as an etch stop layer. The process flow for VIA fabrication using a recess etch is depicted in figure 1.11. During the VIA fabrication process, after the formation of the dielectric barriers by recess etch, a layer of dielectric material is deposited on top of the entire structure. The dielectric layer usually consists of $SiO_2$ with carbon contaminants, also known as carbon doped oxide (CDO). The subsequent formation of the VIAs is achieved by etching the CDO layer. When etching through this CDO, the barriers formed by recess etch are also etched.

To prevent etching of the selectively deposited barriers, an etch contrast between the barriers and the CDO is needed. Currently, an etch stop layer is uniformly deposited on top of the selectively deposited barrier structure. After etching of the VIA, the exposed parts of the etch stop layer are removed using wet chemistry. In order to avoid these wet chemistry processes, area-selective ALD of an etch stop layer on the dielectric in the presence of the metal lines (either Cu or Co) could present a solution. The desired topography achieved by combining the two area-selective processes, is given in figure 1.12. $Al_2O_3$ can be used as a area-selectively deposited barrier layer, with the added benefit that it has an etch contrast with respect to CDO deposited in the subsequent fabrication steps. Therefore, area-selective deposition of $Al_2O_3$ in the presence of Co is investigated.

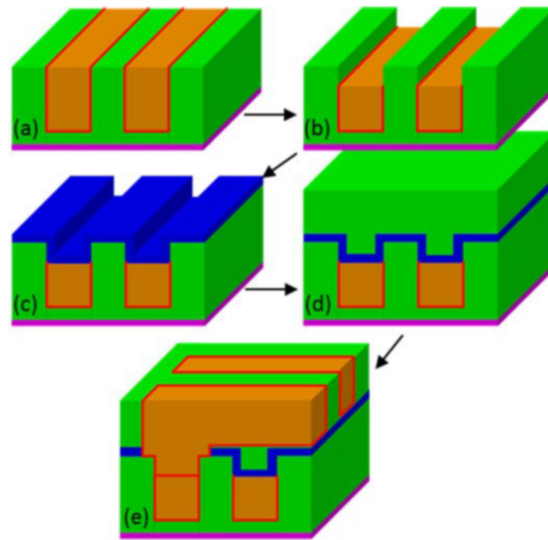


**Figure 1.11:** Schematic process flow for VIA fabrication using a recess etch. (a) Metal - dielectric starting surface, (b) selective recess etch of metal, (c) uniform deposition of the etch stop layer, (d) deposition of the subsequent CDO and (e) the VIA is fabricated using a process to etch the CDO.[35]

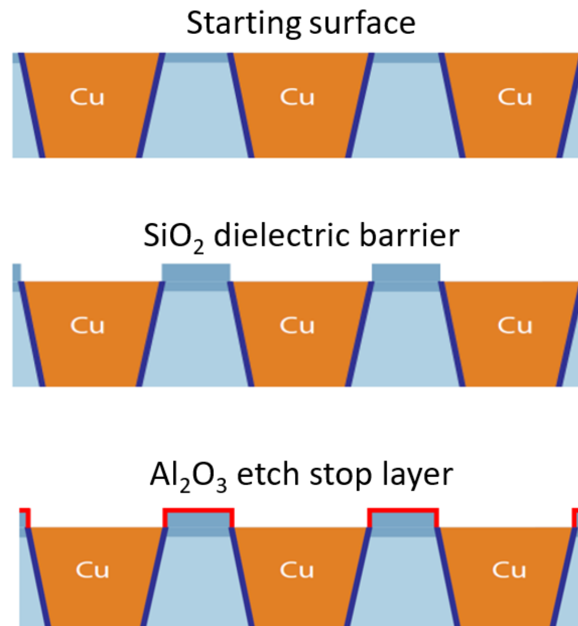


**Figure 1.12:** Schematic of formation of the desired topography by combining two area-selective processes. First, area-selective ALD of $SiO_2$ is used to selectively grow dielectric barrier layers to mitigate alignment issues in VIA fabrication. Secondly, area-selective ALD of $Al_2O_3$ is used to apply an etch stop layer, in order to protect the selectively deposited barrier during subsequent CDO etch.

## 1.6 Goals

The main goal of this research project was to develop processes for area-selective ALD of $SiO_2$ and $Al_2O_3$. These processes can for example be used to selectively deposit barriers to mitigate EPEs in VIA alignment. Three separate research goals are defined, which correspond to chapter 4, 5 and 6 respectively.

Firstly, in order to gain more insight into area-selective ALD of $SiO_2$ in the presence of $Al_2O_3$, the process using inhibitors in ABC-type cycles is investigated. The goal is to obtain fundamental understanding of the surface reactions during the ABC-type cyclesin order to improve the selectivity as far as possible. Since most of the previous work on this process was studied on $Al_2O_3$ as non-growth area, it is convenient to examine this area-selective ALD process on this substrate first.

Secondly, the knowledge gained from the research on $Al_2O_3$ is transferred to Co. For the application of self-aligned VIAs, the starting surface consists of metal / dielectric patterns. Currently, Co or Cu is mostly used for VIAs in the industry. The key goal is to selectively deposited dielectric material ($SiO_2$) on dielectric material without depositing on the metal non-growth area. This work focuses on delaying $SiO_2$ ALD nucleation on Co.

Thirdly, area-selective ALD of $Al_2O_3$ is investigated. As explained in section 1.5, $Al_2O_3$ can be used as an dielectric barrier, with the added benefit that it provides an etch contrast for subsequent patterning steps. Therefore, area-selective ALD of $Al_2O_3$ on $SiO_2$ in the presence of Co was investigated.

In summary, the goals of this research can be given in three research questions. The results presented in this thesis are separated into three chapter, reflecting these three questions:

1. *Can we improve the selectivity of area-selective ALD of $SiO_2$ using ABC-type cycles with Hacac as the inhibitor on $SiO_2$ with $Al_2O_3$ as the non-growth area?*

2. *Can we achieve area-selective ALD of $SiO_2$ with Co as the non-growth area?*

3. *Can we design a process for area-selective ALD of $Al_2O_3$ with Co as the non-growth area?*

# Chapter 2

# Methodology

In this chapter, the experimental details of the conducted research are described. The ALD reactors are discussed, as well as the employed ALD recipes. Furthermore, the used diagnostics are explained, and a model is presented to quantify the experimentally obtained nucleation delay.

## 2.1 Reactors

The measurements presented in this research was conducted on two ALD reactors. Firstly, an Oxford Instruments FlexAL reactor equipped with *in situ* spectroscopic ellipsometry (SE) has been used to study ALD nucleation on different substrates. Secondly, a home-built ALD reactor (referred to as ALDi) equipped with *in situ* Fourier transform infrared spectroscopy (FTIR) has been used to investigate the surface reactions that occur during ALD.

### 2.1.1 FlexAL reactor

A schematic of the FlexAL reactor is given in figure 2.1. The reactor consists of a deposition chamber to which a turbomolecular pump (backed up by a roughing pump), an ICP plasma source and a load lock are connected through gate valves.

The chamber is equipped with a heating stage, to be able to control the temperature of the sample between 25 and 400 °C. In the experiments conducted, the table temperature was set to 150 °C. In order to prevent condensation of precursor and co-reactant molecules in cold spots, the reactor walls and gas lines were heated to 100 °C. The base pressure in the deposition chamber is approximately $10^{-6}$ mbar. The pressure in the chamber during processing is regulated using an automated pressure controller (APC), which is a butterfly valve that automatically opens and closes to either decrease or increase the pressure in the chamber.

Plasmas are generated by an inductively coupled plasma source (ICP). The plasma is produced with a radiofrequency (RF) signal at 13.56 MHz, while an automated matching network ensures efficient coupling of the RF power into the plasma. The plasma characteristics can

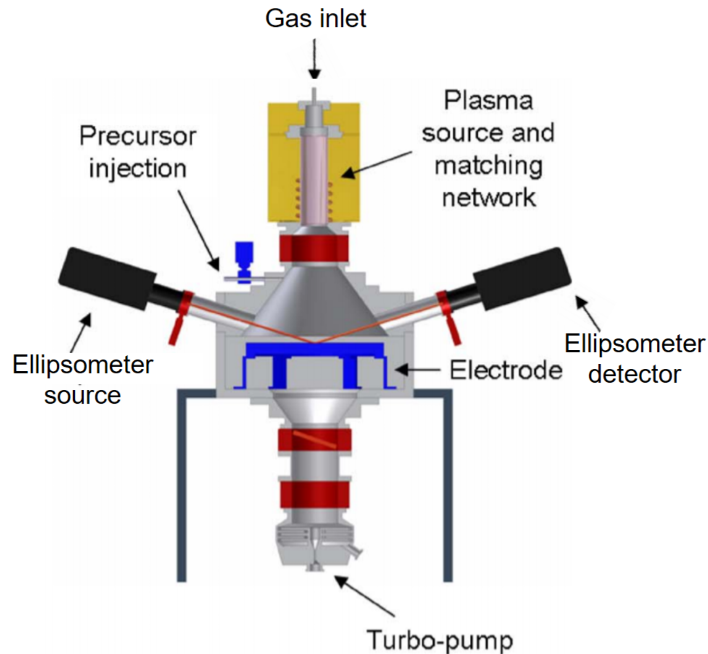


**Figure 2.1:** Schematic of the Oxford Instruments FlexAL reactor.[37] This vacuum setup is equipped with a pump system, an inductively coupled plasma (ICP) source and *in situ* spectroscopic ellipsometry (SE).

be controlled by changing the plasma power and the pressure, with operating values typically between 100 - 600 W and 10 - 300 mTorr respectively. The plasma power and pressure for each step in the used ALD recipes are given in section 2.2. Gases ($H_2$ and $O_2$) are fed into the plasma source through mass flow controllers set at a flow rate of 100 sccm.

Figure 2.1 also shows the connection to the gas lines for precursor injection. Precursors (and inhibitors) are delivered into the process chamber from independently heated bubblers, connected with fast ALD valves (minimum opening time of 10 ms.) The precursor molecules are fed into the reactor by evaporating the precursor from the container. The bubblers can be heated in order to increase the vapour pressure. The bubbler temperatures, line temperatures and pulse times are given in table 2.1, as well as the vapour pressure of the precursor at the given temperatures. In order to avoid deposition in the plasma tube and unnecessary precursor loss, the precursors are dosed with the gate valves to the pump and ICP closed, thereby trapping the precursor in the vessel. The pulse times are chosen such that sufficient precursor enters the deposition chamber, without exceeding critical values for the pressure in the chamber. Therefore, long dose times (as indicated in the ALD recipes in section 2.2) are achieved by pulsing multiple doses and purges sequentially.

The FlexAL setup is equipped with optical ports for *in situ* ellipsometry. These ports, located at a 70° angle with the normal of the substrate table, are protected from deposition by gate valves. More information about this diagnostic technique is provided in section 2.3.

**Table 2.1:** Details of the used precursors and inhibitors. The reported vapour pressures are given at bubbler temperature (RT = room temperature).

| | Bubbler temperature (°C) | Vapour pressure (mbar) | Pulse time (ms) | Line temperature (°C) | Source |
|---|---|---|---|---|---|
| Bis(diethylamino)silane (BDEAS) | 50 | 11 | 200 | 90 | [12] |
| Water | RT | 23.4 | 100 | 40 | [38] |
| Trimethylaluminum (TMA) | RT | 14.7 | 100 | 90 | [12] |
| Acetylacetone (Hacac) | RT | 1.3 | 5000 | 90 | [39] |
| Vinylphosphonic acid (VPA) | 90 | 1.4 | 5000 | 120 | [40] |

### 2.1.2 ALD-I reactor

A schematic of the ALD-I reactor is given in figure 2.2. This home-built reactor is similar to the FlexAL reactor, but does not include a loadlock. Similar to the FlexAL setup, the base pressure is approximately $10^{-6}$ mbar, and the reactor walls and gas lines are heated to 100 °C.

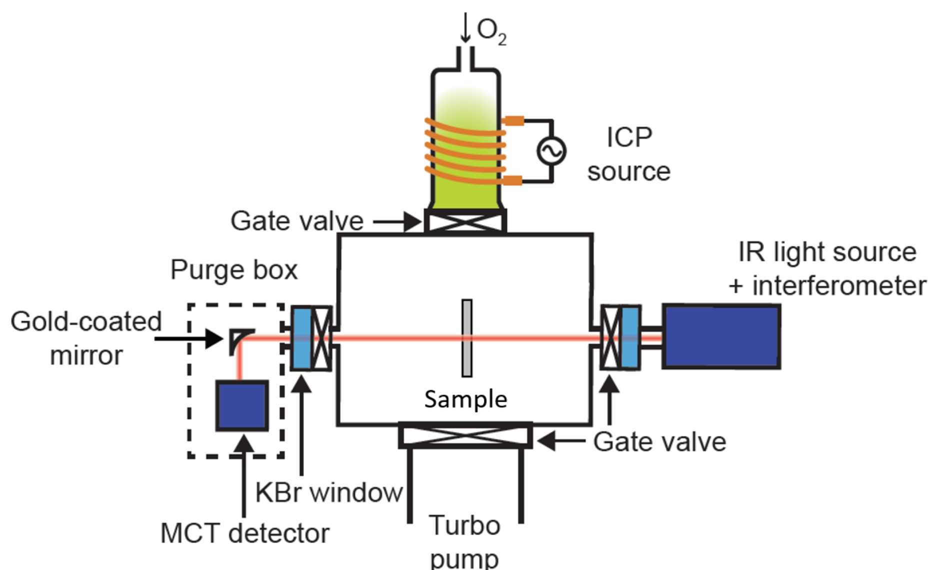


**Figure 2.2:** Schematic of the ALD-I setup. Similar to the FlexAL, this vacuum setup is equipped with a turbo molecular pump and an inductively coupled plasma (ICP) source. In order to perform *in situ* Fourier transform infrared spectroscopy (FTIR), an infrared beam is directed through KBr windows located in the wall of the reactor.

The setup is designed for *in situ* Fourier transform infrared spectroscopy (FTIR). In order to investigate what happens at the surface during ALD cycles with FTIR, the infrared light beam has to pass through the sample. Therefore, the sample is mounted onto a manipulator arm, which makes it possible to move the sample into the light beam.

In order to detect sub-monolayer levels of precursor adsorption, it is crucial to have a high signal-to-noise ratio for the FTIR measurements. This is achieved by using a powder sample, which enlarges the surface area for precursor and inhibitor adsorption. High-surface-area samples are created by pressing non-porous AEROSIL OX 50 $SiO_2$ powder[41] into a tungsten gauze (Alfa Aesar, woven from a 0.05 mm diameter wire with a 0.2 mm opening width.)[42] The powder sample is heated by passing an electrical current through the tungsten mesh. In order to monitor the temperature, a thermocouple is welded onto the sample. The sample temperature is automatically controlled and kept constant at 150 °C. However, the powder samples are not compatible with plasma exposures. Therefore, if the influence of plasmas on the surface species is investigated, a double-side polished Si wafer is used.

## 2.2 ALD cyles

In this research, adjustments to standard ALD recipes have been studied to achieve area-selective ALD. Two different ALD recipes have been examined, namely plasma-assisted ALD of $SiO_2$ and thermal ALD of $Al_2O_3$. The standard ALD recipes (combination of precursor and co-reactant) for both are given in figure 2.3. Variations from these pulse sequences will be indicated with the results obtained. For ALD of $SiO_2$, bis(diethylamino)silane (BDEAS) has been used as the precursor and an $O_2$ plasma (200 W at 25 mbar) as the co-reactant. For ALD of $Al_2O_3$, trimethylaluminum (TMA) has been used as the precursor, and $H_2O$ as the co-reactant. The structural formulas of both the precursors are given in figure 2.4. An overview of all the used molecules in this work, as well as information about the suppliers, is given in appendix A.

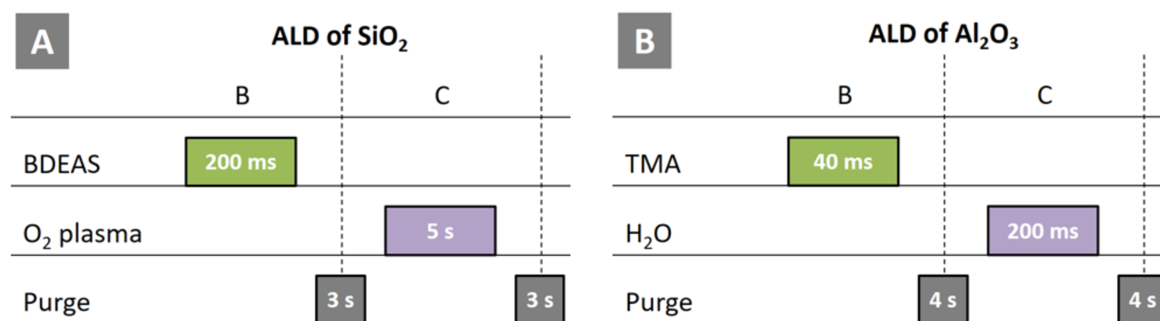


**Figure 2.3:** Pulse sequences and dose times for the used ALD recipes. (A) Pulse sequence used for ALD of $SiO_2$, (B) Pulse sequence used for ALD of $Al_2O_3$.

As stated previously, when dosing the precursor, the gate valves to the pump and ICP are closed in order to trap the precursor in the vessel and prevent unnecessary precursor losses. However, when the plasma is ignited, the chamber is being pumped down constantly. This shortens the residence time of the volatile reaction products formed during plasma exposure, to avoid redeposition of plasma species.[43]

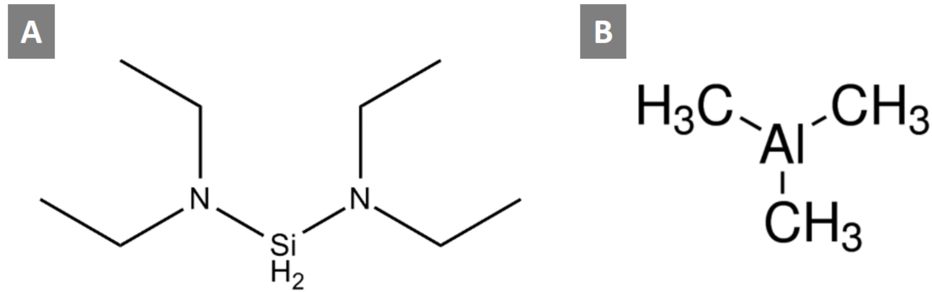


**Figure 2.4:** Structural formulas of (A) bis(diethylamino)silane (BDEAS), which is used as the precursor for ALD of $SiO_2$ and (B) Trimethylaluminum (TMA), which is used as the precursor for ALD of $Al_2O_3$.

Saturation of all the separate doses has been determined in previous research.[12,44] The reactor is conditioned prior to experiments, in order to prevent any influence of varying wall conditions. Before $SiO_2$ ALD experiments, the walls are conditioned by performing 100 cycles plasma-assisted ALD of $SiO_2$. Before $Al_2O_3$ ALD processes, the walls are conditioned with 50 cycles thermal ALD of $Al_2O_3$.

## 2.3 Ellipsometry

Spectroscopic ellipsometry (SE) is a technique used in this work to measure the change in thickness on a flat substrate during ALD cycles.[8] In this research, a J. A. Woollam M-2000 ellipsometer is used *in situ* to study ALD processes. The measurement range is from 1 to 5 eV.

Ellipsometry determines the optical response of a sample by reflecting linearly polarized light on the sample and measuring the change in polarization. Ellipsometry measurements are non-intrusive, fast and relatively easy to perform. Since this method is capable of measuring film thicknesses down to less than an Angström, it is very well-suited to study ALD processes.[45]

As shown in figure 2.5, the polarization state of the light incident on the sample is defined by two components. The $s$ component is polarized perpendicular to the plane of incidence and the p component is polarized parallel to the plane of incidence. After reflection, the polarization of the linearly polarized light changes into elliptically polarized light. The changed amplitudes are normalized to their initial values and denoted by complex $r_s$ and $r_p$ values respectively. The change in polarization is represented as an amplitude ratio $\Psi$ and the phase difference $\Delta$, given by the fundamental equation of ellipsometry:

$$\rho = \frac{r_p}{r_s} = \tan(\Psi) e^{i\Delta}. \tag{2.1}$$

$\Psi$ and $\Delta$ are dependent on the optical properties and thicknesses of the stack of individual layers, which form the sample. Ellipsometry is mostly used to determine film thickness and optical constants, but also to indirectly characterize composition, crystallinity, roughness, doping concentration and other material properties.[46]

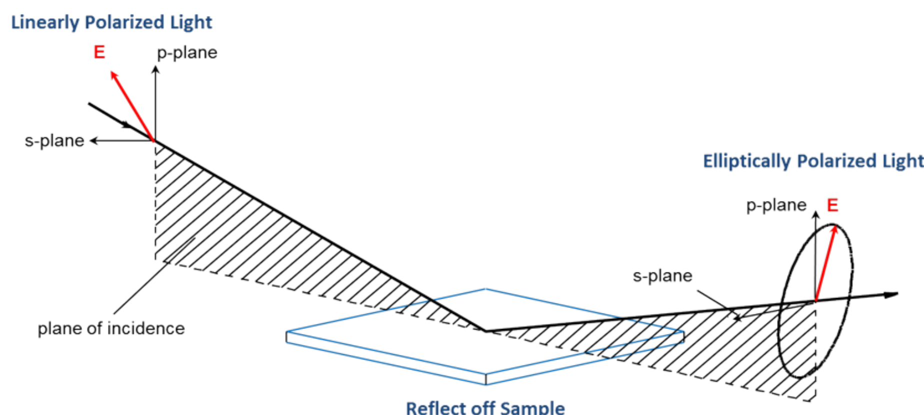


**Figure 2.5:** Schematic of linearly polarized light reflecting on a sample. The s and p components of the polarized light are indicated. The light is linearly polarized before reflection, and elliptically polarized after reflection.

In this work, two types of measurements have been conducted using ellipsometry. The first type of measurements is used to study the ALD nucleation delay. Ellipsometry measurements after every ALD cycle are performed to determine the increase of film thickness as a function of the number of cycles. This way, the nucleation behaviour can be studied and the nucleation delay determined. During the second type of ellipsometry measurements, the thickness is measured after every dose. In these so-called subcycle experiments, the adsorption (and removal) of the ALD reactants is investigated. By examining different combinations of dosing steps, more insight is gained into the ALD process.

### 2.3.1 Ellipsometry modelling

A model is required in order to convert the measured $\Psi$ and $\Delta$ by ellipsometry into the film thickness. The samples consist of a stack of several layers with different optical properties, and is therefore modelled as such. A schematic of the stack of multiple layers modelled is given in figure 2.6. The ellipsometry model starts with a substrate, which in our case is silicon. The substrate is assumed to be infinitely thick, meaning that only a single reflection from the top surface is considered. The optical constants for crystalline silicon are well known[47] and can therefore be modelled relatively easily. On top of the silicon substrate a 1 nm thick native oxide layer is modelled, which is added to the ellipsometry model separately. On top of these two layers, the ALD-grown layer is modelled.

Since $SiO_2$ and $Al_2O_3$ are non-conducting materials with an optical band gap higher than the measurement range,[48,49] a Cauchy model can be used to fit these layers. The mathematical form of the Cauchy model is given by:

$$n(\lambda) = B + \frac{C}{\lambda^2} + \frac{D}{\lambda^4} \tag{2.2}$$

where $n$ is the refractive index as a function of the wavelength of the light $\lambda$, and B, C and D are the fitting parameters. Values for these fitting parameters are specified for different

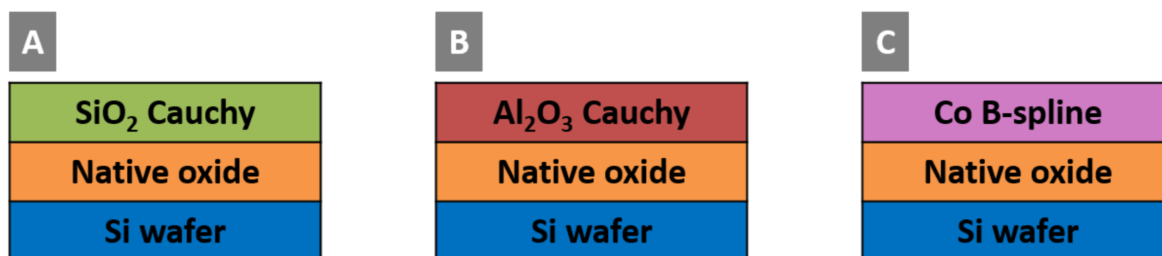


**Figure 2.6:** Schematic of the stack of layers used to model the substrates for ellipsometry analysis. (A) Model for $SiO_2$-coated substrates, (B) model for $Al_2O_3$-coated substrates and (C) model for Co-coated substrates.

materials in the ellipsometer software. For the $SiO_2$ model: B = 1.450, C = 0.01000 and D = 0. For the $Al_2O_3$ model: B = 1.751, C = 0.00632 and D = -0.00010152. The thicknesses of the individual layers of the substrate were determined using a measurement after the plasma clean, and kept constant during subsequent depositions.

For Co samples, ellipsometry modelling is different because Co is conducting and absorbs light in the entire measurement range due to the presence of free charge carriers in the material. SE measurements on absorbing films are more difficult to analyze compared to transparent films, because the general structure of the film optical constants versus wavelength is not known before measurement.[50] Therefore, a mathematical B-Spline model is used to represent the Co. This model specifies the optical constants versus wavelength using a series of control points which are equally spaced in photon energy. The B-spline layer allows arbitrary flexibility in optical constants versus wavelength, while keeping the wavelength-dependence smooth and continuous.[51] Since the B-spline model is only used to represent the substrate (which is assumed not to change during depositions), it is not crucial to accurately determine the optical constants of the Co.

The substrates are fitted (with the models shown in figure 2.6) to the first ellipsometry measurement, which is conducted after heating the sample and applying a 5 minute plasma clean ($O_2$ plasma, 200 W at 25 mbar unless indicated otherwise). The thicknesses of the individual layers of the substrate are fitted and kept constant throughout the subsequent deposition. By keeping the model for the substrate fixed, the deposited layer on top of the substrate (either $SiO_2$ or $Al_2O_3$) can be fitted more accurately. However, since the substrate is considered constant, the accuracy of the model decreases drastically if the physical substrate changes (due to e.g. oxidation, reduction or etching.)

### 2.3.2 Modelling the nucleation for area-selective ALD

As explained in section 1.3, selectivity of area-selective ALD is limited due to eventual nucleation on the non-growth area. In this work, *in situ* ellipsometry is used to measure the delay of nucleation. In order to quantify area-selective ALD, a model for analysis of the nucleation of ALD was proposed by G. Parsons.[52] This model is used to fit the experimentally obtained ellipsometry data. The model is an adaption of the Avrami model,[53] which is a well-known model to describe isothermal nucleation and phase change as a function of time. In addition

to quantifying area-selective ALD, this model gives additional information on the initiation of nucleation on the non-growth area.

The model considers that film growth begins at a number of nucleation sites that have a fixed position on the surface. The number of nucleation sites on the starting surface, $\widehat{N}(nm^{-2})$, could correspond to surface defects or other means that allow precursor or co-reactant adsorption. For a single nucleation site, the diameter of the isolated nucleus increases over an increasing number of cycles as $2\dot{G} \cdot t$, where $t$ is the time and $\dot{G}$ is the growth rate (nm/cycle). For ALD, the time $t$ is defined as the number of cycles. The growth rate is assumed to be the same in all directions, initially creating hemispherical nucleation islands on the substrate. These islands start to coalesce as growth proceeds, eventually resulting in a continuous film.

If conditions permit formation of nucleation sites during ALD, the number of nucleation sites increases as growth proceeds. Therefore, in addition to the number of nucleation sites available on the starting surface $\widehat{N}$, the generation of nucleation sites as a function of cycle number can be defined as $\dot{N}(t)$ (nm$^{-2}$cycle$^{-1}$):[54]

$$\dot{N}(t) = \exp\left(-\nu_d/t\right) \tag{2.3}$$

where $\dot{N}_0$ is the nucleation generation rate (nm$^{-2}$cycle$^{-1}$), and the parameter $\nu_d$ is the characteristic number of cycles for nucleation incubation. Nucleation sites can only be generated on exposed areas where no growth is present, so the net rate of site generation will decrease as growth proceeds. A schematic top-view of the coverage for two limiting cases, (A) $\widehat{N} > 0$ and $\dot{N} = 0$, (B) $\widehat{N} = 0$ and $\dot{N} > 0$ is given in figure 2.7.

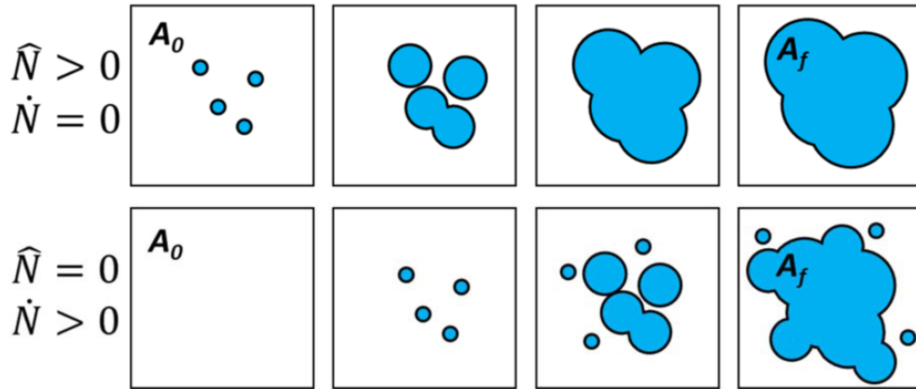


**Figure 2.7:** Schematic top-view image of growth on nucleation sites for an increasing number of ALD cycles from left to right. In the top row, the nucleation sites are present on the starting surface and grow in size as deposition proceeds. In the bottom row, nucleation sites are generated continuously during deposition.[52]

In order to calculate the coverage, the area covered by film ($A_f$) is divided by the substrate surface area ($A_0$). To obtain this fraction, firstly the so-called extended area ($A_e$) is calculated. This extended area is the increasing area of film being deposited, without taking the overlap of coalescing nucleation sites into account. The total extended area is calculated by adding up the extended area for initial sites and the extended area for sites generated during cycles.

In order to calculate the fraction of the planar substrate surface area $A_0$ that is covered by film is $A_f/A_0$, where $A_f$ corresponds to the area of the film covering the substrate, firstly the extended area $A_e$ is calculated. This area does not take into account the overlap of the coalescing nucleation sites. The total extended area is calculated by adding up the extended area for initial sites and the extended area for sites formed over cycles.

$$A_{ext}(t) = A_0\pi\left[(\dot{G}^2t^2)\widehat{N} + \int_0^t (\dot{G}^2(t-\tau)^2)\dot{N}\partial\tau\right] \tag{2.4}$$

The Avrami relation is then obtained by asserting that the change in area covered by film, $\partial A_f$ is directly proportional to the change in the extended area $\partial A_e$ and the fraction of the surface not covered by film:

$$\partial A_f = \partial A_e \cdot \left(1 - \frac{A_f}{A_0}\right) \tag{2.5}$$

which after integration gives:

$$\frac{A_f}{A_0} = 1 - \exp\left(\frac{A_e}{A_0}\right) \tag{2.6}$$

After substituting equation 2.4 into equation 2.6, the fraction of growth surface covered by film $A_f/A_0$ as a function of ALD cycles is obtained.

Eventually, in order to fit this model to ellipsometry data, the average thickness of the deposited material should be calculated. The average thickness can be calculated by determining the deposited volume, and dividing that by the planar substrate surface. To do so, firstly the extended area is determined at height $h$ above the surface, taking into account the radius of a single nucleation sites decreases with increasing height as $A_f = \pi(r^2 - h^2)$. Similarly to equation 2.4 we find:

$$A_{ext}(h) = A_0\pi\left[(\dot{G}^2t^2 - h^2)\widehat{N} + \int_0^t (\dot{G}^2(t-\tau)^2 - h^2)\dot{N}\partial\tau\right] \tag{2.7}$$

Again, using the Avrami relation from equation 2.5, the area covered by a plane at height $h$ with overlapping nuclei at a certain time or cycle ($A_f$) can be calculated:

$$A_f(h) = A_0\left[1 - \exp\Big(-A_{ext}(h)/A_0\Big)\right] \tag{2.8}$$

Then, the average thickness can be found by integrating all the determined film areas over different heights from the substrate (h=0) to the maximum deposited height ($\dot{G}t$) and dividing this by the planar substrate surface area ($A_0$):

$$T_f(n) = \frac{1}{A_0}\int_0^{\dot{G}t} A_f(h)dh \tag{2.9}$$

The average thickness for an increasing number of ALD cycles ($T_f(n)$) now depends on three variables: $\dot{G}$, $\widehat{N}$ and $\dot{N}$. $\dot{G}$ can be obtained by fitting the linear growth after nucleation has occurred. Furthermore, the assumption will be made that either all nucleation sites are present at the starting surface ($\dot{N} = 0$) or all nucleation sites are formed during ALD processing ($\widehat{N} = 0$). This way, the data acquired using ellipsometry can be fitted with the model described, quantifying the nucleation delay (as shown in chapters 4 and 5.)

## 2.4 FTIR

FTIR is used to investigate surface reactions during the individual doses in the ALD cycles. FTIR measurements are done by directing infrared light through a sample. When matter interacts with IR light, chemical bonds in the material can vibrate when certain selection rules are met. The frequency at which light is absorbed depends on the structure of the molecule. IR light can only be absorbed by a molecule if the electric dipole moment of the molecule changes during vibration. Therefore, some molecules are infrared active, and some are infrared inactive. The interaction between the IR light and infrared active molecules can be measured as a IR spectrum, which provides information about the molecules present in the light beam. By using a broadband infrared beam, the absorption of a range of frequencies can be measured. A schematic of the FTIR setup is shown in figure 2.8. The setup consists of a Bruker Optics Vector 22 interferometer, the reactor chamber, and a detector in a purge box. The Vector 22 consists of a mid-infrared source (Globar, 10000-50 $cm^{-1}$) and a Michelson interferometer. The detector is a liquid nitrogen cooled Mercury Cadmium Telluride (MCT) detector (Bruker D316, 10000-550 $cm^{-1}$).

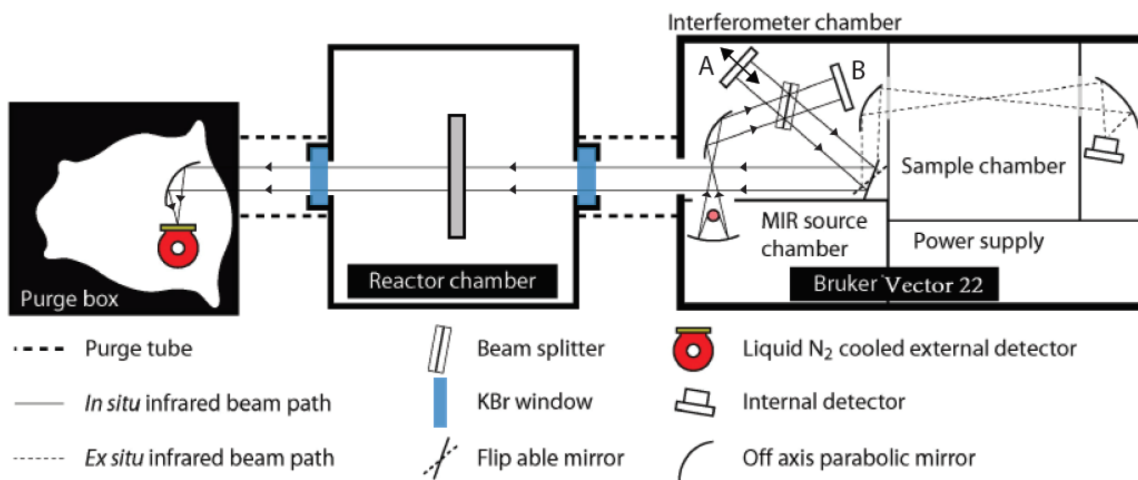


**Figure 2.8:** Schematic overview of the FTIR setup. The IR detector (left) and FTIR spectrometer (right) are attached to the ALD-I deposition chamber for *in situ* FTIR measurements. The IR beam path from the globar to the detector is shown.

In order to obtain insight into what happens on a sample during one of the dosing steps, measurements before and after dosing are taken. The portion of IR light that is absorbed by chemical bonds on the sample surface is very low and cannot be observed in a raw IR

spectrum. Therefore, the difference between two transmission spectra is calculated using:

$$A = -\log\left(\frac{l_B}{l_A}\right) \tag{2.10}$$

with A the absorbance, and $l_A$ and $l_B$ the transmitted signal intensities before and after a dose, respectively. Comparing the two transmission spectra grants the absorption spectrum, which gives information on the formation and consumption of chemical bonds on the sample. Absorbance spectra are very sensitive to surface reactions, and therefore it can be possible to detect single exposures of precursors or inhibitors. The influence of various changes in surface groups on the spectrum are illustrated in figure 2.9. In an absorbance spectrum, positive peaks correspond to formation of surface groups, and negative peaks correspond to removal of surface groups.

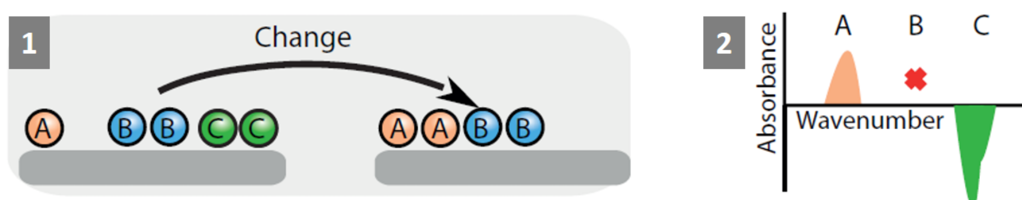


**Figure 2.9:** Response of the IR absorbance spectrum with respect to the reference as a result of changes in surface groups.[55] (1) From the change in surface groups, (2) the absorbance spectrum can be calculated. The formation and removal of surface groups are represented as positive and negative peaks respectively. Persisting surface groups do not show up in the calculated spectrum.

Figure 2.10 gives an example of an FTIR absorbance spectrum. This absorbance spectrum is obtained by measuring the transmission before and after dosing Hacac, and calculating the absorbance using equation 2.10. The adsorbance spectrum shows adsorption of Hacac on $Al_2O_3$-coated powder, as indicated by the positive peaks at 1750-1250 $cm^{-1}$. The negative peaks at 3800-3700 $cm^{-1}$ show consumption of surface -OH groups.[56,57] The fact that Hacac adsorbs on -OH groups on the $Al_2O_3$ surface agrees with the results obtained from DFT calculations as discussed in section 3.4.

In this research, FTIR has particularly been used to study the removal of inhibitor molecules using plasmas. The transmission spectrum of IR light has been measured before and after inhibitor dosing, showing the characteristic signal for the used inhibitor. Subsequently, the surface with adsorbed inhibitor has been exposed to plasmas, and the removal of the inhibitor has been studied for different plasma exposures.

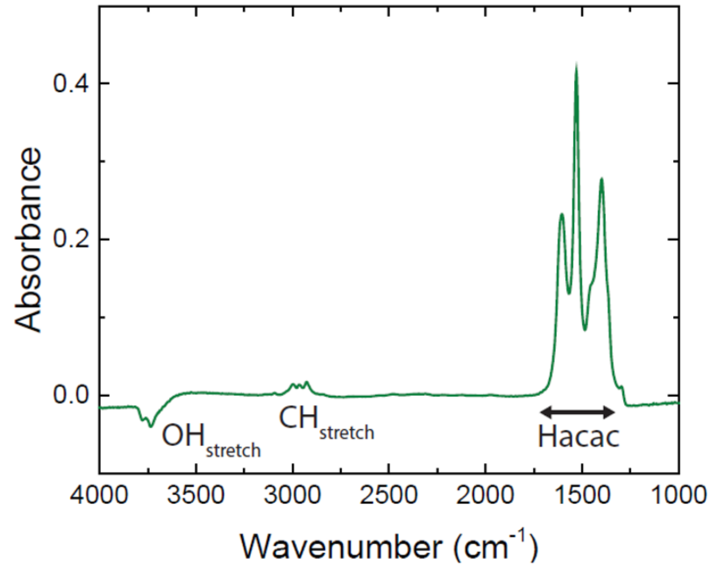


**Figure 2.10:** Measured FTIR absorbance spectrum of an Hacac dose on $Al_2O_3$-coated powder. Characteristic peaks for Hacac are indicated. This spectrum shows that Hacac adsorbs on the surface (positive peak) while -OH groups are consumed (negative peak).[58]

## 2.5 Ex situ diagnostics

Besides the *in situ* diagnostics described above, other diagnostic techniques have been used to study samples after depositions. More information on X-ray photoelectron spectroscopy (XPS), atomic force microscopy (AFM), scanning electron microscopy (SEM) and four-point probe measurements is given below.

### 2.5.1 XPS

X-ray Photoelectron Spectroscopy (XPS) is a spectroscopic technique used to invesigate the elemental composition of surfaces. A schematic representation of a typical XPS spectrometer is given in figure 2.11. In this research, XPS is used to examine the samples composition and verify deposition of material by ALD (after a nucleation delay).

In XPS, samples are irradiated with mono-energetic X-rays. Electrons are then emitted from the sample, with a energy spectra specific to the different elements. These electrons have a kinetic energy ($E_k$) depending on the X-ray photon energy ($hv$) and the original binding energy of the electrons ($E_b$). This leads to the following simple fomula:

$$E_b = hv - E_k - \phi \tag{2.11}$$

where $\phi$ is the so-called spectrometer workfunction which is determined through calibration and considered a constant.[60] Since the photon energy is known, measurement of the kinetic energy yields the binding energy of the electron. A spectrum is obtained by scanning and plotting the number of detected electrons (per energy interval) versus their kinetic energy.

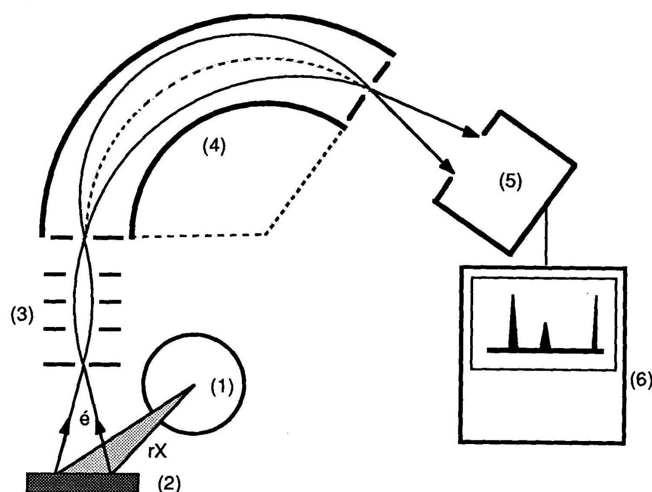


**Figure 2.11:** Simplified schematic representation of a typical XPS spectometer.[59] The essential features are indicated; 1. X-ray source, 2. specimen, 3. electron transfer lens, 4. electron energy analyser, 5. electron detector and 6. obtained spectrum.

Each element has a unique spectrum, and the spectrum from a mixture of elements is approximately the sum of the peaks of the individual elements.[61] Since the binding energy value for a specific element also depends on its chemical environment, an XPS measurement also gives information on oxidation states of the atoms in the sample, making it for example possible to differentiate between elemental Si and Si bound to O.

### 2.5.2 Atomic force microscopy

Atomic force microscopy (AFM) is a technique used to investigate the roughness of a surface. AFM operates by scanning a cantilever with a sharp tip (probe) on its end over a surface. Because the tip is extremely sharp (with the radius of curvature in the order of nm), AFM is able to scan the surface with atomic resolution. When the tip is brought into proximity of the surface, forces between the sample and the tip lead to a deflection of the cantilever according to Hooke's law.[62] By measurement of the cantilever deflection using optical techniques it is possible to evaluate the tip-surface interactive force. This way, AFM can be used to study the roughness of samples, independent of their conductivity.[63]

### 2.5.3 Scanning electron microscopy

Scanning electron microscopy (SEM) is an *in vacuo* diagnostic technique that investigates the topography of a sample by scanning the surface with a focused beam of electrons. The electrons interact with the atoms in the sample, producing signals that contain information about the surface topography and composition of the sample. When the primary electron beam interacts with the sample, secondary electron are emitted by inelastic scattering interactions. Because the emitted electrons have a relatively low energy, the microscope only detects secondary electrons originating within a few nm from the sample surface. This makes SEM a very surface-sensitive diagnostic.[64] A high-resolution image of the topography can be formed by scanning the surface with the electron beam and measuring the secondary electron emission. The emission of secondary electrons not only varies for different materials, but also depends on the angle of incidence of the electrons. Therefore, steep surfaces and edges appear well-defined in the produced image.

# Chapter 3

# Review of previous work: Area-selective ALD of $SiO_2$ using ABC-type cycles

The research described in this thesis builds upon work previously performed in the group by Mameli *et al.*[29] The results have been published, and provide a starting point for this work. In this chapter, the published paper will be reviewed, in order to provide background information for the current project. The data in this chapter is directly taken from the published work by Mameli *et al.*, with some textual elaboration on results interesting for the follow-up research presented in this thesis. By elaborating on this data, some specific experiments are introduced which have been used throughout the current project.

## 3.1 Area-selective ALD using ABC-type cycles

A novel approach for area-selective ALD uses a three-step (ABC-type) cycle to selectively deposit $SiO_2$.[29] A schematic illustration of the ABC-type ALD approach is shown in figure 3.1. The growth area and the non-growth area are indicated. In the first step (A), the inhibitor is dosed. The inhibitor adsorbs on the non-growth area, without adsorbing on the growth area. In the second step (B), when the ALD precursor is dosed, the adsorption of precursor is blocked by the inhibitor molecules on the non-growth area, but not affected on the growth area. In the third step (C), an $O_2$ plasma is used as the co-reactant. The $O_2$ plasma removes the precursor ligands together with the adsorbed inhibitor molecules. Using these ABC-type cycles, the inhibitor molecules are reapplied and removed in every cycle.

The novelty in this approach for area-selective ALD is the use of small inhibitor molecules that are dosed in every cycle. The non-growth area is deactivated in a similar way to SAMs, but the inhibitor molecules are reapplied every cycle. SAMs are generally not compatible with temperatures over 100°C and the use of plasmas. Because the inhibitor molecules in the ABC-type approach are renewed every cycle, this process is compatible with plasma species and higher temperatures.

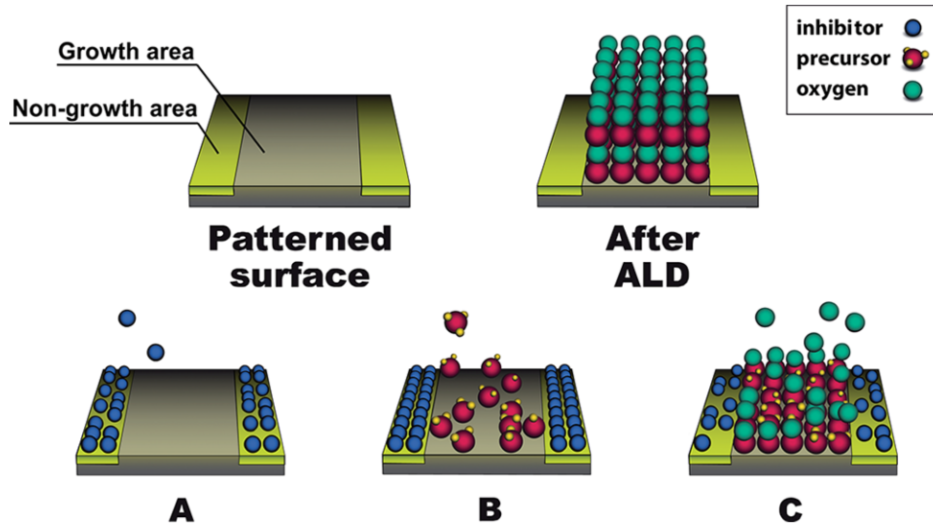


**Figure 3.1:** Schematic of ABC-type cycles used to selectively deposit $SiO_2$ as proposed by Mameli *et al.*[29] During step A, the inhibitor is dosed. The inhibitor adsorbs selectively on the non-growth area. Subsequently, during step B, the precursor is dosed. The precursor adsorbs on the growth area but adsorption on the non-growth area is blocked by the inhibitor molecules. Lastly, during step C, the substrate is exposed to an $O_2$ plasma. The plasma removes the inhibitor molecules and precursor ligands from the surface.[29]

The work by Mameli *et al.* demonstrates proof-of-concept for area-selective ALD of $SiO_2$ using ABC-type ALD cycles. The process consists of dosing acetylacetone (Hacac) as the inhibitor, bis(diethylamino)silane (BDEAS) as the precursor and an $O_2$ plasma as the co-reactant. Various starting surfaces have been investigated, and the nucleation curves measured using *in situ* ellipsometry is given in figure 3.2. The graph shows that $SiO_2$ grows without any nucleation delay on $GeO_2$, $SiO_2$, $WO_3$ and $SiN_x$. On these substrates, a growth rate of approximately 0.09 nm/cycle was obtained, comparable to the growth for regular $SiO_2$ ALD.[12] On the other hand, nucleation delays were observed on $Al_2O_3$, $TiO_2$ and $HfO_2$. The growth delay of approximately 15 cycles on $Al_2O_3$ means that a $SiO_2$ film of approximately 1 nm thickness can be selectively deposited on $SiO_2$ in the presence of $Al_2O_3$. Because these materials showed the biggest difference in nucleation behaviour, further experiments are conducted on these substrates.

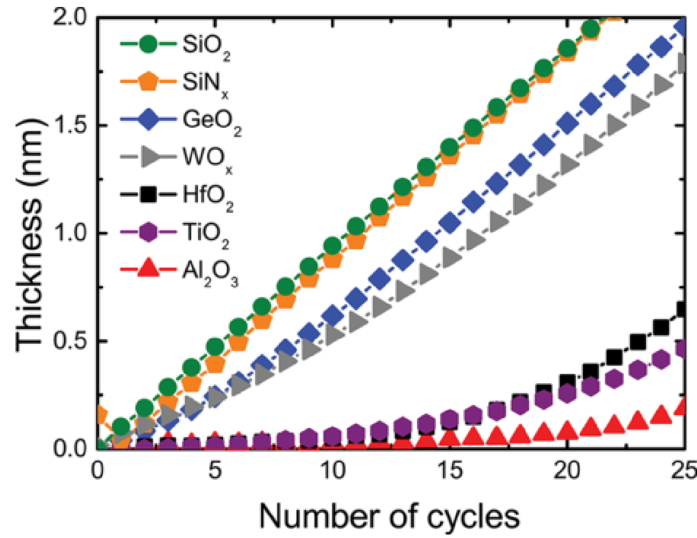


**Figure 3.2:** *In situ* ellipsometry data of nucleation curves for ABC-type ALD of $SiO_2$ on different starting surfaces. Nucleation occurs (almost) immediately on $SiO_2$, $SiN_x$, $GeO_2$ and $WO_x$, but is delayed on $HfO_2$, $TiO_2$ and $Al_2O_3$, illustrating the possibility for area-selective ALD.

## 3.2 Subcycle experiments

In order to gain more insight into the inhibited deposition on $Al_2O_3$ in comparison to the immediate deposition on $SiO_2$, an alternative ellipsometry experiment was conducted where the apparent thickness was measured after every reactant dosing pulse. Since the dielectric function of a monolayer of Hacac is not known, it cannot be taken into account in ellipsometry modelling. Therefore, the measured thickness does not correspond directly to the actual thickness, but is represented as an *apparent thickness*, which is a measure for the amount of adsorbed or deposited material.[8] In these so-called subcycle experiments, ellipsometry measurements are conducted after every individual dose for different subcycle recipes. Figure 3.3 shows results for sequential AC, ABC and BC cycles on $Al_2O_3$ and $SiO_2$. In AC cycles (which is a combination of inhibitor and $O_2$ plasma), adsorption and removal of the inhibitor is investigated. In ABC cycles, blocking of precursor adsorption is studied, and in BC cycles deposition without using inhibitors is examined as a reference.

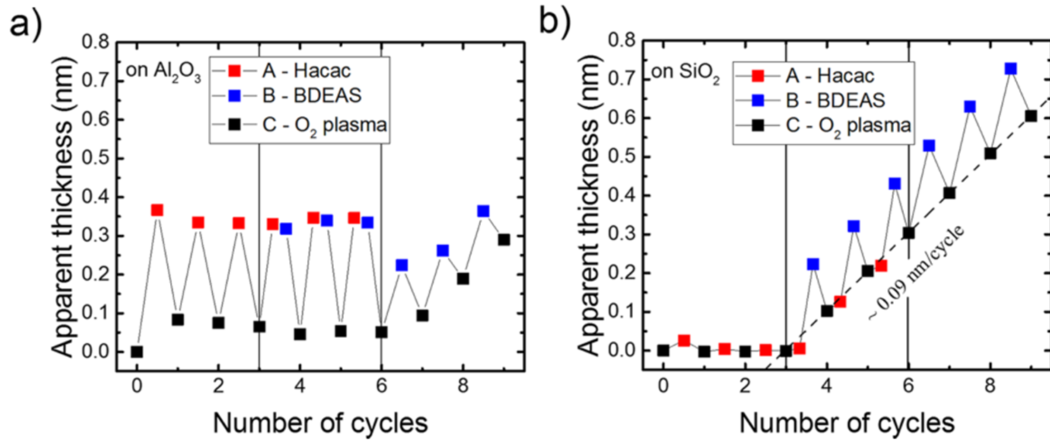


**Figure 3.3:** *In situ* ellipsometry data for subcycle experiments for ABC-type ALD of $SiO_2$ on (a) $Al_2O_3$ and (b) $SiO_2$. From left to right, the apparent thickness is shown for AC, ABC and BC cycles.

The data for the AC cycles on $Al_2O_3$ in figure 3.3 (a) shows an apparent thickness increase after each A step and a decrease after every subsequent C step. This indicates that Hacac is adsorbed on the surface, and removed again by the plasma exposure. Pulse C removes the adsorbed Hacac by combustion reactions and hydroxylates the surface for the subsequent cycle. The thickness does not decrease completely to zero during the $O_2$ plasma steps, which was speculated by Mameli *et al.* to be caused by changes in the underlying $Al_2O_3$ substrate. However, this can also indicate incomplete removal of the adsorbed Hacac molecules from the surface (as is studied in more detail in chapter 4.) The middle part of figure 3.3a, representing the ABC cycles on $Al_2O_3$, indicates that after exposing the surface to Hacac (A), no significant amount of precursor adsorption takes place (B). Conversely, when performing the normal ALD cycles consisting of BDEAS (B) and $O_2$ plasma (C), there is a net increase in thickness indicating deposition of $SiO_2$ with a growth per cycle of ~0.09 nm/cycle.

Figure 3.3b shows the same subcycle experiments for a $SiO_2$ starting surface. In the AC cycles, there is virtually no change in apparent thickness, indicating that Hacac does not adsorb on $SiO_2$. Consequently, ABC-type cycles on $SiO_2$ result in the same growth per cycle (0.09 nm/cycle) as observed for regular ALD in BC cycles. This demonstrates that the addition of Hacac does not influence $SiO_2$ ALD on $SiO_2$ substrates. In conclusion, subcycle experiments show selective adsorption of Hacac on $Al_2O_3$, and blocking of precursor adsorption by the inhibitor molecules, explaining the nucleation delay observed on $Al_2O_3$ for this process.

## 3.3 Fourier transform infrared spectroscopy

In order to investigate the surface chemistry of the ABC-type ALD process of $SiO_2$, *in situ* infrared spectroscopy experiments were performed. The consecutive adsorption of Hacac and BDEAS were investigated on pellet-pressed $Al_2O_3$ and $SiO_2$-coated pellet-pressed $SiO_2$ powder, using Fourier transformed infrared spectroscopy. FTIR difference spectra, which show the formation and consumption of chemical bonds on the surface (as explained in section 2.4), have been measured for Hacac and BDEAS adsorption, and are depicted in figure 3.4.

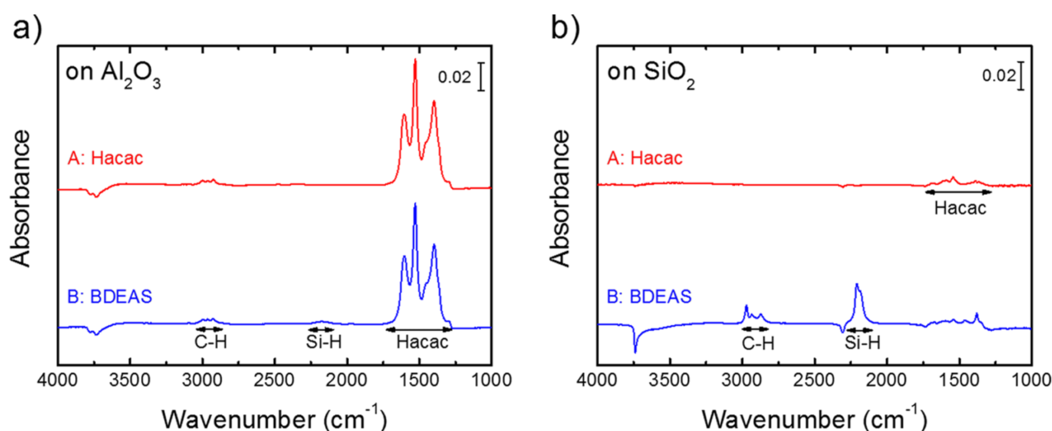


**Figure 3.4:** FTIR data on consecutive doses of Hacac (step A) and BDEAS precursor (step B) during ABC-type ALD of $SiO_2$ on (a) $Al_2O_3$ and (b) $SiO_2$.

The data from figure 3.4 (a) confirms the adsorption of Hacac on $Al_2O_3$, as shown by the absorption peaks in the wavenumber range 1300 - 1650 $cm^{-1}$.[56,65] In the subsequent dose of BDEAS, the spectrum only shows minor changes, which indicates that the adsorbed Hacac molecules inhibit chemisorption of BDEAS molecules on the $Al_2O_3$ surface. When comparing figure 3.4 (a) and (b), it can be concluded that only a small fraction of Hacac adsorbs on the $SiO_2$ surface. Also, when dosing BDEAS (after dosing Hacac on $SiO_2$), the C-H and Si-H stretching vibrations (peaks in respectively the 2800 - 3000 $cm^{-1}$ and 2130 - 2240 $cm^{-1}$ wavenumber ranges) reveal adsorption of BDEAS molecules.[66,67] Concurrently, the negative peak around 3740 $cm^{-1}$ indicates loss of O-H stretching vibrations of the surface hydroxyl groups, which are consumed during BDEAS precursor adsorption.[66,68]

In summary, the FTIR study confirms that Hacac selectively adsorbs on $Al_2O_3$, and subsequently inhibits the adsorption of BDEAS. However, the small amount of Hacac adsorption on $SiO_2$ shows that the adsorption of inhibitor is not completely selective. Furthermore, the small amount of BDEAS adsorption on $Al_2O_3$ after dosing Hacac shows that the blocking of precursor is not perfect and indicates room for improvement.

In the ellipsometry subcycle experiments (section 3.2), it was shown that adsorbed Hacac is not fully removed from the surface using an $O_2$ plasma. To further investigate the removal of Hacac from the surface using an $O_2$ plasma, FTIR measurements of adsorbed Hacac on an $Al_2O_3$ surface were performed as a function of $O_2$ plasma exposure, as shown in figure 3.5. This data was not included in the discussed publication by Mameli *et al.*, but was part of a follow-up project.[58]

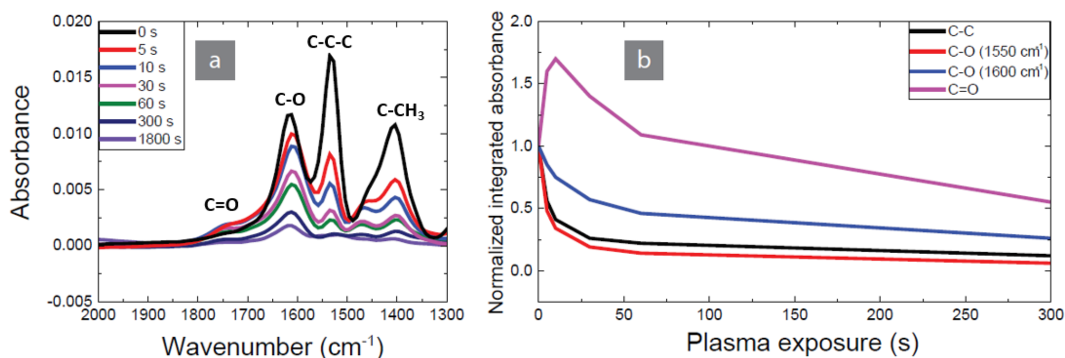


**Figure 3.5:** (a) FTIR absorbance spectra of adsorbed Hacac of an $Al_2O_3$ coated wafer sample for an increasing $O_2$ plasma exposure and (b) the integrated absorbance of various IR peaks associated with adsorbed Hacac as a function of the plasma exposure.[58]

FTIR absorbance spectra of adsorbed Hacac for increasingly long $O_2$ plasma exposures are shown in figure 3.5a. Figure 3.5 b shows the area of the separately integrated peaks characteristic for Hacac as a function of the plasma exposure. Two interesting conclusions can be drawn from this data. Firstly, the FTIR data shows that even for very long plasma exposures, the adsorbed Hacac is not fully removed. The absorbance spectra of adsorbed Hacac after 30 minutes, as shown in figure 3.5 a, still shows some acac species on the surface. Secondly, the IR absorbance of the peaks associated with adsorbed Hacac, as shown in figure 3.5 b, decrease with different rates as function of $O_2$ plasma exposure. This data also shows the creation of C=O peaks when removing the adsorbed Hacac with a $O_2$ plasma. This proves that the adsorbed Hacac molecules are only partially combusted by the $O_2$ plasma, creating fragments of the Hacac molecule on the surface.

Incomplete removal of Hacac fragments from the surface can influence the amount of reactive -OH groups on the surface, which limits new adsorption of Hacac. The results from FTIR agreed with ellipsometry results. Since the incomplete removal of Hacac could limit the selectivity, this hints at a possible improvement for the process. The use of a $H_2$ plasma to fully remove the adsorbed Hacac has been investigated, and the results are given in chapter 4.

## 3.4 DFT calculations

Density functional theory (DFT) calculations were performed to get a better understanding of the adsorption of Hacac on $Al_2O_3$ and $SiO_2$. The results are shown in figure 3.6. Hydroxylated surfaces of $\alpha$-$Al_2O_3$ (0001) and $\alpha$-$SiO_2$ (0001) were modelled to represent the experimentally used substrates. Calculations showed that Hacac binds to both surface preferably in chelate configurations, with both of its oxygen atoms bonded to $Al^{3+}$/ $Si^{4+}$, forming $H_2O$ as a by-product. In order to check if adsorption is thermodynamically favourable, the minimum energy paths for Hacac adsorption on both $Al_2O_3$ (a) and $SiO_2$ (b) were calculated, which are depicted in figure 3.6.

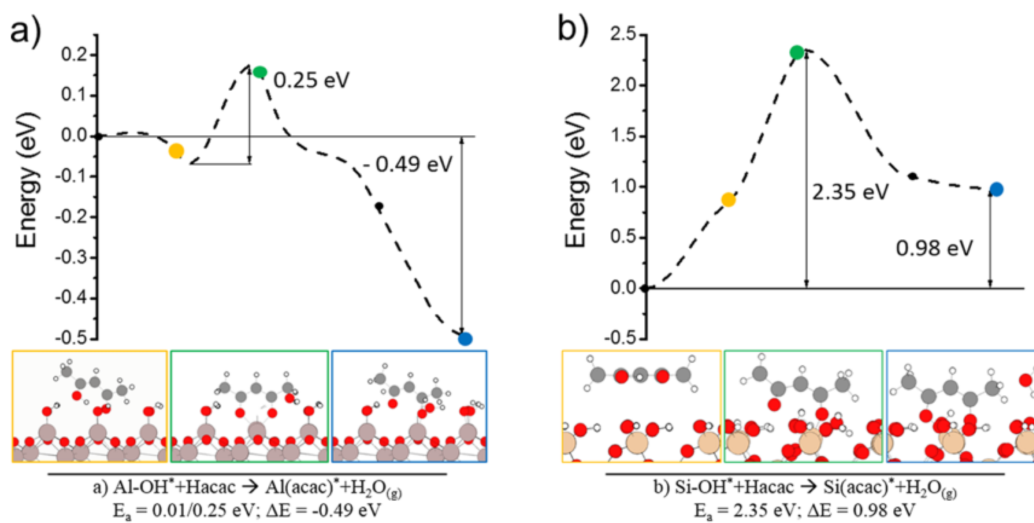


**Figure 3.6:** Calculated DFT results for Hacac adsorption on (a) $Al_2O_3$ and (b) $SiO_2$ surfaces. Below the graphs the physisorbed state (yellow), intermediate state (green) and chelate bonded acac (blue) are indicated, corresponding with the colored points on the graph.

The minimum energy paths confirm selective adsorption of Hacac on $Al_2O_3$. On $Al_2O_3$, the entire adsorption process of Hacac is energetically favourable with $\Delta E_{total} = -0.49$ eV. On $SiO_2$, the process is not energetically favourable with $\Delta E_{total} = 0.89$ eV. For both substrates, formation of an intermediate state in the chemisorption process results in energy barriers. On $Al_2O_3$, the small energy barrier of 0.25 eV is accessible by the energy gained in physisorption. On $SiO_2$, the extremely high energy barrier of 2.35 eV hinders adsorption of Hacac. In the supplementary info it was predicted that the $H_2O$ formed as a by-product in the chemisorption process, have a stabilizing effect on the final chemisorbed product.[69] The stabilizing effect is due to the enhanced H-bonding network between the $H_2O$ and the surface -OH groups. It was stated that accumulating $H_2O$ by-products could be competing with the Hacac adsorption by partly blocking available sites, and removal of these side products would enhance the Hacac inhibition power.

From these DFT calculations it can be concluded that Hacac binds on the hydroxylated $Al_2O_3$ surface, while the overall reaction on hydroxylated $SiO_2$ is both thermodynamically and kinetically hindered. This explains the selectivity of Hacac adsorption on $Al_2O_3$ as opposed to $SiO_2$ during ABC-type ALD of $SiO_2$.

## 3.5 Open questions

In this chapter, the previous work done in our group relevant to this project was summarized. Some questions were left unanswered, which provided a starting point for this project. Firstly, it was shown using FTIR and ellipsometry that an $O_2$ plasma is not able to completely remove adsorbed Hacac from the surface. Leftover Hacac fragments can influence subsequent Hacac adsorption, possibly limiting the selectivity. In literature, a $H_2$ plasma was shown to be effective at the removal of adsorbed Hacac. Therefore, new FTIR and ellipsometry meas-

urements are proposed to check the removal of adsorbed Hacac by a $H_2$ plasma. Moreover, if the inhibitor can be removed completely, it is interesting to check whether or not this was the limiting factor inducing loss of selectivity.

Additionally, it might be possible to extend this area-selective ALD approach to metal/dielectic patterns. In literature it has been shown that $Co(acac)_2$ and $Co(acac)_3$ are stable molecules at the operating temperature.[70,71] This is a first indication that Hacac molecules could adsorb on a Co substrate, possibly blocking ALD of $SiO_2$. Furthermore, initial experiments of this process on $CoO_x$ showed a nucleation delay for ABC-type ALD of $SiO_2$. Therefore, the approach discussed in this chapter seemed a good candidate to achieve area-selective ALD on metal/dielectric patterns.

# Chapter 4

# Improving area-selective ALD of $SiO_2$ in the presence of $Al_2O_3$ using ABDC-type cycles

The approach reported in chapter 3, which uses three-step cycles to achieve area-selective ALD of $SiO_2$, obtained $\sim$ 1 nm of selective growth. As explained in chapter 1, more selective deposition is needed to deposit sufficient dielectric material for the application of self-aligned VIAs. In this chapter, FTIR experiments are performed to investigate the adsorption and removal of Hacac using different plasmas. In order to increase the nucleation delay from the three-step process, a separate inhibitor removal step has been included in the ABC-type process, resulting in an ABDC-type cycle. Ellipsometry and XPS were used to determine the improvement of the nucleation delay.

## 4.1 Removal of adsorbed acac species

Ideally, when performing ABC-type ALD cycles, firstly inhibitor molecules adsorb (on the non-growth area ($Al_2O_3$))(A). During precursor dosing (B), the adsorption of precursor is blocked. Subsequently, during the $O_2$ plasma exposure (C), the inhibitor molecules are removed, resetting the non-growth area for new inhibitor adsorption. The plasma exposure step not only removes the inhibitor molecules from the non-growth area, but also removes the precursor ligands from the adsorbed precursor on the growth area. However, this ideal case of area-selective ALD using ABC-type cycles does not completely accord with reality. It was shown in section 3.3 that the inhibitor molecules were not fully removed by the $O_2$ plasma exposure, and inhibitor fragments were formed. Therefore, the removal of adsorbed Hacac from an $Al_2O_3$ surface was studied using FTIR.

Hacac was dosed on a double side polished Si wafer, which was coated with $Al_2O_3$. The absorbance spectra of Hacac is shown in figure 4.1 A, where the characteristic peaks for acac surface species are indicated. By measuring the absorbance of adsorbed Hacac for increasing $O_2$ plasma exposures, the removal of Hacac is examined. The normalized integrated absorbance of the Hacac on the surface as a function of plama exposure time (as depicted

in figure 4.2) shows that even for very long $O_2$ plasma exposures (5 minutes), the adsorbed Hacac is not fully removed. The long exposure times in these experiments are specific for the setup used (the home-built ALD-i reactor.) When transferring these experiments to the FlexAl reactor (where the nucleation delay is measured with ellipsometry) plasma exposure times are significantly shorter than 300 seconds. However, it can be concluded that even for very long $O_2$ plasma exposures the adsorbed acac is not fully removed from the surface.

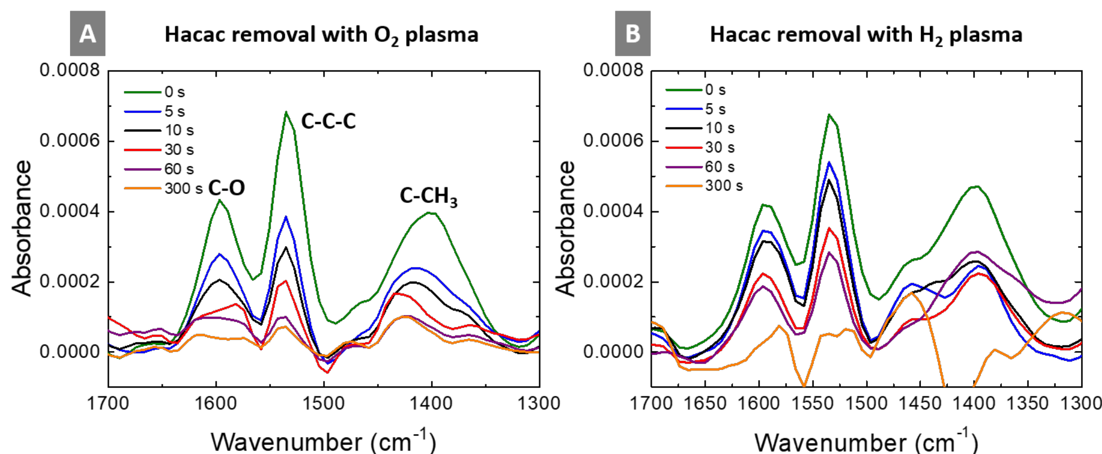


**Figure 4.1:** FTIR data on the removal of Hacac molecules from an $Al_2O_3$ surface. FTIR absorbance spectrum of the adsorbed Hacac molecules have been plotted for an increasing (A) $O_2$ plasma exposure and (B) $H_2$ plasma exposure. The characteristic peaks of Hacac are indicated.

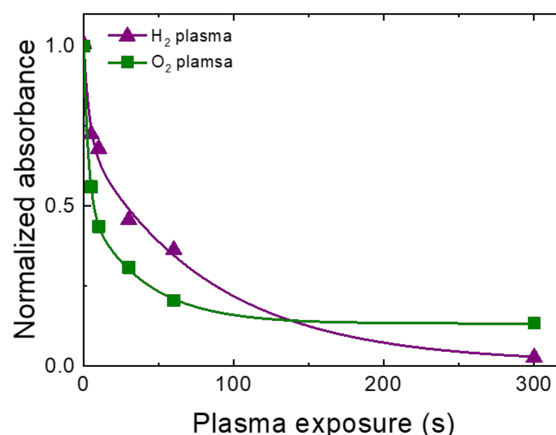


**Figure 4.2:** Normalized integrated area of the characteristic peaks from figure 4.1 (from 1700 to 1300 $cm^{-1}$) as a function of $O_2$ and $H_2$ plasma exposure.

It was previously shown (in section 3.3) that the remaining surface species after a long $O_2$ plasma exposure do not consist of intact acac species. In literature, it was shown that O and $O_3$ exposures of alkane ligands can result in formation of surface carbonates or formates.[72,73] During plasma exposure, the $O_2$ plasma combusts the acac ligands, resulting in fragments

remaining on the surface that can be hard to be removed. These fragments will partially occupy the surface, hindering new Hacac adsorption. Therefore, the renewed layer of inhibitor molecules in the subsequent cycle is arranged less orderly. This is believed to limit the selectivity achieved using ABC-type cycles.

Johnson *et al.* reported that H radicals from a $H_2$ plasma are able to effectively remove adsorbed acac from the surface.[74] By using a $H_2$ plasma it should be possible to remove the adsorbed ligand in one piece, and prevent fragments from forming on the surface. The FTIR absorbance spectra of adsorbed Hacac for increasing $H_2$ plasma exposures is shown in figure 4.1 B. For the long plasma exposures, a significant increase in noise is visible. Small changes in the measured FTIR transmission (e.g. due to changes in temperature or pressure) affect the absorbance spectra greatly. However, the characteristic peaks of Hacac seem not to be present after a 300 s $H_2$ plasma exposure. The normalized absorbance of the characteristic peaks of Hacac as a function of $H_2$ plasma exposure is depicted in figure 4.2. It is shown that eventually, the $H_2$ plasma is able to completely remove the adsorbed Hacac from the surface. Although the measurement uncertainty for long plasma exposures was very large in this measurement, a repeated measurement showed similar results in terms of normalized absorbance, indicating that adsorbed Hacac can be completely removed using a $H_2$ plasma.

The results obtained with FTIR agree with *in situ* ellipsometry data. In order to study the adsorption and removal of inhibitor, subcycle experiments have been conducted. A combination of inhibitor doses (A) and plasma exposures (C for $O_2$ plasma, D for $H_2$ plasma) have been alternately dosed onto an $Al_2O_3$ surface. Figure 4.3 shows the apparent thickness for adsorption and removal of acac ligands using (A) an $O_2$ plasma and (B) a $H_2$ plasma. Since the optical properties of a monolayer of acac are unknown, it has been modelled as a Cauchy layer. The apparent thickness is therefore not an absolute thickness, but gives a measure for the amount of adsorbed inhibitor.

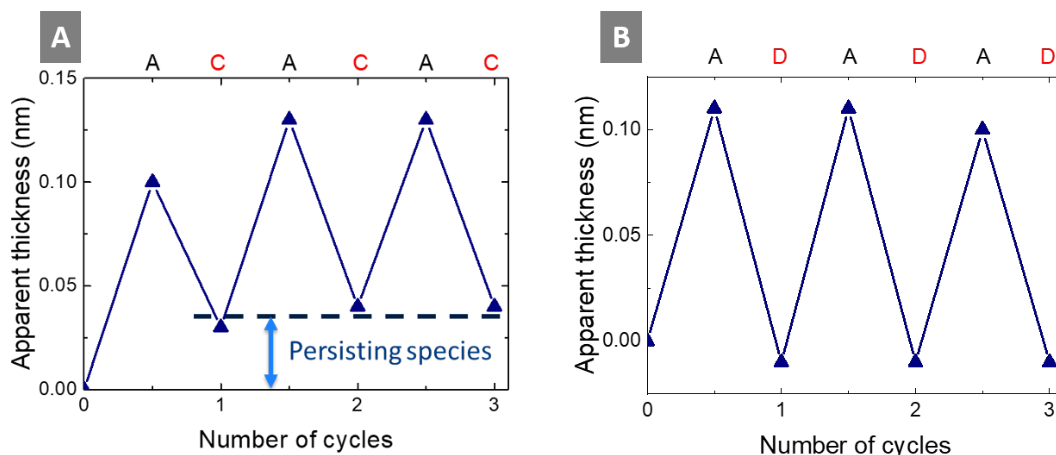


**Figure 4.3:** *In situ* ellipsometry data on the adsorption and removal of acac ligands from an $Al_2O_3$ surface. (A) Apparent thickness for consecutive Hacac doses (A) and $O_2$ plasma exposures (C). After the first dose, the thickness does not reduce to zero, which indicates the presence of persisting species. (B) Apparent thickness for consecutive Hacac doses (A) and $H_2$ plasma exposures (D).

Figure 4.3 A shows the apparent thickness for consecutive Hacac doses and $O_2$ plasma exposures. After the first dose of inhibitor, the apparent thickness does not decrease to zero after the $O_2$ plasma exposure. This indicates persisting species on the surface. Although it is not possible to say what these persisting species are on the basis of ellipsometry measurements, these persisting species on the surface could hinder subsequent Hacac adsorption.

Figure 4.3 B shows the apparent thickness for consecutive Hacac doses and $H_2$ plasma exposures. After the first cycle of inhibitor and plasma, the apparent thickness decreased to zero. This indicates that there are no persisting species on the surface, which shows complete removal of inhibitor molecules. In fact, the thickness decreases slightly below zero, which suggests an etching component. The EPC (etch per cycle) has been determined over 30 cycles in a separate experiment and averaged out to be 0.04 Å/cycle. This etching component can be explained by the formation of volatile $Al(acac)_3$. In literature, the formation of $Al(acac)_3$ was used for atomic layer etching (ALE) of $Al_2O_3$.[75] However, the very small etching component (compared to the GPC of $SiO_2$ ALD) should not be detrimental to the area-selective ALD process.

## 4.2 Improving the selectivity of $SiO_2$ ALD by using a four-step cycle

FTIR and ellipsometry experiments suggest that the adsorbed acac molecules are not fully removed when using an $O_2$ plasma. It was shown that a $H_2$ plasma is able to completely remove adsorbed acac from the surface. By eliminating acac fragmentation on the surface, new Hacac adsorption in the subsequent cycle can be improved, increasing the selectivity. Therefore, a four-step (ABDC-type) process is suggested.

A schematic of the developed four-step cycle is depicted in figure 4.4. In comparison with the ABC-type cycles (as shown in chapter 3) an extra $H_2$ plasma exposure step (D) has been added between the precursor dosing step and the $O_2$ plasma exposure. By dosing the $H_2$ plasma step before the $O_2$ plasma, the inhibitor molecules can be completely removed. Then, in the final step, the $O_2$ plasma exposure is only responsible for removal of the precursor ligands on the growth area, resulting in $SiO_2$ deposition.

### 4.2.1 Subcycle experiments on ABDC-type ALD cycles

In order to study the four-step cycle process, the apparent thickness has been measured with ellipsometry after every reactant dosing pulse. These subcycle experiments show the apparent thickness after every step, giving an indication of adsorption and removal of the ALD reactants. The change in apparent thickness during different combinations of dosing steps is depicted in figure 4.5. The dosing times used for this experiment are the same as the dosing times given in figure 2.3 A, with the addition of (A) a 15 second Hacac dose and (D) a 30 second $H_2$ plasma exposure. In order to maximize the hydrogen radical flux to the surface without damaging the surface with high energy ions, the plasma power and pressure were set at 600 W and 300 mTorr.

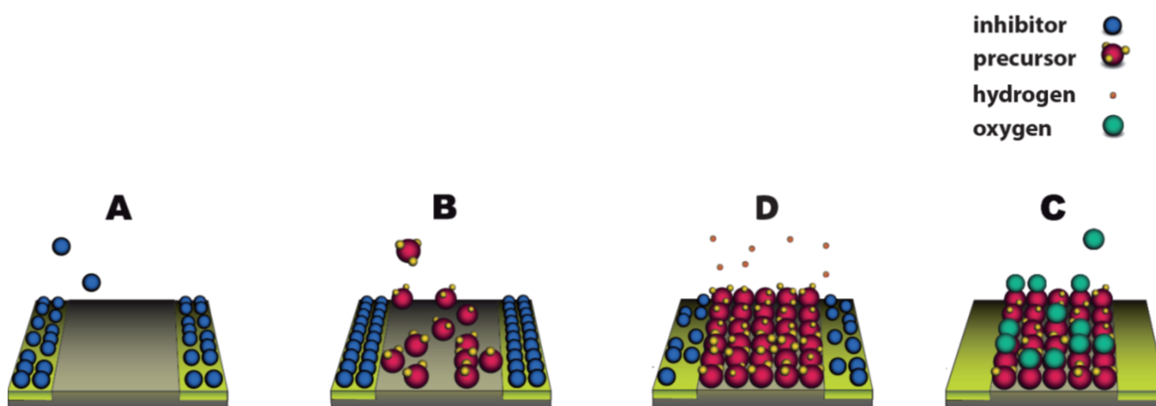


**Figure 4.4:** Schematic of the proposed ABDC-type ALD cycles of $SiO_2$ on $Al_2O_3$. An extra step (D) has been added, which fully removes the adsorbed inhibitor.

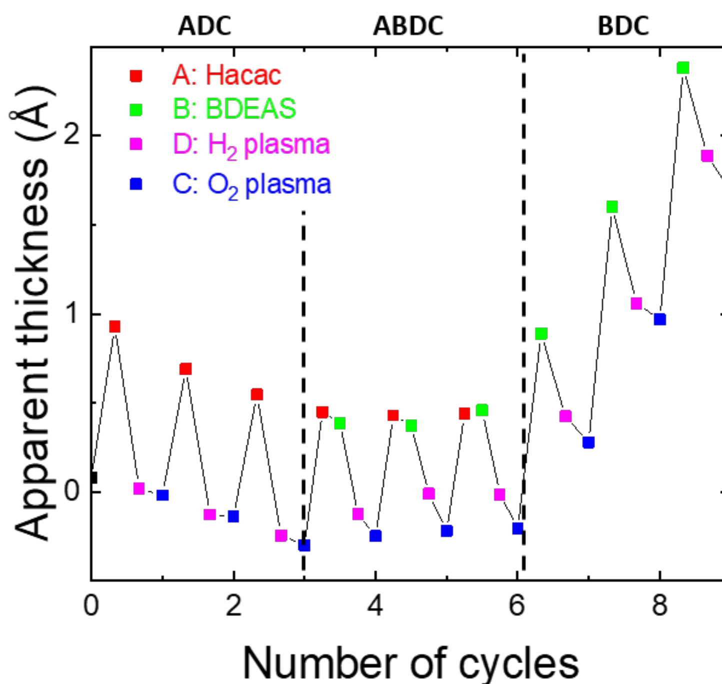


**Figure 4.5:** *In situ* ellipsometry data on subcycle experiments for ABDC-type ALD of $SiO_2$ on $Al_2O_3$. The left part shows adsorption and removal of inhibitor molecules, the middle part illustrates the full ALD cycles and the right part shows ALD without using an inhibitor.

In the first part of the graph, three ADC-cycles have been dosed onto the $Al_2O_3$ substrate. Firstly, the apparent thickness increases due to adsorption of Hacac on the surface. Then, the sample is exposed to a $H_2$ plasma, resulting in removal of the adsorbed Hacac. Subsequently, an $O_2$ plasma is dosed, which results in a small decrease of apparent thickness. This could indicate removal of inhibitor, although that would not be consistent with the results from

FTIR experiments. Furthermore, the apparent thickness is already reduced back to zero by the $H_2$ plasma, showing full inhibitor removal before the $O_2$ plasma exposure. Therefore, the small decrease in apparent thickness is speculated to origin from an increase in surface roughness. Due to the combination of a $H_2$ and $O_2$ plasma, the surface could be reduced slightly under the $H_2$ plasma, and oxidized again during the $O_2$ plasma exposure, which could increase the surface roughness. Although this was not tested for $Al_2O_3$, AFM measurements (in chapter 5) showed a drastic increase in surface roughness of Co samples when performing ABDC-type ALD cycles. Also, the apparent thickness is decreasing overall in the ADC cycles, showing a small etching component (EPC = 0.1 Å/cycle.) Compared to the EPC of 0.04 Å/cycle obtained when performing a combination of Hacac doses and $H_2$ plasma exposures, this shows that the combination of plasmas affects the apparent thickness measured with ellipsometry.

In the second part of the graph, three full ABDC cycles have been performed onto the $Al_2O_3$ substrate. After the adsorption of Hacac, the precursor is dosed. Dosing of BDEAS on the adsorbed inhibitor does not result in a significant change of apparent thickness, indicating that the inhibitor is able to block precursor adsorption. For the two subsequent plasma exposures in the ABDC cycles, a decrease of apparent thickness is visible indicating removal of adsorbed inhibitor. However, since the inhibitors are completely removed by the $H_2$ plasma, the decrease in apparent thickness due to the $O_2$ plasma is not expected in ABDC-type cycles. The combination of $H_2$ and $O_2$ plasma exposures might affect the surface, resulting in a change in the apparent thickness measured with ellipsometry. It is not fully understood why the apparent thickness decreases for the $O_2$ plasma exposure, and therefore it would be interesting to investigate this further. In chapter 5, the combination of plasma exposures in ABDC-type ALD cycle was shown to affect the Co substrate, increasing the surface roughness significantly. Similarly, the $Al_2O_3$ surface could be affected by the combination of plasmas. Overall, when looking at the data points after full ABDC cycles, the apparent thickness does not increase. This indicates blocking of $SiO_2$ ALD on $Al_2O_3$.

In the third part of the graph, three BDC-cycles have been dosed onto the $Al_2O_3$ substrate. In these cycles, no inhibitor is being dosed on the surface. When precursor is dosed, the apparent thickness increases indicating adsorption of precursor. Consequently, the combination of $H_2$ and $O_2$ plasmas results in a thickness decrease, indicating removal of precursor ligands. Both the $H_2$ and the $O_2$ plasmas remove part of the precursor ligands. Since the precursor ligands are partially removed by the $H_2$ plasma, a shorter $O_2$ plasma might be sufficient to obtain ALD of $SiO_2$. In chapter 5, a shorter $O_2$ plasma exposure time was shown to mitigate damage to the non-growth area, while still depositing $SiO_2$ on the growth area. Overall, the GPC over these three BDC cycles equals 0.7 Å/cycle. This value is somewhat lower than the usual GPC for $SiO_2$ at operating conditions (0.9 Å/cycle.) However, determining the GPC over only three cycles is not accurate, and in section 4.2.2 it is shown that the GPC is unaffected by the addition of the $H_2$ plasma exposure.

The subcycle data shows, similar to the results in chapter 3, that Hacac adsorbs on the $Al_2O_3$ surface, and precursor adsorption is blocked. Furthermore, the combination of plasmas seems to fully remove the adsorbed inhibitor, and it has been shown that without inhibitor, $SiO_2$ can be deposited on $Al_2O_3$.

### 4.2.2 Determining the nucleation delay with *in situ* ellipsometry

Figure 4.6 shows the thickness measured by *in situ* ellipsometry as a function of the number of ALD cycles on (A) $Al_2O_3$ and (B) $SiO_2$ starting surfaces for (standard) BC, ABC and ABDC-type cycles. The $H_2$ plasma exposure has been optimized, which is discussed later. Figure 4.6 A shows immediate nucleation for (standard) BC cycles, and a nucleation delay of approximately 15 cycles for ABC-type ALD cycles. The nucleation delay is determined by selecting the point where the slope of the nucleation curve significantly changes from zero. The nucleation delay of 15 cycles using ABC-type cycles agrees with the results obtained in earlier research, as shown in chapter 3. Furthermore, the nucleation delay on $Al_2O_3$ increased significantly by adding a 25 s $H_2$ plasma exposure step (600 W, 300 mTorr) to ABC-type ALD cycles, resulting in ABDC-type ALD cycles. For ABDC-type cycles, nucleation occurs only after approximately 30 cycles.

In figure 4.6 B, the thickness as a function of number of ALD cycles on $SiO_2$ is shown. Because the inhibitor does not adsorb on the surface, linear growth is observed for all three processes. The slight difference in the slope of the graph (indicating the GPC) is believed not to be significant. In conclusion, it can be concluded that the selectivity has been increased significantly. Using ABDC-type cycles, selective deposition of $\sim 2.5$ nm is achieved.

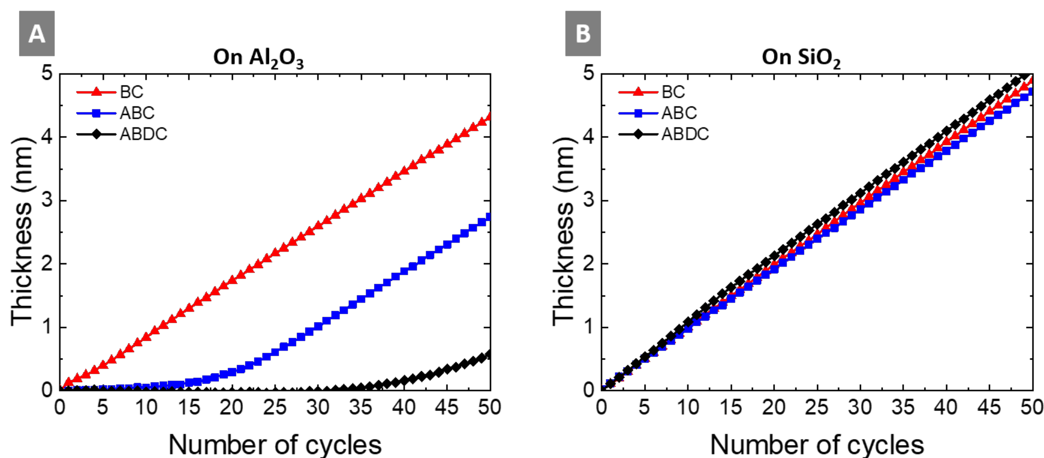


**Figure 4.6:** *In situ* ellipsometry measurements on selective deposition for BC, ABC and ABDC-type ALD of $SiO_2$ on (A) $Al_2O_3$ and (B) $SiO_2$.

As stated before, various $H_2$ plasma exposure times were investigated to optimize the nucleation delay (depicted in figure 4.7 A). For the removal of adsorbed Hacac from the surface, a combination of high radical flux to the surface, while limiting the ions energies on the surface is desired. The high radical flux enables the formation of volatile Hacac on the surface, and limiting the ion energies reduces damaging of the surface. Therefore, the plasma power and pressure during plasma exposure has been chosen at 600W, 300 mTorr. These values are the maximal operating plasma power and pressure for the used setup. Figure 4.7 shows the nucleation delay measured using ABDC-type cycles for different $H_2$ plasma exposure times.

Figure 4.7 A shows the nucleation curves measures for a varying $H_2$ plasma exposure time. The nucleation delay was determined from these nucleation curves, and the determined nucleation delay for different $H_2$ plasma exposures is given in figure 4.7 B, showing an optimum. The

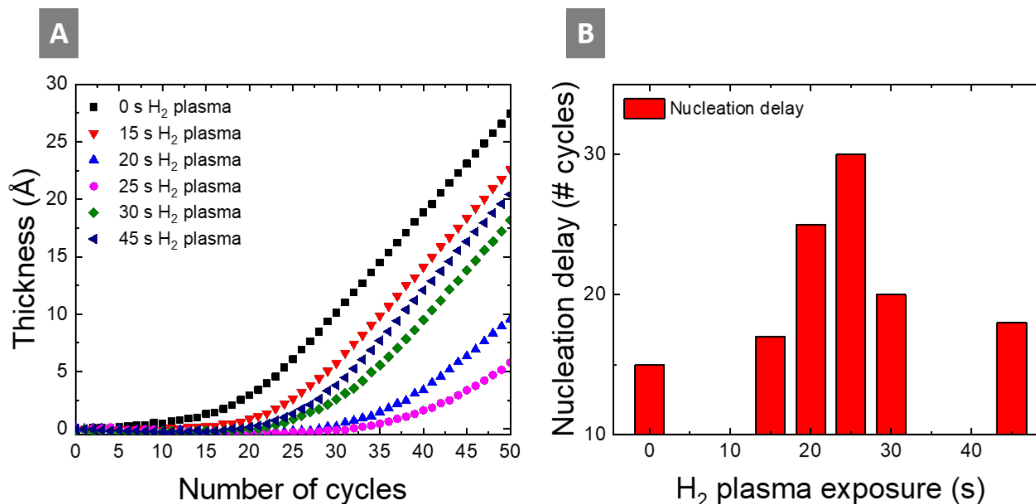


**Figure 4.7:** Nucleation delay for ABDC cycles measured for different $H_2$ plasma exposures on $Al_2O_3$. (A) *In situ* ellipsometry measurements of the nucleation curve for varying $H_2$ plasma exposures. (B) Determined nucleation delay for different $H_2$ exposure times, where the maximum nucleation delay is achieved at 25 s.

nucleation delay increases up to a plasma exposure of 25 seconds, but decreases when a longer plasma step is performed. On one hand, the nucleation delay increases for an increasing $H_2$ plasma exposure by fully removing the acac ligands from the surface. On the other hand, the decrease of nucleation delay for plasma exposures over 25 seconds, is speculated to originate from the combination of reduction and oxidation of the $Al_2O_3$ substrate. Excessive reduction and oxidation of the substrate might damage the surface, resulting in an increased surface roughness. In chapter 5, AFM measurements indicated that performing ABDC-type ALD cycles on Co resulted in a significant increase in surface roughness. A more rough surface could result in a less densily packed Hacac layer on the surface. This way, nucleation sites for the $SiO_2$ ALD can be created, which results in ALD growth on the non-growth area.

The maximum nucleation delay has been achieved using a 25 second $H_2$ plasma exposure. As shown in figure 4.7 B, the obtained nucleation delay is approximately 30 cycles. The measurement resulting in the maximal nucleation delay was performed multiple times, and reproducibility was shown. For future research, it would be a valuable addition to vary both the $O_2$ and $H_2$ plasma exposures. Since the oxygen plasma is not fully responsible for removal of the inhibitor ligands anymore, it could be possible to reduce the $O_2$ plasma exposure time (as shown in chapter 5 for Co substrates.) Reducing the $O_2$ plasma will cause less damage to the substrate and might result in an even longer nucleation delay.

The ellipsometry data from figure 4.6 A, showing the optimized nucleation delay for BC, ABC and ABDC-type ALD cycles, was fitted using the model described in section 2.3.2. The data with fitted nucleation delay is depicted in figure 4.8. The model takes three variables into account; $\dot{G}$, $\widehat{N}$ and $\dot{N}$. $\dot{G}$ is the GPC of the process when linear growth is observed. The GPC is determined by taking the slope of a linear fit through the BC data, where uninhibited growth is observed, which resulted in $\dot{G} = 0.086$ nm/cycle. $\widehat{N}$ is the number of nucleation sites present on the starting surface, and $\dot{N}$ is the number of nucleation sites generated per cycle.

Since these variables are correlated, one is chosen to be zero. Because the plasma pretreatment is believed to remove all of the nucleation sites from the starting surface, $\widehat{N} = 0$ is used. Now fitting of the data results in a value for the number of nucleation sites generated per ALD cycle. The values for $\dot{N}$ provide general insight into the nucleation behaviour, and can be used to compare nucleation delays for different processes. For ABC-type ALD cycles, $\dot{N} = 8 \cdot 10^{-3}$ ($nm^{-2}$ $cycle^{-1}$), and for ABDC-type ALD cycles, $\dot{N} = 3 \cdot 10^{-4}$ ($nm^{-2}$ $cycle^{-1}$). These values demonstrate that generation of nucleation sites is slower for ABDC cycles, corroborating the increase in nucleation delay by addition of the $H_2$ plasma. Furthermore, these values can be compared to the number of -OH groups on a $Al_2O_3$ substrate. The experimentally obtained hydroxyl density of a pristine $Al_2O_3$ surface is approximately 9 $nm^{-2}$.[76] Earlier FTIR experiments have shown that on $Al_2O_3$-coated powder samples, that adsorbed Hacac molecules limit the adsorption of a single BDEAS dose to 8% of the normal adsorption.[58] The values obtained from fitting the nucleation delay suggest that only 0.09 % of the surface sites allow nucleation. Because the nucleation delay is measured on a wafer sample, a more defect-free inhibiting layer is expected to form. The values obtained emphasize how well adsorbed Hacac is able to block BDEAS adsorption on $Al_2O_3$, and prove that adding a $H_2$ plasma is able to improve the blocking significantly.

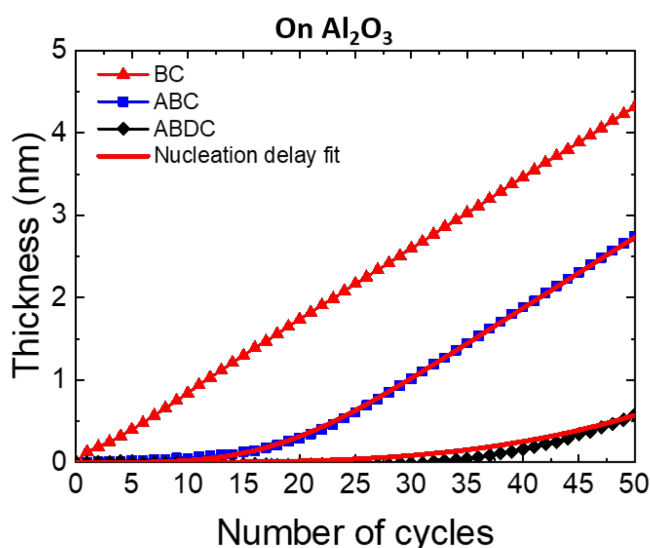


**Figure 4.8:** *In situ* ellipsometry measurements of the nucleation delay for BC, ABC and ABDC-type ALD of $SiO_2$ on $Al_2O_3$. The data (also shown in figure 4.6) was fitted using the model explained in section 2.3.2, with $\dot{G} = 0.086$ nm/cycle, $\widehat{N} = 0$ $nm^{-2}$. The values obtained for $\dot{N}$ are $8 \cdot 10^{-3}$ $nm^{-2}$ $cycle^{-1}$ for ABC cycles, and $3 \cdot 10^{-4}$ $nm^{-2}$ $cycle^{-1}$ for ABDC cycles.

### 4.2.3 XPS corroboration of the nucleation delay

X-ray photoelectron spectroscopy (XPS) has been used to corroborate the results obtained with ellipsometry. The Si 2p peak has been used to investigate the deposition of $SiO_2$ on the $Al_2O_3$ substrates. Since the XPS measurements have been done *ex situ*, every measurements has been done on a separate sample. Figure 4.9 shows the Si 2p peaks from XPS for different numbers of ALD cycles for BC, ABC and ABDC cycles.

The BC graph gives the Si 2p peak for $SiO_2$ ALD cycles without using an inhibitor, as a reference for standard ALD. The full spectra are shown in appendix B. For 5 ALD cycles, which corresponds to a little under 0.5 nm of $SiO_2$, the Si 2p peak maximum is around 5000 counts/s. When comparing the ABC and ABDC cycles with this deposition, it is clear that nucleation is delayed using inhibitor molecules. Also, addition of the $H_2$ plasma shows an increased nucleation delay. For instance, looking at the 25 ABDC cycle graph, it is clear that there is less $SiO_2$ deposition than for the 20 ABC cycle graph. The reference shows that these amounts of cycles are still under 5 normal ALD cycles worth of growth. This corroborates the results obtained with ellipsometry experiments, showing that the nucleation delay has been increased by adding a $H_2$ plasma step into the previously examined ABC-type ALD process. However, XPS is more sensitive for small amounts of species on the surface then ellipsometry. It is shown that even for 5 ABDC cycles, some trace amount of deposition is already on the $Al_2O_3$ surface. Although this nucleation was not detectable using ellipsometry, earlier FTIR experiments also showed a small amount of nucleation in the first cycles.[58] This coincides with the assumption made in the model used to fit the ellipsometry data, where nucleation sites are being generated in every cycle.

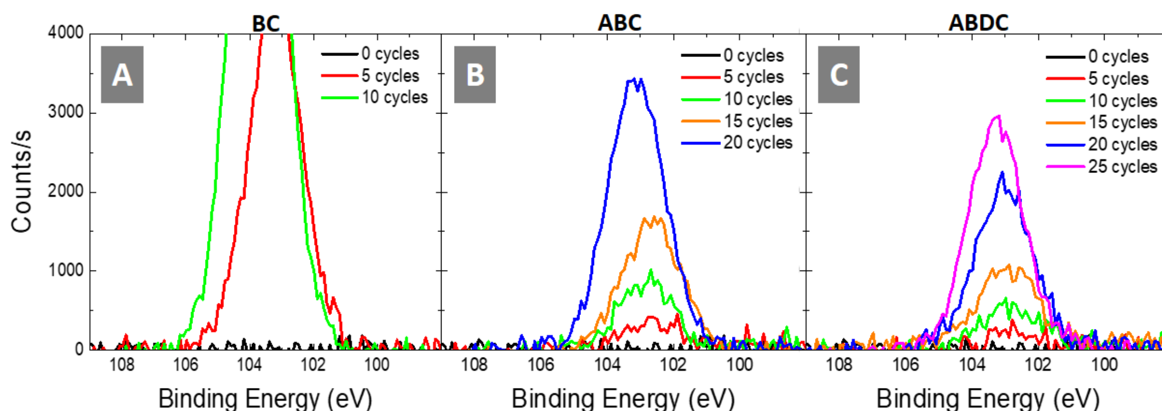


**Figure 4.9:** XPS measurements of the Si2p peak for different number of ALD cycles on $Al_2O_3$. The increase in Si2p peak is indicated for (A) BC, (B) ABC and (C) ABDC cycles, corroborating the increased nucleation delay observed with ellipsometry.

Since the areas of the Si 2p peaks from figure 4.9 are a measure for the amount of $SiO_2$ deposition, these peaks have been integrated to show the nucleation delay. The integrated areas have been plotted in figure 4.10. This graph corroborates the nucleation delay measured by ellipsometry, proving that the nucleation delay is increased by the addition of a $H_2$ plasma exposure step.

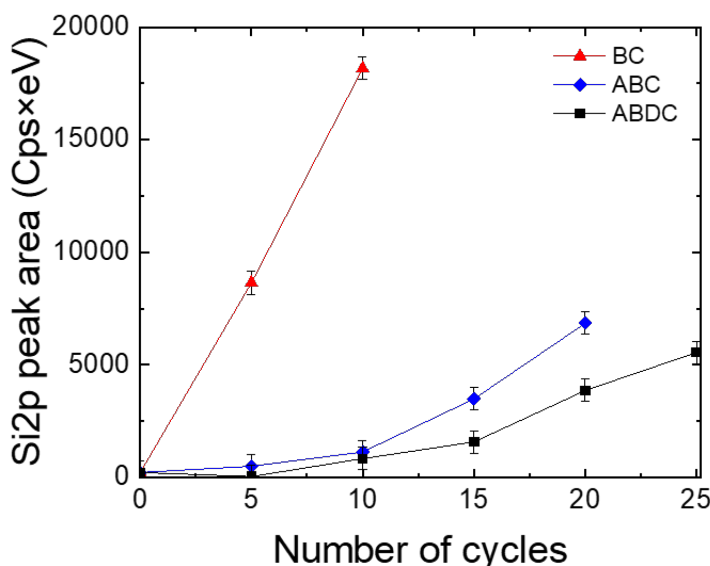


**Figure 4.10:** Integrated Si2p peaks from XPS for an increasing number of ALD cycles on $Al_2O_3$ (from figure 4.9.) This data shows the nucleation delay has been increased by addition of a $H_2$ plasma exposure.

## 4.3 Conclusion

In this chapter, the area-selective deposition process based on ABC-type cycles as studied by Mameli *et al.*[29] was improved by adding a $H_2$ plasma exposure step. The $H_2$ plasma completely removed inhibitor ligands, and this resulted in an increased nucleation delay. The nucleation delay was fitted by the model explained in section 2.3.2, which quantified the nucleation delay for future comparisons. Both ellipsometry and XPS measurements demonstrated an increase in selectivity by adding a $H_2$ plasma step. Using the ABDC-type process, selective deposition of $\sim 2.5$ nm can be achieved.

However, some further investigation could help understanding this process better. It was shown that the combination of $H_2$ and $O_2$ plasma steps affected the surface. The ellipsometry subcycle experiments in section 4.2.1 showed an significant etching component, which is speculated to originate from an increased surface roughness. Furthermore, the nucleation delay reaches an optimum for a certain $H_2$ plasma exposure. This is speculated to originate from deformation of the surface, resulting in a less effective blocking layer. Clearly, studying the influence of the combination of plasmas on the surface would help better understand the initiation of nucleation on the non-growth area. For Co, the effect of the plasmas on the surface is shown in chapter 5. Additionally, more experiments to mitigate damages to the non-growth area are proposed in chapter 7.

# Chapter 5

# Area-selective ALD of $SiO_2$ in the presence of Co

In this chapter, area-selective ALD of $SiO_2$ using Hacac as the inhibitor with cobalt as the non-growth area is studied. The nucleation delay on Co is investigated for both ABC- and ABDC-type cycles. Furthermore, the effect of the ALD chemistry on the morphology of the Co is examined using both AFM and SEM.

The composition of the cobalt substrates was characterized with an XPS depth profile, which is shown in appendix C. The Co was exposed to either a 5 minute $O_2$ plasma pretreatment or a 5 minute $H_2$ plasma pretreatment, depending on the experiments conducted. As depicted in figure 5.1, oxidized cobalt was used to investigate the ABC-type ALD cycles and reduced cobalt was used to investigate the ABDC-type ALD cycles.

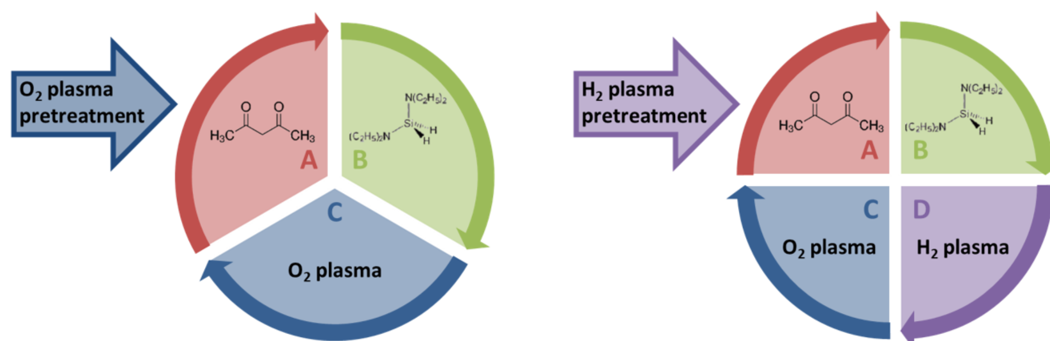


**Figure 5.1:** Schematic of the ABC- and ABDC-type cycles used on cobalt substrates, with their respective pretreatments. $CoO_x$ is used to study ABC-type cycles, and reduced Co is used to study ABDC-type cycles.

For the application of area-selective ALD in self-aligned VIAs, the required state of the Co after deposition is conducting (i.e. non-oxidized). However, due to the $O_2$ plasma used during ALD of $SiO_2$, the substrate oxidizes to some extend. Because it is not possible to accurately model the repeated oxidation and reduction of the substrate in ellipsometry while depositing on a reduced sample, the more stable $CoO_x$ (Co after a 5 minute $O_2$ plasma) has been used

to investigate ABC-type cycles with ellipsometry. For ABDC-type cycles, XPS was used to measure the nucleation delay, enabling the use of reduced cobalt substrates. Besides removal of the inhibitor, the included $H_2$ plasma exposure also mitigates the oxidation of the Co.

## 5.1 Area-selective ALD of $SiO_2$ in the presence of oxidized cobalt

In order to gain insight into the adsorption and removal of inhibitor and blocking of precursor adsorption during ABC-type ALD cycles on $CoO_x$, ellipsometry subcycle experiments (as explained in chapter 2) were conducted. The apparent thickness was determined after each dose for different combinations of doses and the results are depicted in figure 5.2. The Co substrate more prone to oxidation and reduction than the $Al_2O_3$ substrate, and therefore the error in ellipsometry fitting is relatively big.

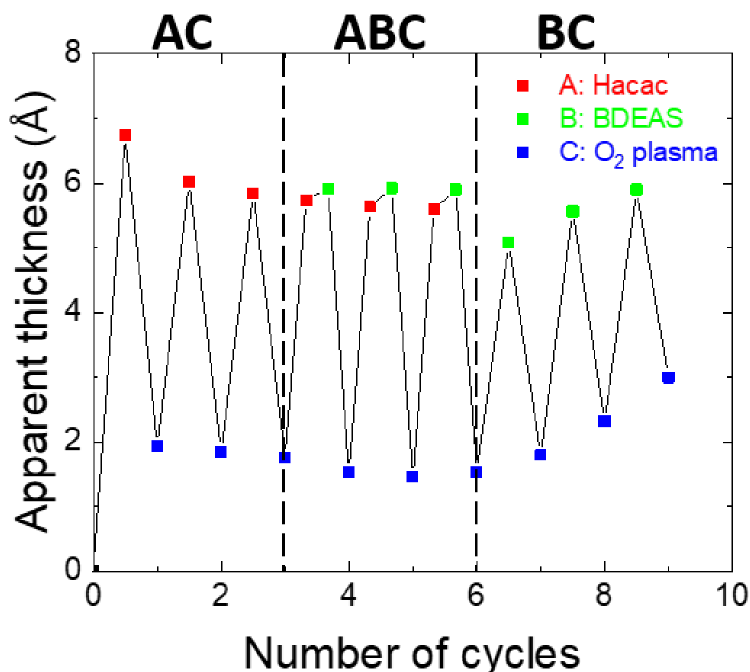


**Figure 5.2:** Apparent thickness as a function of the number of cycles from *in situ* ellipsometry for subcycle experiments on oxidized cobalt. The left part shows doses of inhibitor and $O_2$ plasma (AC), the middle part illustrates the full ALD cycles (ABC) and the right part shows normal ALD without using an inhibitor (BC). The dosing times used for this experiment are given in figure 2.3 A.

The first part of the graph shows the apparent thickness during three AC cycles (dosing of inhibitor and $O_2$ plasma), performed on $CoO_x$. Firstly, the increase in apparent thickness indicates adsorption of Hacac on the $CoO_x$. Secondly, the sample is exposed to a $O_2$ plasma step. The apparent thickness decreases, but the fact that the thickness does not decrease to zero indicates only partial removal of the adsorbed acac molecules.

The middle part of the graph shows the apparent thickness evolution during subsequent dosing of three full ABC-type cycles. After adsorption of Hacac (A), the BDEAS precursor is dosed (B), resulting in a small increase in apparent thickness. This could indicate that a fraction of the precursor adsorbs on the surface, which suggests the adsorbed Hacac is not able to fully block precursor adsorption. However, during the $O_2$ plasma exposure, the thickness reduces to approximately the same thickness as before the ALD cycle. Besides, the apparent thickness over the complete ABC cycle does not significantly increase, which shows that ALD is blocked by the inhibitor.

The third part of the graph shows the apparent thickness during subsequent exposure to three BC cycles, which are standard $SiO_2$ ALD cycles without an inhibitor dose. Dosing the BDEAS precursor causes an increase in apparent thickness, indicating precursor adsorption. After the $O_2$ plasma exposure, the apparent thickness decreases which complies with precursor ligand removal. Overall, the apparent thickness increases, indicating deposition of $SiO_2$.

The subcycle data demonstrates that Hacac adsorbs on the $CoO_x$ surface, and that the adsorbed Hacac blocks precursor adsorption. However, similar to the results for ABC-type cycles on $Al_2O_3$ as presented in chapter 4, the inhibitor molecules are not fully removed from the surface by the $O_2$ plasma exposure. As studied in chapter 4, the removal of the inhibitor molecules can be improved by implementing a $H_2$ plasma exposure, which will be applied later in this chapter.

Figure 5.3 shows the thickness for both BC- and ABC-type ALD cycles of $SiO_2$ on $CoO_x$ measured by *in situ* ellipsometry as a function of the number of ALD cycles. The nucleation curve for BC cycles has been included, to show the influence of the inhibitor on the ALD process. This data corroborates that the nucleation delay for ABC-type cycles is due to the addition of inhibitor molecules to the process. Performing ABC-type cycles on $CoO_x$, as shown in figure 5.3, results in a nucleation delay of approximately 20 cycles. It was previously shown (in figure 4.6 B) that the inhibitor does not affect the GPC of ALD of $SiO_2$ on the growth area. Therefore, the obtained nucleation delay of approximately 20 cycles results in a selective deposition of $\sim$ 2 nm.

In the first 20 cycles, the thickness increases slightly for ABC-type cycles on oxidized cobalt. However, in terms of the slope this is clearly different from deposition of $SiO_2$ on the surface. This slight increase can likely be attributed to the fact that the cobalt oxidizes during the $O_2$ plasma exposure every cycle. Even after a long (5 minute) plasma pretreatment, the $O_2$ plasma exposure has an effect on the cobalt substrate. Separate measurements showed that after the 5 minute plasma pretreatment, another subsequent minute of $O_2$ plasma exposure resulted in an apparent thickness increase of $\sim$ 3 Å. This shows that the measurement uncertainty of these ellipsometry measurements increases as a function of number of cycles.

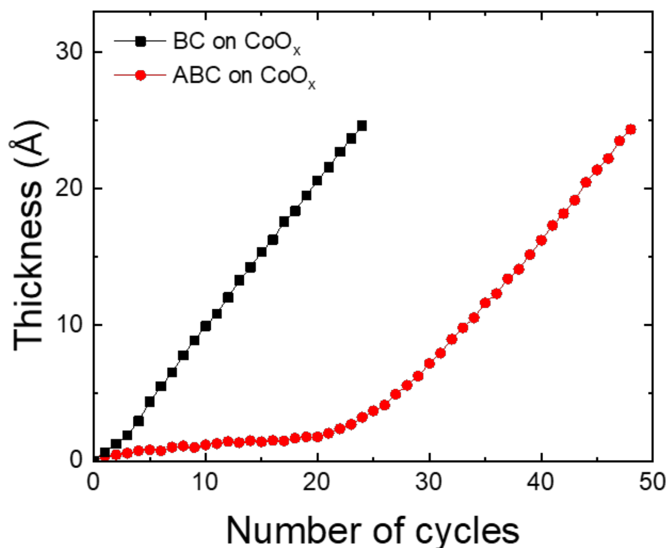


**Figure 5.3:** *In situ* ellipsometry measurements of the nucleation behaviour of BC and ABC-type ALD of $SiO_2$ on oxidized cobalt substrates. For ABC-type cycles, a nucleation delay of approximately 20 cycles is observed, resulting in area-selective ALD of $\sim$ 2 nm using $SiO_2$ as the growth area.

The data also shows that the nucleation delay for ABC-type cycles depends on the starting substrate. For instance, the nucleation delay on oxidized cobalt (20 cycles) is longer than the nucleation delay on $Al_2O_3$ (15 cycles). The loss of selectivity is caused by incomplete blocking of the precursor, which can occur most likely due to (a combination of) three factors.[29] First, the presence of surface defects or impurities can negatively influence the inhibitor adsorption behaviour. Second, it is possible that surface reactive sites remain accessible to the precursor due to an imperfect coverage of inhibitor molecules. Third, physisorbed water molecules on the surface can compete with Hacac adsorption, also resulting in an incomplete inhibitor layer. The difference in nucleation delay on different substrates is a result of the packing density of the adsorbed inhibitor layer.

In this case, the $O_2$ plasma pretreatment is expected to remove most of the surface impurities. This means that the loss of selectivity is caused by nucleation sites being generated during the ALD cycles. Nucleation sites can be generated the adsorbed Hacac molecules are not able to fully block precursor adsorption. When fitting the data from figure 5.3 with the Avrami model (see section 2.3.2), the best fit is achieved for $\dot{G} = 1.03$, $\widehat{N} = 0$ and $\dot{N} = 2.2e - 5$, which indicates formation of nucleation sites during the deposition process. However, since the apparent thickness increases in the first few cycles due to oxidation, the fit is not entirely accurate.

## 5.2 Area-selective ALD of $SiO_2$ in the presence of reduced cobalt

It is shown in chapter 4 that a $H_2$ plasma exposure increases the selectivity by fully removing the inhibitor molecules from the surface. Therefore, the $H_2$ plasma exposure was also included for area-selective ALD on Co, resulting in ABDC-type ALD cycles. During initial experiments, the combination of $H_2$ and $O_2$ plasmas was shown to change the optical response of the substrate too much to allow for accurate ellipsometry fitting. Since the required state of the Co after deposition for the application in self-aligned VIAs is conducting (i.e. non-oxidized), ABDC-type ALD was investigated on reduced Co. This cobalt is exposed to a 5 min $H_2$ plasma pretreatment, to reduce the native oxide from the surface. Since the repeated oxidation and reduction cannot be modelled accurately using ellipsometry fitting, XPS is used to investigate the nucleation behaviour of ABDC-type cycles on reduced Co.

When performing ABDC-type cycles on $Al_2O_3$, a small etching component was shown using ellipsometry (due to the formation of $Al(acac)_3$, as discussed in section 4.1.) Since XPS only measures the chemical composition of the surface, etching of the substrate is not investigated. However, both $Co(acac)_2$ and $Co(acac)_3$ are volatile reaction products that can introduce an etching component during ABDC-type cycles on Co. It is not known whether etching occurs during these cycles. On the other hand, when looking at the application of self-aligned VIAs, a small etching component of the metal lines would be helpful. Etching of the Co would, like the recess etch currently used, help forming a pattern with dielectric barriers as shown in figure 1.9 D.

Figure 5.4 shows the Si 2s peak for different numbers of BC and ABDC-type ALD cycles on $Al_2O_3$ and reduced Co respectively. The Si 2s peaks are used as a measure for the amount of $SiO_2$ deposition instead of the Si 2p peak, since the Si 2p peak overlaps with the Co 3s peak. XPS measurements have been done *ex situ*, so every measurement has been performed on a separate sample. Figure 5.4 A gives a reference for the Si 2s peak intensity for $SiO_2$ ALD cycles on $Al_2O_3$ without using an inhibitor, and figure 5.4 B gives the Si 2s peaks for ABDC cycles on reduced cobalt. These graphs show that up to 25 ABDC cycles, there is no deposition of $SiO_2$ on the reduced cobalt, which corresponds to selective deposition of $\sim$ 2.5 nm. The 25 ABDC-type cycle deposition was repeated three times and no $SiO_2$ deposition was detected in all cases. However, after 30 ABDC cycles, the Si 2s peak intensity increases rapidly. The peak intensity for 30 cycles is higher than the peak observed for 5 BC cycles (the integrated areas are shown in figure 5.5), which suggests more than 5 ALD cycles worth of $SiO_2$ deposition are deposited during cycle number 25 to 30. In addition to the abrupt increase in the Si 2s peak, an additional peak at 151 eV stands out. This peak indicates elemental Si from the surface itself. When depositing $SiO_2$ using BC-type ALD cycles as shown in figure 5.4A, this elemental Si peak is not visible. However, elemental Si can be found in the substrate underlying the Co on the sample. SEM was used to examine these samples, as will be discussed in section 5.3.2. The results indicated that repeated $O_2$ and $H_2$ exposures damage the surface heavily, creating pinholes and eventually dewetting of the Co. The occurrence of dewetting explaines the abrupt increase in Si 2s peak intensity, as well as the appearance of a peak indicating elemental Si.

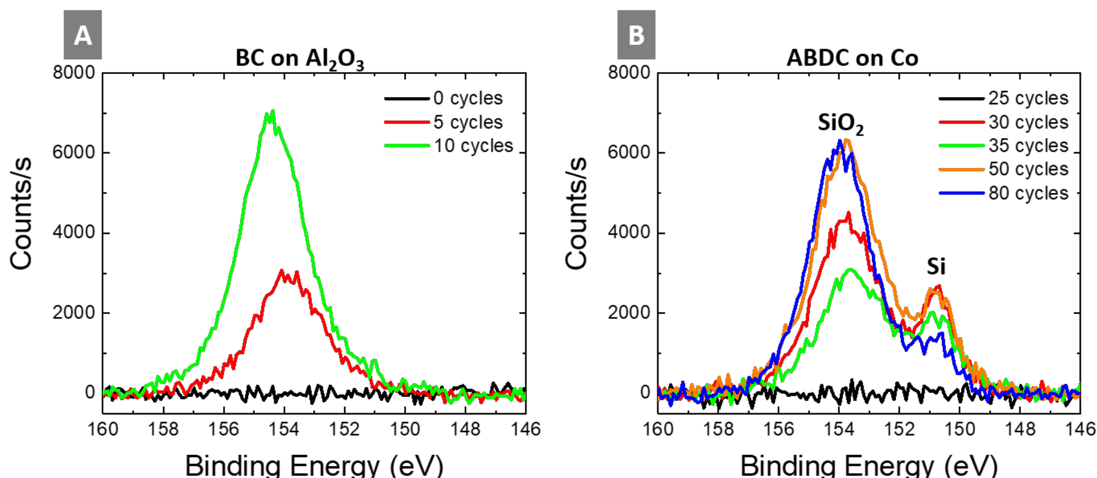


**Figure 5.4:** Si 2s peaks measured by XPS. (A) BC-type ALD cycles of $SiO_2$ on $Al_2O_3$, as a reference for normal growth. (B) ABDC-type ALD cycles on reduced cobalt. Up to 25 cycles, no deposition is visible. After 30 cycles, the Si 2s peak intensity abruptly increases, and an additional peak at 151 eV appears, indicating elemental Si.

The integrated area under the Si 2s peaks as determined from the data presented in figure 5.4 as a function of the number of cycles is given in figure 5.5. In red, the immediate and linear increase in peak area is given for BC cycles on $Al_2O_3$ as a reference for normal ALD. In black, the integrated peak area is given for ABDC-type ALD on reduced Co. The graph shows that up to 25 cycles, no significant deposition of $SiO_2$ occurs. When comparing the integrated area measured after 25 and 30 ABDC cycles, the Si 2s peak area increases abruptly, showing an increase of more than 5 cycles worth of $SiO_2$ deposition.

During the first 25 ABDC-type cycles on reduced Co, XPS showed no deposition of $SiO_2$. However, the samples discolored visibly. A picture of the discolored samples in comparison to the initial substrate is given in figure 5.6. This discoloration is believed to be due to the combination of consecutive oxidation and reduction steps. Therefore, the $O_2$ plasma exposure was decreased to 1 s, which resulted in less discoloration. The effect of the plasma exposures on the morphology was further investigated using AFM and SEM.

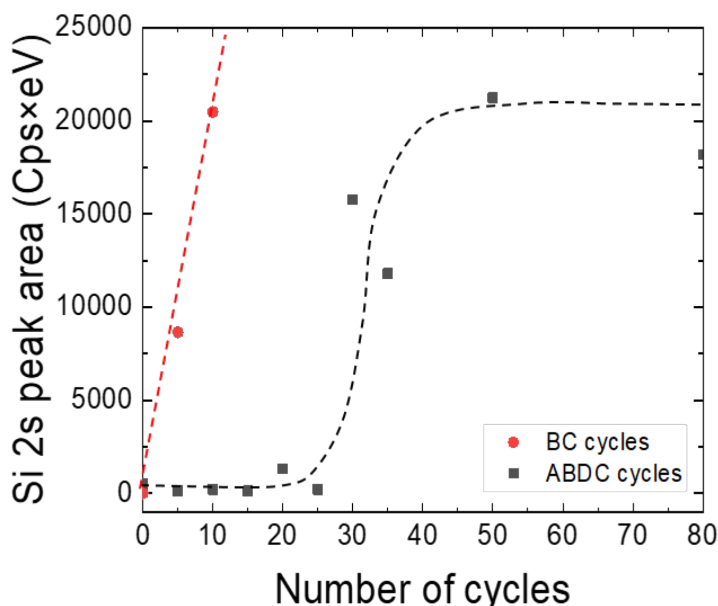


**Figure 5.5:** Integrated Si 2s peak measured by XPS as a function of number of cycles. For normal BC-type ALD cycles on $Al_2O_3$, an immediate and linear increase is observed. For ABDC-type cycles on reduced cobalt, the nucleation is delayed by at least 25 cycles. After 25 cycles, the integrated area of the Si 2s peak abruptly increases.

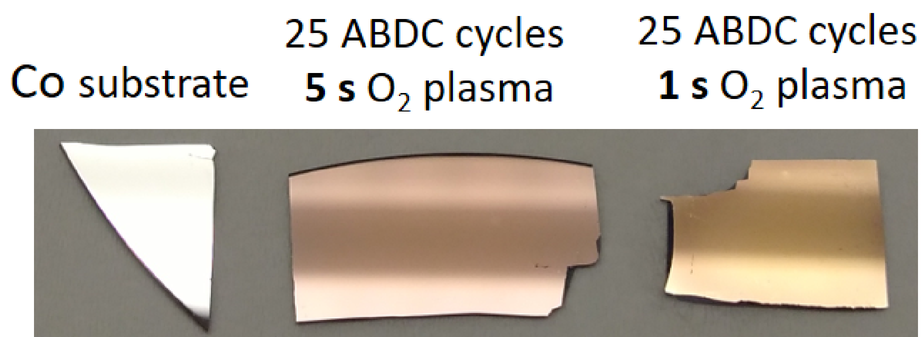


**Figure 5.6:** Picture of Co samples showing the change in color due to the ALD chemistry after dosing 25 ABDC-type ALD cycles. By reducing the $O_2$ plasma exposure time from 5 seconds to 1 second, the substrate showed less discoloration.

## 5.3 Oxidation and reduction of the cobalt substrate during ABDC-type ALD

Since both $O_2$ and $H_2$ plasmas are used in ABDC-type ALD, the Co substrate undergoes repeated oxidation and reduction. In literature, it was shown that an $O_2$ plasma is capable of fully oxidizing Co thin films to $Co_3O_4$.[77] On the other hand, a $H_2$ plasma is capable to

fully reduce a $Co_3O_4$ substrate to metallic Co.[78] In this research, it has not been investigated thoroughly to what extend the surfaces are oxidized or reduced. Therefore, further experiments are suggested in section 7.2.1. Excessive oxidation and reduction of the surface might result in damage to the substrate. For thermal reduction of Co, it has been shown that the surface morphology is modified due to tensile stress in the film, resulting in dewetting of the cobalt film.[79] Generally, dewetting evolves through three distinct stages; First, pinholes are formed on the substrate. Then, these holes grow to form dewetted regions that eventually overlap, such that the entire film dewets.[80] The process of dewetting is driven by surface energy minimization and can occur via surface diffusion, well below the melting temperature of the film, especially when the film is very thin.[81]

Dewetting of Co thin films is often shown in literature, where it is used for example in the formation of nanoparticles[82] and carbon nanotubes.[83] For the application of area-selective ALD of $SiO_2$ for self-aligned VIAs, the damage to the conducting material should remain minimal. Therefore, the effect of the ABDC-type ALD process on the surface was investigated using AFM and SEM.

### 5.3.1 AFM

The change in surface topography due to ABDC-type ALD was investigated for different $O_2$ plasma exposure durations using AFM. After investigating the saturation for the $O_2$ plasma exposure in the $SiO_2$ ALD process (as shown in appendix D), the plasma exposure was decreased to 1 second. When dosing ABDC-type cycles, the $O_2$ plasma exposure is not responsible for the removal of inhibitor. Therefore, the requirement for the $O_2$ plasma is removal of the precursor ligands on the growth area. Since the GPC was shown to be unaffected, it appears this short plasma exposure is sufficient to deposit $SiO_2$ on the growth area.

Figure 5.7 shows AFM scans of a cobalt substrate, a cobalt substrate after 25 ABDC-type cycles using a 5 s $O_2$ plasma exposure and a cobalt substrate after 25 ABDC-type cycles with a 1 s $O_2$ plasma exposure. According to XPS, after 25 ABDC cycles (see figure 5.4 B), no $SiO_2$ deposition is apparent on the surface, so the topography should only show changes in the cobalt substrate. The cobalt substrate (without pretreatment) is very smooth, with an RMS roughness value under the detection limit of 1 nm. When performing 25 ABDC cycles using a 5 second $O_2$ plasma, the roughness increased significantly, to an RMS roughness value of 5.7 nm. Since the maximal selective deposition achieved in this research is $\sim$ 2.5 nm, it is obvious why such a high roughness is not acceptable. The increase in roughness can be explained by the fact that the surface is being oxidized and reduced during every cycle, which induces stress in the substrate resulting in an increased roughness. When the $O_2$ plasma exposure is reduced to 1 s (figure 5.7 C), the RMS roughness after 25 cycles is 2.9 nm. This is an improvement as compared to the 5 second plasma exposure, which corroborates the assumption that the increase in surface roughness originates from the oxidation and reduction. However, in order to use this process for selective deposition in industry, it is vital that the roughness should be decreased even further.

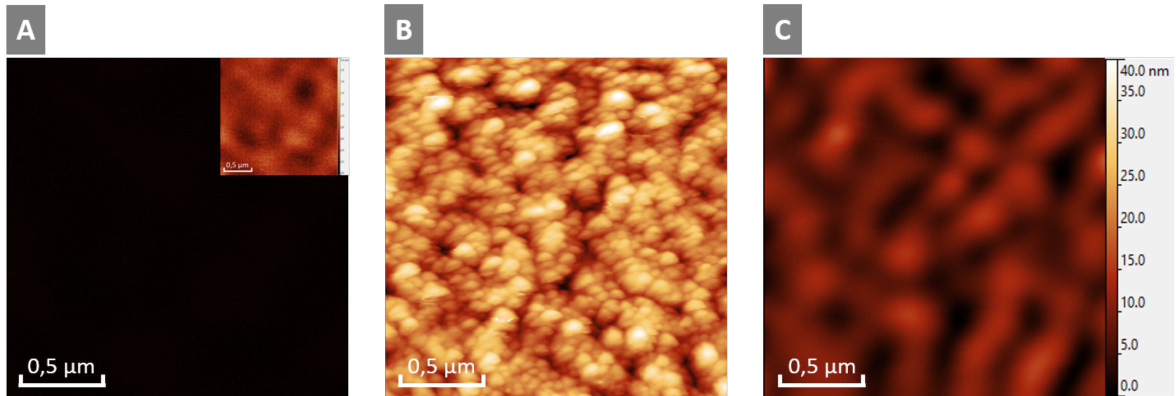


**Figure 5.7:** Surface topography plots from AFM. Figure (A) is the cobalt subtrate, (B) the Co sample after 25 ABDC cycles with a 5 second $O_2$ plasma exposure and (C) the Co sample after 25 ABDC cycles with a 1 second $O_2$ plasma exposure. The values for RMS roughness are respectively $< 1$ nm, 5.7 nm and 2.9 nm.

The roughness can potentially be decreased by further shortening the $O_2$ plasma exposure, or by decreasing the flux of O radicals to the surface. Decreasing the radical flux to the surface can be achieved by varying the plasma parameters (e.g. using a lower plasma power or higher pressure during plasma exposure.) Mitigating the deformation of the surface is not only important for the application in self-aligned VIAs, but could also further increase the nucleation delay. An increase in surface roughness could impede the formation of a densely packed inhibitor layer, affecting the nucleation delay.

### 5.3.2 SEM

Top-view SEM images were obtained to get a better understanding of what happens with the Co film during deposition. SEM images of the reduced Co substrate, and 25, 30 and 50 ABDC cycles are depicted in figure 5.8.

The top left image shows the cobalt substrate. The image shows a very fine, uniform structure, confirming the conclusion from the AFM measurements that the substrate is smooth. After 25 cycles (as shown in the top right image) some topography formed on the surface, which explains the increase in surface roughness. Also, some tiny dark dots are visible on the sample, which appear to be pinholes in the film. According to Favazza *et al.*, one of the two basic mechanisms for morphology evolution via dewetting on defect-free surfaces is homogeneous nucleation of holes followed by their growth.[82] Up to 25 cycles, XPS results from figure 5.4 showed no Si 2s peak, indicating that no deposition of $SiO_2$ occurred. Since the Co sample consists of Co deposited on Si, the absence of a Si 2s peak also indicates that the Co fully covers the underlying Si substrate. However, for 30 cycles, as shown in the bottom left image, dewetting of the Co is clearly visible. The pinholes from the top right image have grown, forming separate features of Co on the Si substrate. The formed topography proves that dewetting of the Co film occurs on the surface, which explains the abrupt increase in Si 2s peak as well as the peak indicating elemental Si from XPS. In the bottom right image, after 50 ABDC cycles, the topography formed after 30 ABDC cycles seems mostly unchanged.

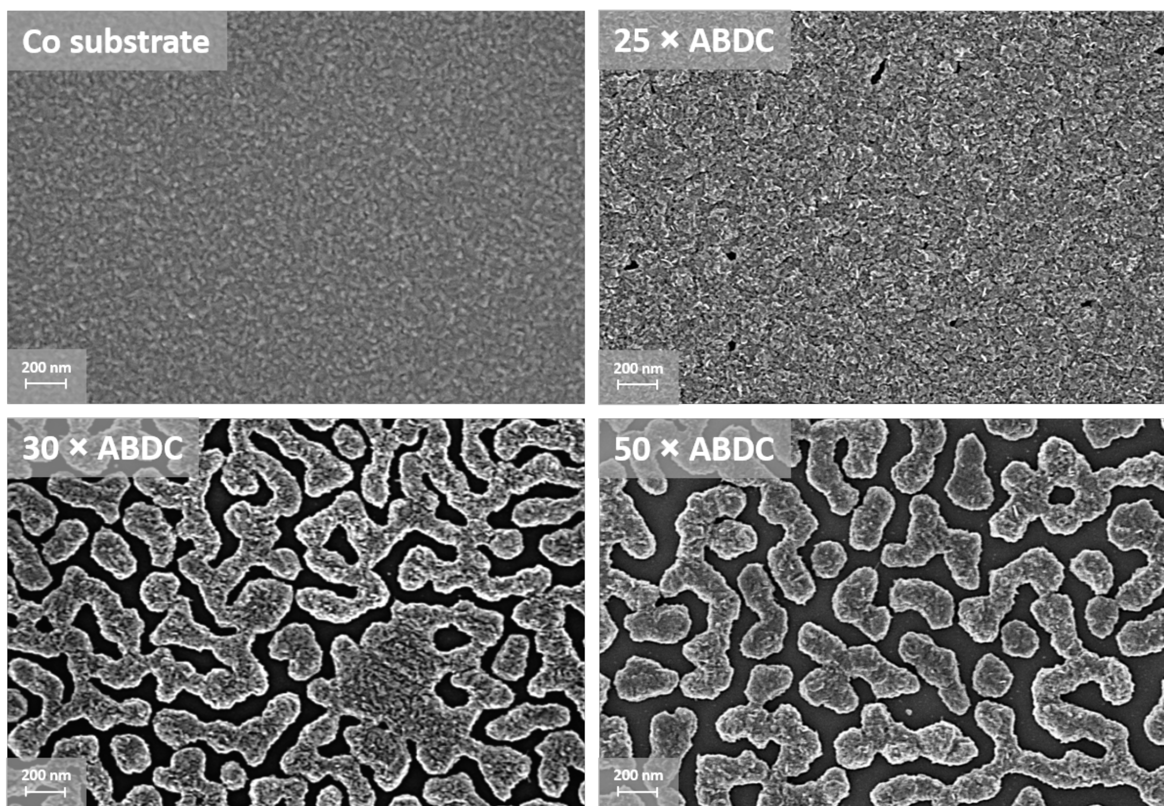


**Figure 5.8:** Top-view SEM images for different numbers of ABDC cycles performed on a Co substrate. For the film exposed to 25 cycles, small pinholes are observed Between 25 and 30 cycles, a pattern has abruptly formed on the surface, which shows dewetting of the Co. Between 30 and 50 cycles, the surface morphology has changed relatively little.

It can be concluded that the shown structure for 30 ABDC cycles is not deposition of $SiO_2$, because of two reasons. First, the diameter of the features is in the 200 nm range, which is too large for an expected 5 cycles (0.5 nm) of deposition after a nucleation delay of 25 cycles. Secondly, it would be expected when performing more ALD cycles, that a closed $SiO_2$ film would form on the surface. Even for 80 ABDC cycles, SEM imaging showed this was not the case. Therefore, it can be concluded that exposing the Co surface to the ABDC-type ALD cycles results in dewetting of the Co. Moreover, since dewetting did not occur when applying only the $H_2$ plasma pretreatment (as shown by XPS) or the ABC-type ALD cycles on $CoO_x$ (as shown by ellipsometry), it can be concluded that dewetting is caused by the repeated oxidation and reduction from the $O_2$ and $H_2$ plasma exposures.

## 5.4 Conclusion

Area-selective ALD of $SiO_2$ in the presence of cobalt was investigated. On oxidized cobalt, a nucleation delay of approximately 20 cycles was shown using ABC cycles, resulting in $\sim 2$ nm of selective growth on $SiO_2$. On reduced cobalt, XPS showed that ALD is blocked for 25 cycles, resulting in $\sim 2.5$ nm of selective growth. However, after 30 ABDC cycles, the repeated

oxidation and reduction of the substrate causes dewetting of the Co from the underlying Si. Further investigation of the dewetting of the cobalt is essential for eliminating damage to the Co surface as well as for elongating the nucleation delay, and is therefore given in section 7.2.2. Furthermore, it would be very interesting to verify whether or not area-selective ALD can be achieved using this process on a metal - dielectric patterned substrate.

# Chapter 6

# Area-selective ALD of $Al_2O_3$ on $SiO_2$ in the presence of Co

In this chapter, area-selective ALD of $Al_2O_3$ on $SiO_2$ as the growth area in the presence of Co as the non-growth area is investigated. The application of this process in VIA fabrication is selective deposition of an etch stop layer, as introduced in chapter 1. In this chapter, firstly literature is discussed to select inhibitor molecules for area-selective ALD of $Al_2O_3$. Two inhibitors were tried to achieve selective deposition. In the last section, a detailed discussion with an outlook for further research is given.

## 6.1 Selection of the inhibitor

In order to achieve area-selective ALD of $Al_2O_3$ on $SiO_2$ in the presence of Co, a suitable inhibitor has to be chosen. As stated in chapter 3, the two main requirements for the inhibitor are that it selectively adsorbs on the non-growth area, and that it is able to block the precursor adsorption. In literature, different molecules have been shown to (partially) block ALD of $Al_2O_3$ by deactivating the surface for precursor adsorption.

Yanguas-Gil *et al.* used inhibitor molecules to reduce the GPC of $Al_2O_3$ ALD.[84] In particular, Hacac was employed as an inhibitor in ABC-type ALD cycles for $Al_2O_3$. Using Hacac as the inhibitor, TMA as the precursor and $H_2O$ as the co-reactant, the GPC was reduced by 60%. From the results presented in chapters 4 and 5, it is known that Hacac adsorbs on both $Al_2O_3$ and Co. The research by Yanguas-Gil *et al.* shows that Hacac as an inhibitor partially blocks adsorption of TMA. Therefore, Hacac was tried as an inhibitor for area-selective ALD of $Al_2O_3$ on $SiO_2$ in the presence of Co. Figure 6.1 explains the possibility of area-selective ALD when the inhibitor also adsorbs on the growth area. Area-selective ALD (with a reduced GPC as indicated by Yanguas-Gil *et al.*) can be achieved if the inhibitor blocks precursor adsorption better on Co than on both $SiO_2$ and $Al_2O_3$.

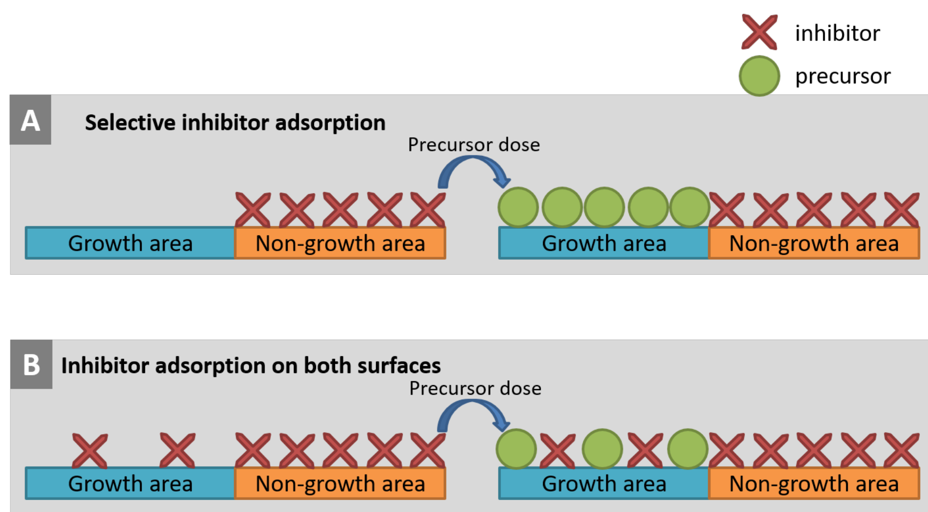


**Figure 6.1:** Schematic illustration of inhibitor molecules blocking precursor adsorption. (A) Ideally, the inhibitor adsorbs with perfect selectivity on the non-growth area, blocking precursor adsorption. (B) If the inhibitor adsorbs on both surfaces, it is still possible to achieve area-selective ALD, granted that the inhibitor blocks precursor adsorption better on the non-growth area than on the growth area.

Hashemi *et al.* demonstrated area-selective ALD of ZnO on $SiO_2$ in metal-dielectric patterns (Cu and $SiO_2$) using octadecylphosphonic acid (ODPA) SAMs as a passivating layer.[25] Knowledge from SAM literature is used here as a starting point for the choice of inhibitor. ODPA SAMs adsorb on Cu and not on $SiO_2$, due to the phosphonic acid head group. Another study by Seo *et al.*, showed area-selective ALD of $Al_2O_3$ using ODPA as a SAM.[85] Since the SAM monomers selectively adsorb on metal in the presence of dielectric material with the phosphonic acid headgroup, this is a good starting point. However, formation of a densely-packed ODPA SAM on Cu is a solution-based process which takes 48 hours.[86] In order for this method to be applicable in industry, a volatile molecule is required that can be dosed in gas-phase. Vinylphosphonic acid (VPA), as shown in figure 6.2, is a possible candidate. Due to the small size and high volatility of this molecule, adsorption is expected to take place on a much shorter time-scale. Therefore, VPA was tested to obtain a nucleation delay for ALD of $Al_2O_3$ on Co.

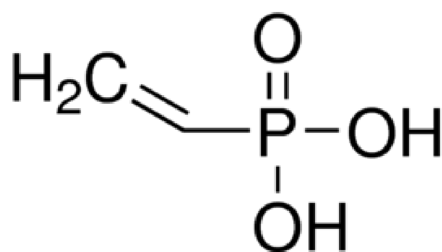


**Figure 6.2:** Structural formula of vinylphosphonic acid (VPA), consisting of a phosphonic acid headgroup, and a short double-bonded carbon 'tail'.[39]

## 6.2 Investigating Hacac as the inhibitor for area-selective ALD of $Al_2O_3$

Hacac was investigated as an inhibitor for area-selective ALD of $Al_2O_3$ on $SiO_2$ in the presence of Co. $Al_2O_3$ can be deposited using either either thermal ALD (using TMA and $H_2O$) or plasma-assisted ALD (using TMA and an $O_2$ plasma exposure) as explained in chapter 1. ABC-type ALD processes for both thermal and plasma-assisted ALD were investigated on oxidized cobalt (Co prepared using a 5 minute $O_2$ plasma pretreatment) and $SiO_2$ substrates. Figure 6.3 shows the *in situ* ellipsometry results for ABC-type ALD of $Al_2O_3$ on both $CoO_x$ and $SiO_2$ using thermal and plasma-assisted ALD. The initial experiments discussed this section were a proof-of-concept, and have not been checked for reproducibility.

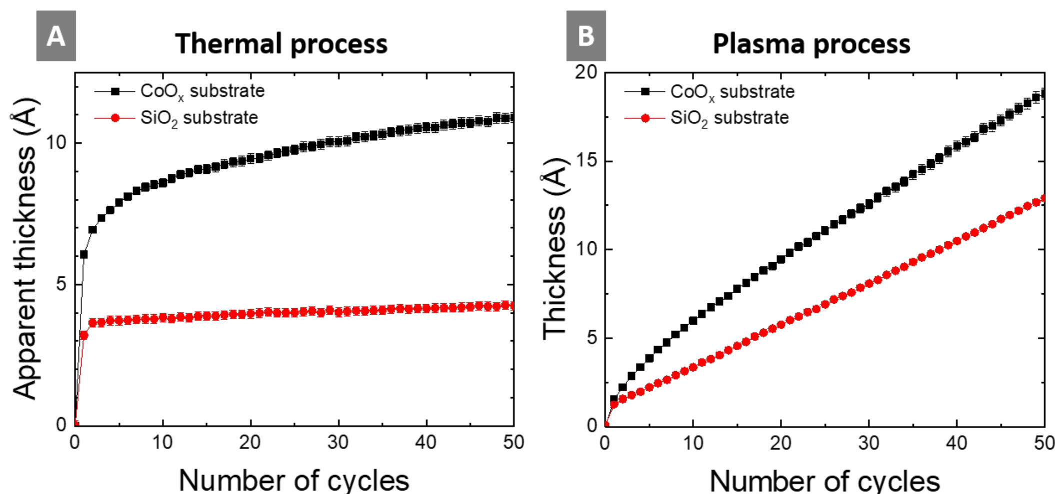


**Figure 6.3:** *In situ* ellipsometry measurements for ABC-type ALD of $Al_2O_3$ on $SiO_2$ and $CoO_x$, using Hacac as the inhibitor. The thickness as a function of the number of ALD cycles is shown for (A) thermal ALD (using TMA + $H_2O$), and (B) plasma-assisted ALD (using TMA + $O_2$ plasma).

Using Hacac as the inhibitor for thermal ALD of $Al_2O_3$, as shown in figure 6.3 A, shows little to no deposition after the first few cycles on both substrates. First, an increase in thickness on both surfaces is apparent. These two increasing apparent thicknesses in the first cycle are caused by two different mechanisms. On oxidized cobalt, the adsorption of Hacac causes a big increase in apparent thickness, which was also shown during the subcycle experiments for area-selective ALD of $SiO_2$ in section 5.1. For the $SiO_2$ substrate, the initial increase in apparent thickness does not originate from adsorption of Hacac. In the subcycle experiments in section 3.2, it was shown that only a small amount of Hacac adsorbs on the $SiO_2$ surface. This means that the initial increase in apparent thickness in figure 6.3 originates from ALD of $Al_2O_3$. However, the increase in the first cycle is bigger that the GPC of $Al_2O_3$ ALD (1 Å/cycle). This can be explained by incorporation of Hacac in the film, which has also been reported by Yanguas-Gil *et al.*[84]

After this initial apparent thickness increase, the GPC of $Al_2O_3$ for both substrates is very small compared to the normal GPC of approximately 1 Å/cycle. On $SiO_2$, no significant

increase in apparent thickness is shown. This indicates that the adsorbed Hacac molecules on the $Al_2O_3$ deposited in the first cycles, are able to block TMA adsorption and inhibit further deposition. This does not agree with the results obtained by Yanguas-Gil *et al.*, who showed that the GPC for ABC-type ALD of $Al_2O_3$ using Hacac as the inhibitor reduced to 0.4 Å/cycle. However, some differences in operating parameters (different temperature, Hacac dosing times unknown) might cause this deviation. After the initial apparent thickness increase (due to adsorption of Hacac) on $CoO_x$, the GPC decreases for an increasing number of cycles. The slope of the apparent thickness (after Hacac adsorption in the first cycle) indicates ALD of $Al_2O_3$. It seems the adsorbed Hacac on $CoO_x$ is not able to fully block TMA adsorption, resulting in growth. However, once $Al_2O_3$ is deposited on the $CoO_x$ substrate, the GPC should be equal to the GPC of the $Al_2O_3$ deposited on the $SiO_2$ substrate. This explains the slowly decreasing GPC.

To check whether $Al_2O_3$ was deposited, both the $CoO_x$ and $SiO_2$ samples after 50 ABC cycles of thermal ALD of $Al_2O_3$ using Hacac as the inhibitor were examined using XPS. On both samples, a small amount of Al was detected. This verifies that Hacac adsorbs on the deposited $Al_2O_3$, blocking further deposition. Since the adsorbed Hacac stops ALD of $Al_2O_3$ on a $Al_2O_3$ coated substrate, it is not possible to obtain area-selective ALD using this process.

Using Hacac as the inhibitor for plasma-assisted ALD of $Al_2O_3$, as shown in figure 6.3 B, shows growth on both substrates. However, the GPC is reduced significantly, to 0.31 and 0.24 Å/cycle for deposition on $CoO_x$ and $SiO_2$ respectively. The initial increase in apparent thickness on both substrates is, similarly caused as described above, by the adsorption of Hacac on $CoO_x$, and deposition of $Al_2O_3$ on $SiO_2$. However, as shown in chapter 5, the inhibitor is (partially) removed from the $CoO_x$ substrate by the $O_2$ plasma exposure. The GPCs are expected to be equal once both surfaces are coated with $Al_2O_3$. The difference in GPC can be caused by oxidation of the underlying Co substrate during $O_2$ plasma exposures. Even though the surface has been pretreated with a 5 minute $O_2$ plasma, separate experiments have shown that a 1 minute $O_2$ plasma exposure on a $CoO_x$ substrate increases the apparent thickness by $\sim$ 3 Å.

Interestingly, the thermal process shows that adsorbed Hacac is able to fully block TMA adsorption whereas the growth during plasma-assisted ALD indicates adsorption of TMA after Hacac adsorption. One possible explanation for this is a more densily-packed inhibiting layer is obtained after several combinations of Hacac and $H_2O$ on the surface. In previous research, it has been shown that alternating between Hacac and methanol increased Hacac coverage on the surface.[58] In the case of Hacac and $H_2O$, the $H_2O$ dose could remove some of the weakly bonded acac from the surface, allowing for new Hacac adsorption. This could increase the stability of the inhibitor layer, which could improve the precursor blocking. Another possible explanation for this difference in blocking ability is the formation of acac fragments (as shown in section 3.3) when exposing the inhibitor layer to an $O_2$ plasma. As shown in chapter 4, fragmentation of acac ligands on the surface affects the blocking ability of the inhibitor.

In conclusion, the adsorbed acac on $CoO_x$ is not able to fully block TMA adsorption, which results in ALD on both the growth and the non-growth area. Therefore, processes using Hacac as the inhibitor are not applicable for area-selective ALD of $Al_2O_3$ in the presence of $CoO_x$.

## 6.3 Delaying nucleation of $Al_3O_3$ ALD by on Co by using VPA as the inhibitor

Vinylphosphonic acid was investigated as an inhibitor for area-selective ALD of $Al_2O_3$. Ideally, the inhibitor adsorbs selectively on the non-growth area (Co), while not adsorbing on both the growth area ($SiO_2$) and the material that is being deposited ($Al_2O_3$). Therefore, adsorption of VPA was investigated on reduced Co (Co prepared using a 5 minute $H_2$ plasma pretreatment), $SiO_2$ and $Al_2O_3$. The (increase of) apparent thickness as a function of 10 subsequent 5 second doses of VPA is plotted in figure 6.4.

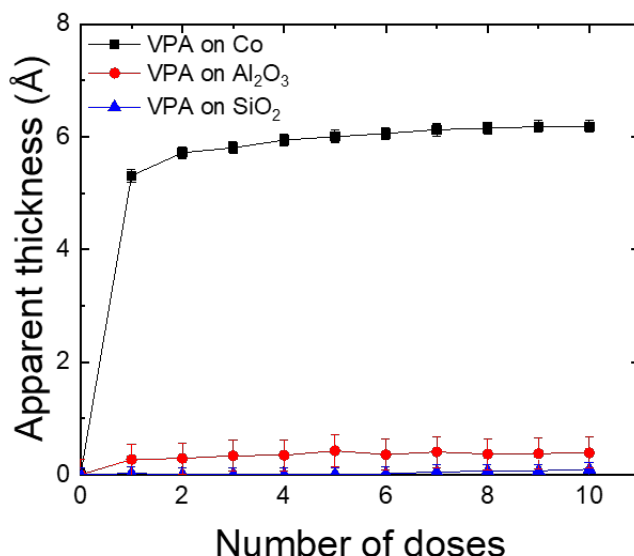


**Figure 6.4:** *In situ* ellipsometry measurements for adsorption of vinylphosphonic acid on various substrates. 10 subsequent exposures of 5 seconds were dosed to check adsorption and saturation.

On reduced Co, dosing VPA results in an apparent thickness increase, showing VPA adsorption on the surface. After approximately three subsequent doses, the apparent thickness does not significantly increase, indicating VPA adsorption has saturated on the surface. On $SiO_2$, ellipsometry shows no significant adsorption of VPA, as expected from the SAM literature.[25] However, on $Al_2O_3$ a small amount of VPA adsorption is observed. VPA adsorption on $Al_2O_3$ could reduce the GPC of the area-selective ALD process, resulting in less material being selectively deposited in the nucleation delay. However, the main requirement is that the VPA inhibitor adsorbed on Co is able to block precursor adsorption.

As stated before, ALD of $Al_2O_3$ can be achieved using either thermal ALD or plasma-assisted ALD. Alternation between the $O_2$ plasma and VPA will most likely result in deposition of a phosphorus oxide layer on the sample.[87] Therefore, only thermal ALD of $Al_2O_3$ has been investigated while using VPA as the inhibitor. This inhibitor is assumed not to be removed in these cycles using $H_2O$, because VPA has been shown to make the substrate hydrophobic.[25] Therefore, a single VPA treatment prior to the ALD process on the reduced cobalt substrate

has been investigated first, similar to area-selective ALD using SAMs. The nucleation curves measured using *in situ* SE are given in figure 6.5.

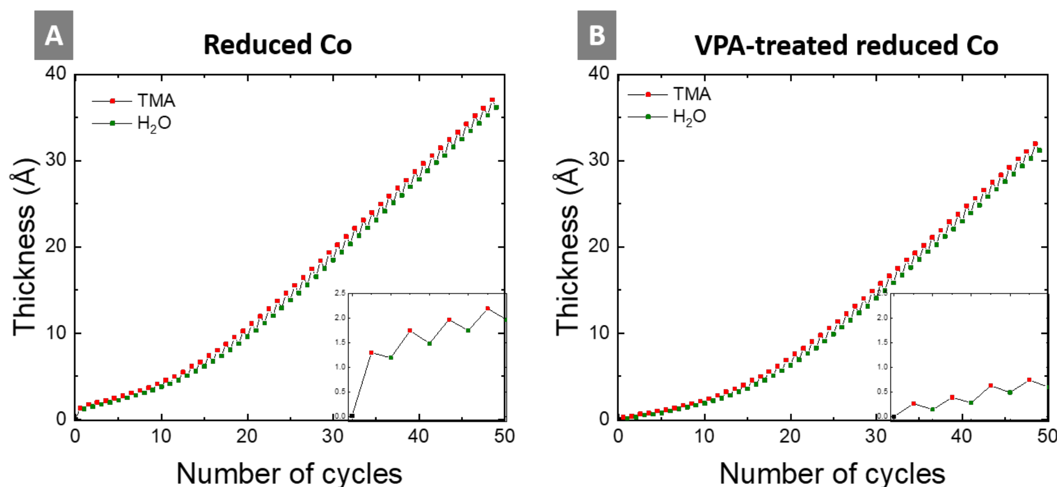


**Figure 6.5:** *In situ* ellipsometry measurements (after every dosing step) for BC cycles of thermal ALD of $Al_2O_3$ on (A) reduced cobalt, and (B) reduced cobalt after dosing vinylphosphonic acid. The insets show the thickness increases after each dosing step for the first four cycles.

Figure 6.5A shows the nucleation curve for thermal ALD of $Al_2O_3$ on reduced cobalt without the VPA pretreatment. A short nucleation delay is observed, which is not uncommon in ALD. The reduced cobalt should not contain -OH groups on the surface that allow for immediate ALD nucleation, resulting in an small initial nucleation delay.

Figure 6.5B shows the nucleation curve for thermal ALD of $Al_2O_3$ on reduced cobalt after dosing VPA. As compared to figure 6.5 A, the nucleation delay is slightly longer. The insets in both graphs highlight the SE measurements after every dose during the first cycles. In the first few cycles, less TMA adsorption is visible on the VPA-treated Co (thickness increase of 0.3 Å) as compared to the reduced Co (thickness increase of 0.5 Å). This causes a reduced GPC in the first few cycles. However, already some TMA adsorption is observed during the first few cycles, indicating that the precursor adsorption is not sufficiently blocked.

Although VPA slightly increased the nucleation delay, dosing of the inhibitor solely prior to thermal ALD does not grant sufficient blocking of ALD on Co to achieve area-selective ALD. Therefore, VPA doses were included in the ALD cycles before the precursor dose, resulting in ABC-type cycles. The nucleation curved for this process are depicted in figure 6.6, showing the thickness measured by ellipsometry after every ABC-type cycle on Co.

In the first cycle, the thickness measured by ellipsometry increased by $\sim$ 12 Å. From the results in figure 6.4 it is known that VPA on Co results in an apparent thickness increase of $\sim$ 6 Å. In chapter 5 it is shown that TMA on Co also results in a big increase ($\sim$ 7 Å) of the apparent thickness. Therefore, this large increase in thickness is probably due to a combination of VPA and TMA adsorption. After this increase in thickness, linear growth is observed. The GPC of the linear growth was determined to be 0.3 Å/cycle, which is a reduction of approximately 65% as compared to thermal ALD of $Al_2O_3$ without using VPA.

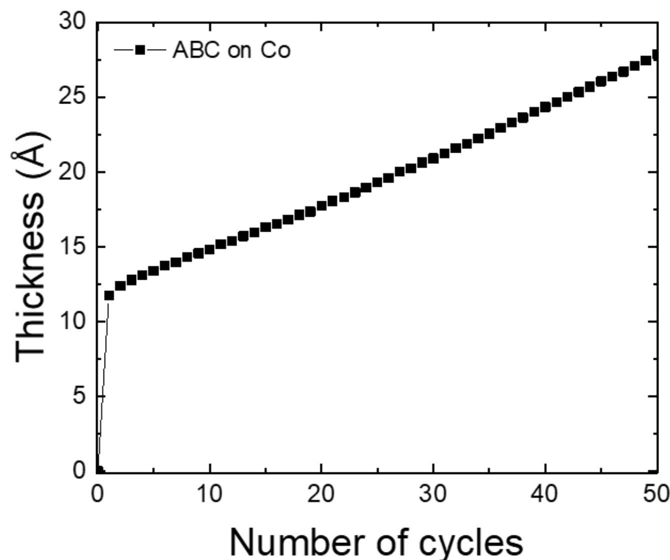


**Figure 6.6:** *In situ* ellipsometry measurement of the nucleation curve using VPA as the inhibitor in ABC-type ALD cycles for thermal ALD of $Al_2O_3$ on reduced Co.

From this data it can be concluded that VPA as an inhibitor on reduced cobalt is not able to fully block TMA adsorption. Therefore, this ABC-type ALD process is not suitable for area-selective ALD of $Al_2O_3$. Furthermore, the small amount of VPA adsorption on $Al_2O_3$, as shown in figure 6.4, reduces the GPC of thermal ALD of $Al_2O_3$ significantly.

## 6.4 Conclusion and outlook

Both Hacac and VPA were tested as an inhibitors for area-selective ALD of $Al_2O_3$. Using Hacac, thermal ALD of $Al_2O_3$ is blocked, independent of the substrate. For the plasma-assisted ALD process, using Hacac as the inhibitor resulted in a reduced GPC. VPA is shown to adsorb on Co and $Al_2O_3$ and not on $SiO_2$, similar to Hacac. Completely blocking ALD nucleation on Co is necessary to achieve area-selective ALD. It is shown that VPA adsorbed on Co partially blocks precursor adsorption, which is not sufficient to achieve area-selective ALD. Although both processes tested are not directly suitable for area-selective ALD of $Al_2O_3$, this research gives a starting point for future research. In order to achieve area-selective ALD of $Al_2O_3$, different ALD recipes are needed. Possible improvements for future research are suggested in this section.

The precursor used in this research for ALD of $Al_2O_3$, TMA, is small, volatile and highly reactive.[88] Physically blocking precursor adsorption of such a small and reactive molecule is challenging, since small defects in the inhibitor layer allow for adsorption of precursor. Therefore, a larger precursor molecule for ALD of $Al_2O_3$ (e.g. dimethylaluminum isopropoxide or triisobutylaluminum) is suggested for area-selective ALD. Using Hacac as the inhibitor, the reduced GPC will limit the thickness that can be selectively deposited in the nucleation

delay, which is not optimal. However, area-selective ALD is possible if the adsorbed Hacac on the Co is able to completely block precursor adsorption.

Furthermore, an alternative inhibitor can be examined. For instance, the tail length of the VPA inhibitor could be increased which can improve precursor blocking. In SAM literature, Chen *et al.* showed that an alkane chain length larger than 12 units is required to block $HfO_2$ ALD completely.[89] An example of a possible alternative inhibitor is butylphosphonic acid (as shown in figure 6.7). By keeping the phosphonic acid headgroup, the adsorption of the inhibitor should remain similar. The choice of tail length seems to be a trade-off between volatility and the ability to block precursor adsorption.[90,91]

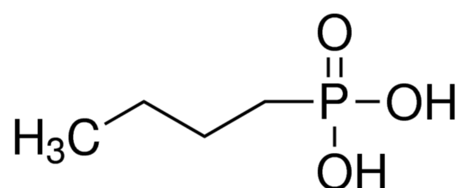


**Figure 6.7:** Stuctural formula of butylphosphonic acid, consisting of a phosphonic acid headgroup and a butyl 'tail'.[91]

The choice of inhibitor is not limited to phosphonic acids. Sampson *et al.* showed selective inhibition of TMA adsorption using SAMs with a thiol headgroup.[92] The SAM was dosed in vapour phase, which reduces the SAM formation time to approximately 30 minutes. A nucleation delay of 20 cycles was shown for thermal ALD of $Al_2O_3$, using 1-dodecanethiol (DDT) as a SAM monomer. This process can be used as a starting point for area-selective ALD of $Al_2O_3$ using ABC-type cycles using a thiol inhibitor.

# Chapter 7

# Conclusion and outlook

## 7.1 Conclusion

This work was focused on the development of area-selective ALD processes for $SiO_2$ and $Al_2O_3$. These processes can for example be employed for selective deposition of dielectric barriers for self-aligned VIAs. Three research questions were investigated:

1. *Can we improve the selectivity of area-selective ALD of $SiO_2$ using ABC-type cycles with Hacac as the inhibitor on $SiO_2$ with $Al_2O_3$ as the non-growth area?*

The selectivity of area-selective ALD of $SiO_2$ is improved. Ellipsometry and FTIR measurements showed inhibitor fragments on the surface, which affect new Hacac adsorption and limit selectivity. Implementing a $H_2$ plasma exposure between the precursor and co-reactant dose fully removed the adsorbed Hacac from the surface. The nucleation delay was increased to approximately 30 cycles, which corresponds in $\sim$ 3 nm of selective deposition.

2. *Can we achieve area-selective ALD of $SiO_2$ with Co as the non-growth area?*

Delaying nucleation of $SiO_2$ ALD on Co was studied on both oxidized and reduced Co. On oxidized Co, a nucleation delay of approximately 20 cycles is shown using ellipsometry, which results in a selectivity window of $\sim$ 2 nm. On reduced Co, a nucleation delay of 25 cycles is shown using XPS, resulting in a selectivity window of $\sim$ 2.5 nm. However, SEM images indicated dewetting of the Co substrate from the underlying Si. Therefore, the actual nucleation delay for ALD of $SiO_2$ could be more than 25 cycles. However, to further improve the selectivity of this process, the dewetting of the Co substrate should be mitigated.

3. *Can we design a process for area-selective ALD of $Al_2O_3$ with Co as the non-growth area?*

Two different inhibitors (Hacac and VPA) were examined for area-selective ALD of $Al_2O_3$. Both inhibitors are shown to not fully block adsorption of the precursor on Co, which indicates that these processes are not viable for area-selective deposition. However, some relevant information is presented as a starting point for future research.

Overall, area-selective ALD using ABDC-type cycles shows promising results for its application in self-aligned VIAs. By decoupling the inhibitor removal and the precursor ligand removal in two separate steps, significant improvements are made in terms of selectivity.

However, some challenges still need to be overcome before it can be implemented in industrial applications. Future work should focus on mitigating damages done to the Co surface. Moreover, testing the investigated processes on patterned substrates would be a next step in the implementation of this area-selective ALD process. Although throughout this work the application of self-aligned VIAs was used to define the requirements, the knowledge gained in this research is more widely applicable in the field of ALD.

## 7.2 Outlook

The experiments conducted in this work have resulted in some new insight concerning area-selective ALD using inhibitors in multi-step cycles. However, some results raised questions and induced ideas for future experiments. In this section, future research is proposed and some interesting improvements for the area-selective ALD process are given.

### 7.2.1 Reduction of oxidized cobalt

Studying the nucleation delay for area-selective ALD of $SiO_2$ on cobalt substrates using ellipsometry turned out to be challenging. Since the cobalt substrate is subjected to oxidation and reduction by $O_2$ and $H_2$ plasma exposures, the optical response of the substrate changes. Ideally, the $H_2$ plasma exposure would be able to fully reduce the oxidized cobalt. In that case, the substrate could be exposed to a $H_2$ plasma post deposition, resulting in a conducting Co substrate. However, the changes in the optical response with ellipsometry indicate this is not the case. Therefore, further investigation into the reduction of oxidized cobalt would complement the results from chapter 5 well.

When examining area-selective ALD on reduced Co, it was assumed in this research that a 5 minute $H_2$ plasma exposure (600 W, 300 mTorr) was able to fully reduce the native oxide from the Co substrate. Ellipsometry was used to investigate the saturation of this reducing process, showing that the changes in optical response mostly appear in the first 5 minutes of the $H_2$ plasma exposure. However, this does not prove that the substrate is fully reduced. It is possible that for instance only the top layer is reduced, resulting in a combination of oxidized and metallic layers in the substrate. In literature, it was shown that a $H_2$ plasma is able to fully reduce $Co_3O_4$ nanoparticles to metallic Co.[93] Also, a low temperature $H_2$ plasma was used by Sabat *et al.* to successfully reduce a $Co_3O_4$ pellet (2 cm thickness.)[78] This shows that it should be possible to fully reduce oxidized Co, including native oxide and oxidation formed during $O_2$ plasma exposures.

To investigate the reduction of the Co substrate, XPS can be used to both measure the O content in the film, as well as look at the oxidation state of the Co. However, after exposing the Co substrate to a reducing $H_2$ plasma exposure, the substrate will be oxidized again due to air exposure when transferring the sample to the XPS reactor. To protect the substrate from oxidation, *in situ* deposition of a capping layer is proposed after reducing the substrate. The proposed capping layer should (1) not contain any oxygen, which could migrate into the Co substrate, (2) be able to fully protect the substrate from oxidation due to air exposure and (3) be able to be etched away using the ion beam in the XPS setup.

A metal-nitride layer could be used as a capping layer. In IC fabrication, metal-nitride layers are used as liner material, separating the dielectric (O-containing) material with the metal lines. After transferring the capped sample to the XPS reactor, the capping layer can be etched using an ion beam. A depth profile of the substrate can be used to investigate whether there is O in the film, which demonstrates whether or not the Co substrate is fully reduced using the $H_2$ plasma exposures. Additionally, different plasma pretreatments can be examined to verify their effects on the Co substrate.

### 7.2.2 Eliminate dewetting of Co substrates for ABDC-type ALD cycles

It was shown in chapter 5 that the Co substrates dewet when exposed to more than 25 ABDC-type ALD cycles. Since XPS showed there is no deposition at all up to 25 cycles, it is believed that a longer nucleation delay can be achieved. To improve the area-selective ALD process using Co as the non-growth area, the dewetting of the Co substrates should be eliminated. In order to check if the dewetting was solely due to the combination of plasmas, 50 repeated exposures of $H_2$ and $O_2$ plasmas (DC cycles) were dosed on a Co sample. A SEM image of the Co sample after 50 DC cycles is shown in figure 7.1.

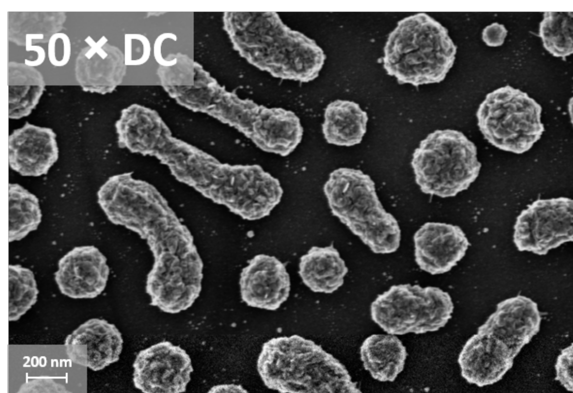


**Figure 7.1:** Top-view SEM image for 50 DC cycles. The influence of the combination of plasmas on the Co substrate is investigated.

Figure 7.1 shows that a combination of the plasmas results in dewetting of the film. In fact, compared to the image from figure 5.8, there is a lower coverage of Co after 50 DC cycles, than there is for 50 ABDC cycles. This suggests that the adsorbed Hacac on the surface somehow limits the dewetting of the Co. Dosing of only $H_2$ or $O_2$ plasmas separately (used as a 5 min pretreatment before depositions) does not result in dewetting. Therefore, it is believed that the repeated oxidation and reduction of the Co causes stresses in the film that eventually lead to dewetting.

A further study into elimination of the dewetting of the Co for a combination of plasmas would be very relevant. Since oxidation of the Co should be limited for the application of VIA fabrication, the $O_2$ plasma exposure can be minimized. Decreasing the $O_2$ plasma exposure can be done by (a combination of) lowering the plasma power, decreasing the $O_2$ plasma exposure time and increasing the pressure during $O_2$ plasma exposure. After finding plasma settings that eliminate dewetting, it should be verified that the plasma exposure is still

sufficient to deposit $SiO_2$ on the growth area. However, since the $H_2$ plasma might (partially) remove the precursor ligands, it is possible that only a very short $O_2$ plasma exposure is able to deposit $SiO_2$. Recently, follow-up on this work confirmed that reducing the $O_2$ plasma exposure limits the dewetting of the Co. This shows room for improvement for area-selective ALD using ABDC cycles with Co as the non-growth area.

By reducing the $O_2$ plasma exposure, it might even be possible to investigate future ABDC cycle experiments using ellipsometry. If the changes in the Co substrate are mitigated, the optical response may not be affected by repeated oxidation and reduction, which makes accurate ellipsometry modelling possible.

### 7.2.3 Combining ALD and ALE to reset the nucleation delay

As stated before, one of the main challenges in area-selective ALD is increasing the nucleation delay in order to achieve as much selective deposition as possible. For the application of self-aligned VIAs, selective deposition of approximately 10 nm is needed in order to have a sufficiently high dielectric barrier. In this research, loss of selectivity occurred after (at most) $\sim$ 2.5 nm. Therefore, combining area-selective ALD with an etch process is suggested to increase the thickness that can be deposited in a selective manner.

An $SiO_2$ ALE (atomic layer etch) process could be used (in a supercycle with area-selective ALD) to reset the non-growth area after deposition of nucleation sites. This type of approach has been suggested in literature by Vallat *et al.*,[94] and is depicted in figure 7.2. To illustrate the proposed supercycle, a schematic image of this method shows the increase in thickness as a function of number of cycles for both the growth area (orange) and non-growth area (blue). During the initial area-selective ALD process, a linear increase in thickness shows immediate nucleation on the growth area, whereas a nucleation delay occurs on the non-growth area. After a certain number of cycles, a loss of selectivity causes nucleation to start on the non-growth area. By introducing an etch step, material is removed from both the growth and non-growth area. If the etch step is able to fully remove the deposited material on the non-growth area, this surface is brought back to the original state, where the delay of ALD nucleation can be exploited again. By repeating this combination of area-selective ALD with a etch step in supercycles, increasing the thickness that can be deposited in an area-selective manner. However, the etch step should selectively etch the deposited material ($SiO_2$) without affecting the non-growth substrate (Co).

In literature, some possible etch steps for $SiO_2$ have been reported. A dry etching method using HF vapor can be used to etch $SiO_2$.[95] Although this is expected to selectively etch $SiO_2$ without affecting the Co substrate, atomic level controll of thickness is not obtained. Furthermore, fluorcarbon-assisted ALE of $SiO_2$ was studied by Metzler *et al.*, using low energy Ar ion bombardment to remove the fluorcarbon reactants formed on the surface.[96] Combining these etch steps with area-selective ALD could result in an increased selectivity. However, the impact of these processes on the non-growth area should also be considered. For the application of self-aligned VIAs, fluor-carbon contaminants on the Co might be problematic. Although the HF vapor etch compromises on the atomic level of control, this is not expected to affect the Co substrate.

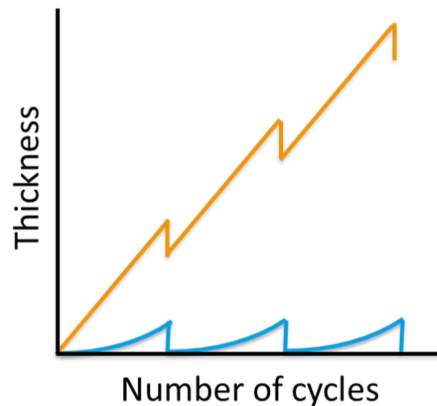


**Figure 7.2:** Schematic plot of the thickness as a function of the number of cycles, for the proposed supercycle ALD scheme. An etch step is implemented after nucleation on the non-growth area in order to remove the unwanted material, and exploit the new nucleation delay.

### 7.2.4 Alternating complementary area-selective ALD schemes

For area-selecitve ALD, improving the selectivity of the deposition process is important in order to reach thicker features deposited in a selective manner. However, when relatively thick area-selective ALD film growth can be achieved, the lateral ALD growth is not blocked by the inhbitor molecules. This results in mushroom-like growth, which is illustrated in figure 7.3. Even for SAMs, after a few cycles the selectively deposited feature grows higher than the thickness of the blocking layer, resulting in widening of the deposited features.[97] With feature sizes in IC fabrication shrinking and placement requirements becoming increasingly strict, even a small lateral broadening might already have a detrimental influence on device performance.

**Figure 7.3:** Illustration of lateral growth during area-selective ALD, resulting in a mushroom-like structure.[97]

A possible strategy to solve the lateral broadening is using two alternating complementary area-selective ALD processes. By combining two processes with a reverse selectivity, meaning one deposits in a selective manner one material on area A and the other deposits another material in a selective manner on area B, the lateral broadening can be confined within area-selectively deposited material. A schematic of this proposed process is depicted in figure 7.4. By combining two different ALD processes in supercycles, the amount of lateral broadening can be controlled.

An additional advantage of combining two complementary area-selective ALD processes, is the encapsulation of any island nucleation. After area-selective ALD of one material on area A, nucleation sites might be present on the non-growth area for this process, area B. If

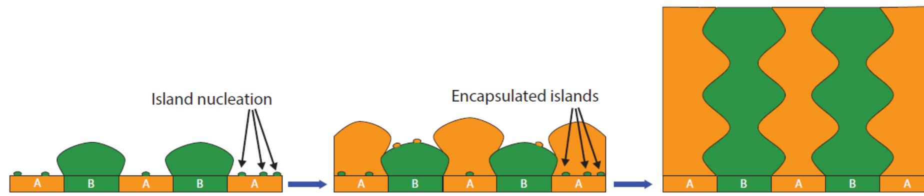


**Figure 7.4:** Schematic illustration of two complimentary area-selective ALD cycles. The lateral broadening is limited by alternating two area-selective ALD processes, with contrary growth areas. Furthermore, encapsulation of nucleation islands is shown.[58]

the subsequent process selectively deposits another material on area B, the small nucleation sited are encapsulated, 'resetting' the nucleation on the non-growth area for the first process. However, this introduces cross-contamination between the two materials, which might not be acceptable for some applications. By defining the number of ALD cycles for two complementary ALD processes in the supercycle, both lateral broadening and amount of contaminants can be controlled.

# Acknowledgements

This work would not have been possible without guidance and assistance of several people, both on a scientific and personal level. Therefore, I would like to express my appreciation to everyone who contributed to this MSc. thesis.

First and foremost, I would like to thank my supervisors Marc Merkx and Adrie Mackus for their guidance throughout this research project. Both of your dedication to research always got me enthusiastic to do mine to the best of my abilities. Marc, thank you for getting me started on the setups, and all the feedback throughout the year. Adrie, thank you for giving me the opportunity to work on this project, and always being ready to discuss my findings and the conclusions following. The research I have conducted (and especially this thesis) have benefited immensely from the guidance you gave me.

Secondly, I am profoundly grateful for everyone in the PMP research group. I have enjoyed working with everyone, learning a lot from various interesting research topics. Especially thanks to Erwin Kessels for suggesting this project to me, the technicians (Janneke, Cristian, Joris, Caspar and Jeroen) for maintaining and troubleshooting the setups whenever needed and the secretaries (Jeanne and Lianne) for all the administrative help.

Lastly, I would like to thank my friends and family for encouraging me and providing me with (sometimes much needed) relaxation during the last year. In particular, I would like to thank Jackie, my mom, dad and sister, for always cheering me up and supporting me throughout this project. Furthermore, my roommates, fraternity and fellow graduates for always relieving my workload with a coffee break, or other recreational diversion.

# Bibliography


[1] Jan Mulkens, Michael Hanna, Hannah Wei, Vidya Vaenkatesan, Henry Megens, and Daan Slotboom. Overlay and edge placement control strategies for the 7nm node using EUV and ArF lithography. In *SPIE*, 2015.

[2] A. J. M. Mackus, A. A. Bol, and W. M. M. Kessels. The use of atomic layer deposition in advanced nanopatterning. *Nanoscale*, 6(19):10941–10960, 2014.

[3] D. James. Intel's 14-nm Parts are Finally Here! *https://www.chipworks.com/about-chipworks/overview/blog/intel's-14-nm-parts-are-finally-here*, 2014. Accessed: 2018-06-08.

[4] Chris G.N. Lee, Keren J. Kanarik, and Richard A. Gottscho. The grand challenges of plasma etching: A manufacturing perspective. *Journal of Physics D: Applied Physics*, 47(27), 2014.

[5] Joern-Holger Franke, Matt Gallagher, Gayle Murdoch, Sandip Halder, Aurelie Juncker, and William Clark. EPE analysis of sub-N10 BEoL flow with and without fully self-aligned via using Coventor SEMulator3D. 1014529(1014529), 2017.

[6] Jeongdong Choe. Intel 3D XPoint Memory Die Removed from Intel Optane PCM (Phase Change Memory). *http://www.techinsights.com/about-techinsights/overview/blog/intel-3D-xpoint-memory-die-removed-from-intel-optane-pcm/*, 2017. Accessed: 2018-09-18.

[7] Steven George. Atomic Layer Deposition: An Overview. *Chem. Rev.*, 110:111–131, 2010.

[8] E Langereis, S B S Heil, H C M Knoops, W Keuning, M C M van de Sanden, and W M M Kessels. In situ spectroscopic ellipsometry as a versatile tool for studying atomic layer deposition. *Journal of Physics D: Applied Physics*, 42(7):073001, 2009.

[9] Riikka L Puurunen. Surface chemistry of atomic layer deposition: A case study for the trimethylaluminum/water process. *Journal of Applied Physics*, 97(121301), 2005.

[10] H C M Knoops, S E Potts, A A Bol, and W M M Kessels. *Atomic layer deposition.* 2 edition, 2015.

[11] H. B. Profijt, S. E. Potts, M. C. M. van de Sanden, and W. M. M. Kessels. Plasma-Assisted Atomic Layer Deposition: Basics, Opportunities, and Challenges. *Journal of Vacuum Science & Technology A: Vacuum, Surfaces, and Films*, 29(5):050801, 2011.

[12] G Dingemans, C A A van Helvoirt, M C M van de Sanden, and W M M Kessels. Plasma-assisted atomic layer deposition of low temperature SiO2. *ECS Transactions*, 35(4):191–204, 2011.

[13] J. W. Klaus, A. W. Ott, J. M. Johnson, and S. M. George. Atomic layer controlled growth of SiO2 films using binary reaction sequence chemistry. *Applied Physics Letters*, 1997.

[14] S. B. S. Heil, F. Roozeboom, M. C. M. van de Sanden, and W. M. M. Kessels. Plasma-assisted atomic layer deposition of $Ta_2O_5$ from alkylamide precursor and remote O2 plasma. *Journal of Vacuum Science & Technology A: Vacuum, Surfaces, and Films*, 2008.

[15] Rong Chen, Hyoungsub Kim, Paul C. McIntyre, David W. Porter, and Stacey F. Bent. Achieving area-selective atomic layer deposition on patterned substrates by selective surface modification. *Applied Physics Letters*, 86(19):1–3, 2005.

[16] Martin M. Frank, Yves J. Chabal, Martin L. Green, Annelies Delabie, Bert Brijs, Glen D. Wilk, Mun Yee Ho, Elisa B.O. Da Rosa, Israel J.R. Baumvol, and Fernanda C. Stedlle. Enhanced initial growth of atomic-layer-deposited metal oxides on hydrogen-terminated silicon. *Applied Physics Letters*, 83(4):740–742, 2003.

[17] Riikka L. Puurunen, Wilfried Vandervorst, Wim F.A. Besling, Olivier Richard, Hugo Bender, Thierry Conard, Chao Zhao, Annelies Delabie, Matty Caymax, Stefan De Gendt, Marc Heyns, Minna M. Viitanen, Marco De Ridder, Hidde H. Brongersma, Yde Tamminga, Thuy Dao, Toon De Win, Marcel Verheijen, Monja Kaiser, and Marko Tuominen. Island growth in the atomic layer deposition of zirconium oxide and aluminum oxide on hydrogen-terminated silicon: Growth mode modeling and transmission electron microscopy. *Journal of Applied Physics*, 96(9):4878–4889, 2004.

[18] Qian Tao, Gregory Jursich, and Christos Takoudis. Selective atomic layer deposition of $HfO_2$ on copper patterned silicon substrates. *Applied Physics Letters*, 96(19):192105, 2010.

[19] Wayne L. Gladfelter. Selective Metallization by Chemical Vapor Deposition. *Chemistry of Materials*, 5(10):1372–1388, 1993.

[20] Alfredo Mameli. *Selective atomic layer deposition and etching of oxides.* PhD thesis, Eindhoven University of Technology, 2018.

[21] Paul C. Lemaire, Mariah King, and Gregory N. Parsons. Understanding inherent substrate selectivity during atomic layer deposition: Effect of surface preparation, hydroxyl density, and metal oxide composition on nucleation mechanisms during tungsten ALD. *Journal of Chemical Physics*, 146(5), 2017.

[22] Ali Haider, Petro Deminskyi, Talha M. Khan, Hamit Eren, and Necmi Biyikli. Area-Selective Atomic Layer Deposition Using an Inductively Coupled Plasma Polymerized Fluorocarbon Layer: A Case Study for Metal Oxides. *The Journal of Physical Chemistry C*, 120(46):26393–26401, 2016.

[23] Xirong Jiang and Stacey Bent. Area-Selective ALD with Soft Lithographic Methods: Using Self-Assembled Monolayers to Direct Film Deposition. *J. Phys. Chem. C*, 113:17613–17625, 2009.

[24] Sidharam P. Pujari, Luc Scheres, Antonius T.M. Marcelis, and Han Zuilhof. Covalent surface modification of oxide surfaces, 2014.

[25] Fatemeh Sadat Minaye Hashemi, Chaiya Prasittichai, and Stacey F. Bent. A new resist for area selective atomic and molecular layer deposition on metal-dielectric patterns. *Journal of Physical Chemistry C*, 2014.

[26] Xirong Jiang, Rong Chen, and Stacey F. Bent. Spatial control over atomic layer deposition using microcontact-printed resists. *Surface and Coatings Technology*, 201(22-23 SPEC. ISS.):8799–8807, 2007.

[27] Rong Chen, Hyoungsub Kim, Paul C. McIntyre, and Stacey F. Bent. Self-assembled monolayer resist for atomic layer deposition of $HfO_2$ and $ZrO_2$ high-$\kappa$ gate dielectrics. *Applied Physics Letters*, 84(20):4017–4019, 2004.

[28] H. B. R. Lee, J. Kim, H. Kim, W. H. Kim, J. W. Lee, and I Hwang. Degradation of the deposition blocking layer during area-selective plasma-enhanced atomic layer deposition of Cobalt. *Journal of the Korean Physical Society*, 56(1):104–107, 2010.

[29] Alfredo Mameli, Marc J M Merkx, Bora Karasulu, Fred Roozeboom, Wilhelmus (Erwin) M M Kessels, and Adriaan J M Mackus. Area-Selective Atomic Layer Deposition of SiO2 Using Acetylacetone as a Chemoselective Inhibitor in an ABC-Type Cycle. *ACS Nano*, 2017.

[30] Angus I. Kingon, Jon Paul Maria, and S. K. Streiffer. Alternative dielectrics to silicon dioxide for memory and logic devices. *Nature*, 406(6799):1032–1038, 2000.

[31] Yoshiaki Fukuzumi, Ryota Katsumata, Masaru Kito, Masaru Kido, Mitsuru Sato, Hiroyasu Tanaka, Yuzo Nagata, Yasuyuki Matsuoka, Yoshihisa Iwata, Hideaki Aochi, and Akihiro Nitayama. Optimal integration and characteristics of vertical array devices for ultra-high density, bit-cost scalable flash memory. *Technical Digest - International Electron Devices Meeting, IEDM*, (c):449–452, 2007.

[32] Jiyoung Kim, Augustin J. Hong, Masaaki Ogawa, Ma Siguang, Emil B. Song, You Sheng Lin, Jeonghee Han, U. In Chung, and Kang L. Wang. Novel 3-D structure for ultra high density flash memory with VRAT (Vertical-Recess-Array-Transistor) and PIPE (Planarized Integration on the same PlanE). *Digest of Technical Papers - Symposium on VLSI Technology*, pages 122–123, 2008.

[33] Cepheiden. Cmos-chip structure in 2000s. *https://commons.wikimedia.org/wiki/File:Cmos-chip_structure_in_2000s_%28en%29.svg*, 2006. Accessed: 2018-07-20.

[34] M. J. Biercuk, D. J. Monsma, C. M. Marcus, J. S. Backer, and R. G. Gordon. Low-temperature atomic-layer-deposition lift-off method for microelectronic and nanoelectronic applications. *Applied Physics Letters*, 83(12):2405–2407, 2003.

[35] Benjamin D Briggs, C B Peethala, D L Rath, J Lee, S Nguyen, N V Licausi, P S Mclaughlin, H You, and D Sil. Fully Aligned Via Integration for Extendibility of Interconnects to Beyond the 7 nm Node. *IEDM Technical Digest. IEEE International Electron Devices Meeting*, 17(c):338–341, 2017.

[36] Gayle Murdoch, Jürgen Bömmels, Christopher J. Wilson, Khashayar Babaei Gavan, Quoc Toan Le, Zsolt Tokei, and William Clark. Feasibility study of fully self aligned vias for 5nm node BEOL. *IITC 2017 - 2017 IEEE International Interconnect Technology Conference*, pages 1–4, 2017.

[37] S. B. S. Heil, J. L. van Hemmen, C. J. Hodson, N. Singh, J. H. Klootwijk, F. Roozeboom, M. C. M. van de Sanden, and W. M. M. Kessels. Deposition of TiN and $HfO_2$ in a

commercial 200mm remote plasma atomic layer deposition reactor. *Journal of Vacuum Science & Technology A: Vacuum, Surfaces, and Films*, 25(5):1357, 2007.

[38] D. R. Lide. Hardness of Minerals and Ceramics. *CRC Handb. Chem. Phys.*, pages 2313–2314, 2005.

[39] Sigma-Aldrich. Acetylacetone. *https://www.sigmaaldrich.com/catalog/product/sial/05581*. Accessed: 2018-07-20.

[40] Chemspider. Vinylphosphonic acid. *http://www.chemspider.com/Chemical-Structure.147591.html*. Accessed: 2018-07-20.

[41] Evonik. AEROSIL OX 50. *https://products-re.evonik.com/lpa-productfinder/page/productsbytext/detail.html?channel=aerosil&pid=1827&lang=en*. Accessed: 2018-07-20.

[42] AlfaAesar. Alfa Aesar. *https://www.alfa.com/en/*. Accessed: 2018-07-20.

[43] Harm C.M. Knoops, K. De Peuter, and W. M.M. Kessels. Redeposition in plasma-assisted atomic layer deposition: Silicon nitride film quality ruled by the gas residence time. *Applied Physics Letters*, 107(1), 2015.

[44] J. L. van Hemmen, S. B. S. Heil, J. H. Klootwijk, F. Roozeboom, C. J. Hodson, M. C. M. van de Sanden, and W. M. M. Kessels. Plasma and Thermal ALD of Al[sub 2]O[sub 3] in a Commercial 200mm ALD Reactor. *Journal of The Electrochemical Society*, 154(7):G165, 2007.

[45] D. Barton and F. K. Urban. Ellipsometer measurements using focused and masked beams. *Thin Solid Films*, 515(3):911–916, 2006.

[46] Varun Sharma. Spectroscopic Ellipsometry for the in-Situ Investigation of Atomic Layer Depositions. 2014.

[47] R. Swanepoel. Determination of the thickness and optical constants of amorphous silicon. *J. Phps. E: Sci. Instrum.*, 16:1214, 1983.

[48] S. H. Wemple. Refractive-index behavior of amorphous semiconductors and glasses. *Physical Review B*, 7(8):3767–3777, 1973.

[49] S. Canulescu, K. Rechendorff, C. N. Borca, N. C. Jones, K. Bordo, J. Schou, L. Pleth Nielsen, S. V. Hoffmann, and R. Ambat. Band gap structure modification of amorphous anodic Al oxide film by Ti-alloying. *Applied Physics Letters*, 104(12), 2014.

[50] J. A. Wollam Co. Inc. CompleteEASE Data Analysis Manual. pages 1–207, 2011.

[51] J. W. Weber, T. A.R. Hansen, M. C.M. Van De Sanden, and R. Engeln. B-spline parametrization of the dielectric function applied to spectroscopic ellipsometry on amorphous carbon. *Journal of Applied Physics*, 106(12), 2009.

[52] Prof Gregory N Parsons. ALD Nucleation and Area Selective Deposition. In *ALD 2018 conference*, 2018.

[53] Melvin Avrami. Kinetics of phase change. II Transformation-time relations for random distribution of nuclei. *The Journal of Chemical Physics*, 8(2):212–224, 1940.

[54] Han Bo Ram Lee, Marja N. Mullings, Xirong Jiang, Bruce M. Clemens, and Stacey F. Bent. Nucleation-controlled growth of nanoparticles by atomic layer deposition. *Chemistry of Materials*, 24(21):4051–4059, 2012.

[55] L.E. Cornelissen. *In situ infrared spectroscopy for plasma-assisted ALD of SiNx films*. PhD thesis, 2015.

[56] Rob J A van Veen, Gert Jonkers, and Wim H Hesselink. Interaction of Transition-metal Acetylacetonates with y-Al,O, Surfaces. *J. Chem. SOC., Faraday Trans. I*, 85(2):389413, 1989.

[57] Michael Baltes, Pascal Van Der Voort, Bert M. Weckhuysen, R. Ramachandra Rao, Gabriela Catana, Robert A. Schoonheydt, and Etienne F. Vansant. Synthesis and characterization of alumina-supported vanadium oxide catalysts prepared by the molecular designed dispersion of $VO(acac)_2$complexes. *Physical Chemistry Chemical Physics*, 2(11):2673–2680, 2000.

[58] M J M Merkx. *Area-selective atomic layer deposition of SiO 2*. PhD thesis, Eindhoven University of Technology, 2017.

[59] Iramis. X-ray photoelectrons spectroscopy (XPS). *http://iramis.cea.fr/en/Phocea/Vie_des_labos/Ast/alltec.php?id_ast=120*, 2018. Accessed: 2018-09-18.

[60] S. Tougaard. *SURFACE ANALYSIS — X-ray Photoelectron Spectroscopy*. Number December 2013. Elsevier Inc., 2013.

[61] John F. Moulder, William F. Stickle, Peter E. Sobol, and Kenneth D. Bomben. Handbook of X-ray Photoelectron Spectroscopy. page 261, 1992.

[62] B. Cappella and G. Dietler. Force-distance curves by atomic force microscopy. *Surface Science Reports*, 1999.

[63] Dieter K Schroder. *Semiconductor material and device characterization*. John Wiley & Sons, Inc., 3rd edition, 2006.

[64] G. I. Goldstein, D. E. Newbury, P. Echlin, D. C. Joy, C. Fiori, and E. Lifshin. *Scanning electron microscopy and x-ray microanalysis*. New York: Plenum Press, 1981.

[65] S N Slabzhennikov, O B Ryabchenko, and L A Kuarton. Interpretation of the IR Spectra of Aluminum, Gallium, and Indium Tris(acetylacetonates). *Russian Journal of Coordination Chemistry*, 32(8):570–576, 2006.

[66] Barbara Stuart. Infrared Technology. *ECT*, 14(5):224–243, 2005.

[67] Kirill O. Bugaev, Anastasia A. Zelenina, and Vladimir A. Volodin. Vibrational Spectroscopy of Chemical Species in Silicon and Silicon-Rich Nitride Thin Films. *International Journal of Spectroscopy*, 2012.

[68] B. A. Morrow and I. A. Cody. Infrared spectra of the isolated hydroxyl groups on silica. *The Journal of Physical Chemistry*, 77(11):1465–1469, 1973.

[69] Alfredo Mameli, Marc J. M. Merkx, Bora Karasulu, Fred Roozeboom, Wilhelmus (Erwin) M. M. Kessels, and Adriaan J. M. Mackus. Supporting info to Area-Selective Atomic Layer

Deposition of $SiO_2$ Using Acetylacetone as a Chemoselective Inhibitor in an ABC-Type Cycle. *ACS Nano*, page acsnano.7b04701, 2017.

[70] Aimo Rautiainen, Marina Lindblad, Leif B. Backman, and Riikka L. Puurunen. Preparation of silica-supported cobalt catalysts through chemisorption of cobalt(ii) and cobalt(iii) acetylacetonate. *Physical Chemistry Chemical Physics*, 4(11):2466–2472, 2002.

[71] Joan Von Hoene, Robert G. Charles, and William M. Hickam. Thermal Decomposition of Metal Acetylacetonates: Mass Spectrometer Studies. *The Journal of Physical Chemistry*, 62(9):1098–1101, 1958.

[72] Jinhee Kwon, Mark Saly, Mathew D Halls, Ravindra K Kanjolia, and Yves J Chabal. Substrate Selectivity of (tBu-Allyl)Co$(CO)_3$ during Thermal Atomic Layer Deposition of Cobalt. *Chem. Mater.*, 24:1025–1030, 2012.

[73] Vikrant R. Rai, Vincent Vandalon, and Sumit Agarwal. Influence of surface temperature on the mechanism of atomic layer deposition of aluminum oxide using an oxygen plasma and ozone. *Langmuir*, 28(1):350–357, 2012.

[74] Nicholas R. Johnson, Huaxing Sun, Kashish Sharma, and Steven M. George. Thermal atomic layer etching of crystalline aluminum nitride using sequential, self-limiting hydrogen fluoride and Sn$(acac)_2$ reactions and enhancement by $H_2$ and Ar plasmas. *Journal of Vacuum Science & Technology A: Vacuum, Surfaces, and Films*, 34(5):050603, 2016.

[75] Y. Lee, J.W. Dumont, and S.M. George. Atomic Layer Etching Using Thermal Reactions: Atomic Layer Deposition in Reverse. *ECS Transactions*, 69(7):233–241, 2015.

[76] Timo Weckman and Kari Laasonen. First principles study of the atomic layer deposition of alumina by TMA $H_2O$-process. *Phys. Chem. Chem. Phys.*, 17(26):17322–17334, 2015.

[77] Akhalakur Rahman Ansari, Shahir Hussain, Mohd Imran, M Sh Abdel-wahab, and Ahmed Alshahrie. Synthesis , characterization and oxidation of metallic cobalt (Co) thin film into semiconducting cobalt oxide ($Co_3O_4$) thin film using microwave plasma CVD. *Mater. Res. Express*, 5:065003, 2018.

[78] K. C. Sabat, R. K. Paramguru, S. Pradhan, and B. K. Mishra. Reduction of Cobalt Oxide ($Co_3O_4$) by Low Temperature Hydrogen Plasma. *Plasma Chemistry and Plasma Processing*, 35(2):387–399, 2015.

[79] Daniela Alburquenque, Victoria Bracamonte, Marcela Del Canto, Alejandro Pereira, and Juan Escrig. Dewetting of Co thin films obtained by atomic layer deposition due to the thermal reduction process. *MRS Communications*, 7(4):848–853, 2017.

[80] Booyong S. Lim, Antti Rahtu, and Roy G. Gordon. Atomic layer deposition of transition metals. *Nature Materials*, 2(11):749–754, 2003.

[81] Carl V. Thompson. Solid-State Dewetting of Thin Films. *Annual Review of Materials Research*, 42(1):399–434, 2012.

[82] C. Favazza, J. Trice, A. K. Gangopadhyay, H. Garcia, R. Sureshkumar, and Ramki Kalyanaraman. Nanoparticle ordering by dewetting of Co on $SiO_2$. *Journal of Electronic Materials*, 35(8):1618–1620, 2006.

[83] Yong Jun Oh, Caroline A. Ross, Yeon Sik Jung, Yang Wang, and Carl V. Thompson. Cobalt nanoparticle arrays made by templated solid-state dewetting. *Small*, 5(7):860–865, 2009.

[84] Angel Yanguas-Gil, Joseph A. Libera, and Jeffrey W. Elam. Modulation of the growth per cycle in atomic layer deposition using reversible surface functionalization. *Chemistry of Materials*, 25(24):4849–4860, 2013.

[85] Seunggi Seo, Il-Kwon Oh, Byung Chul Yeo, Sang Soo Han, Chang Mo Yoon, Joon Young Yang, Jonggeun Yoon, Choongkeun Yoo, Ho-jin Kim, Yong-baek Lee, Su Jeong Lee, Jae-Min Myoung, Han-Bo-Ram Lee, Woo-Hee Kim, and Hyungjun Kim. Reaction Mechanism of Area-Selective Atomic Layer Deposition for $Al_2O_3$ Nanopatterns. *ACS Applied Materials & Interfaces*, page acsami.7b13365, 2017.

[86] Fatemeh Sadat Minaye Hashemi, Chaiya Prasittichai, and Stacey F. Bent. Self-Correcting Process for High Quality Patterning by Atomic Layer Deposition. *ACS Nano*, 9(9):8710–8717, 2015.

[87] Matti Putkonen, Timo Sajavaara, Paavo Rahkila, Leiting Xu, Sulin Cheng, Lauri Niinistö, and Harry J. Whitlow. Atomic layer deposition and characterization of biocompatible hydroxyapatite thin films. *Thin Solid Films*, 517(20):5819–5824, 2009.

[88] M. E. Bartram, T. A. Michalske, and J. W. Rogers. A reexamination of the chemisorption of trimethylaluminum on silica. *Journal of Physical Chemistry*, 95(11):4453–4463, 1991.

[89] Rong Chen, Hyoungsub Kim, Paul C. McIntyre, and Stacey F. Bent. Investigation of self-assembled monolayer resists for hafnium dioxide atomic layer deposition. *Chemistry of Materials*, 17(3):536–544, 2005.

[90] Sigma-Aldrich. Safety data sheet Ethylphosphonic acid. *https://www.sigmaaldrich.com/catalog/product/aldrich/289876*, 2006. Accessed: 2018-09-19.

[91] Sigma-Aldrich. Safety data sheet Butylphosphonic acid. *https://www.sigmaaldrich.com/catalog/product/aldrich/737933*, 2006. Accessed: 2018-09-26.

[92] Matthew D. Sampson, Jonathan D. Emery, Michael J. Pellin, and Alex B. F. Martinson. Inhibiting Metal Oxide Atomic Layer Deposition: Beyond Zinc Oxide. *ACS Applied Materials & Interfaces*, page acsami.7b01410, 2017.

[93] Hans Gerd Boyen, Gerd Kästle, Klaus Zürn, Thomas Herzog, Frank Weigl, Paul Ziemann, Oliver Mayer, Christine Jerome, Martin Möller, Joachim P. Spatz, Michael G. Garnier, and Peter Oelhafen. A micellar route to ordered arrays of magnetic nanoparticles: From size-selected pure cobalt dots to cobalt-cobalt oxide core-shell systems. *Advanced Functional Materials*, 13(5):359–364, 2003.

[94] Rémi Vallat, Rémy Gassilloud, Brice Eychenne, and Christophe Vallée. Selective deposition of $Ta_2O_5$ by adding plasma etching super-cycles in plasma enhanced atomic layer deposition steps. *Journal of Vacuum Science & Technology A: Vacuum, Surfaces, and Films*, 35(1):01B104, 2017.

[95] Kouhei Kawamura. Method for etching an SiO2 film, 1994.

[96] Dominik Metzler, R. L. Bruce, S. Engelmann, E. A. Joseph, and G. S. Oehrlein. Fluorocarbon assisted atomic layer etching of $SiO_2$ using cyclic $Ar/C_4F_8$ plasma. *Journal of Vacuum Science & Technology A*, 32:020603, 2014.

[97] Robin H. A. Ras, Elina Sahramo, Jari Malm, Janne Raula, and Maarit Karppinen. Blocking the Lateral Film Growth at the Nanoscale in Area-Selective Atomic Layer Deposition. *JACS Communication*, pages 11252–11253, 2008.

# Appendix A

# Precursors and inhibitors

Illustrations of the different precursor and inhibitor molecules used in this researched are given below. Images are downloaded from the webpages of chemical suppliers, Sigma Aldrich (https://www.sigmaaldrich.com/) and Nova-Kem (http://www.nova-kem.com/).

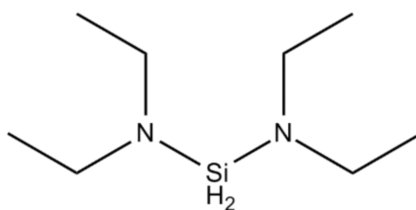


**Figure A.1:** Schematic representation of BDEAS.

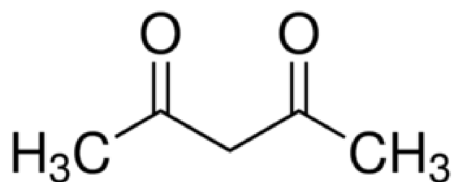


**Figure A.2:** Schematic representation of Hacac.

**Figure A.3:** Schematic representation of TMA.

**Figure A.4:** Schematic representation of vinylphosphonic acid.

# Appendix B

# XPS Si 2p peak reference for $SiO_2$ deposition

Figure B.1 shows the Si 2p peak measured by XPS for 0, 5 and 10 BC cycles of $SiO_2$ ALD. These peaks are given as a reference for uninhibited growth of $SiO_2$.

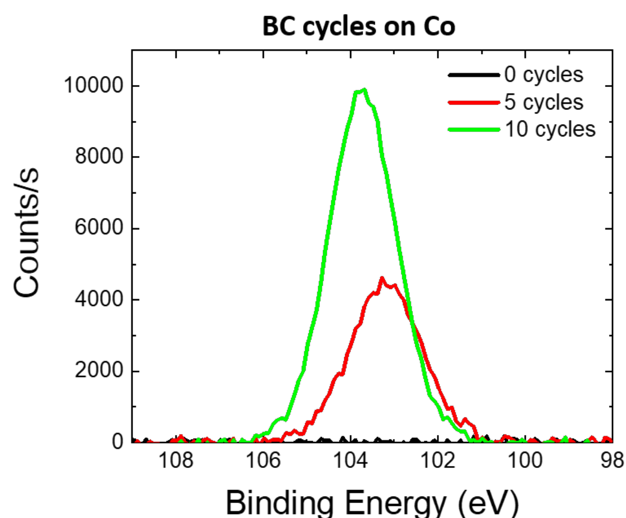


**Figure B.1:** XPS measurement of the Si2p peak for different number of BC-type ALD cycles on $Al_2O_3$. These peaks show a reference for uninhibited $SiO_2$ growth

# Appendix C

# Characterization of the cobalt substrate

In order to characterize the chemical composition of the cobalt substrates used for the experiments, XPS has been used to make a depth profile. The substrate consist of a silicon wafer, on which a cobalt layer of approximately 45 nm thick has been deposited using ALD.

Figure C.1 shows the atomic percentages of species determined using XPS for an increasing etch time. From this data it is visible that the substrate consists of cobalt, with a native oxide layer on top. Also some carbon and nitrogen contaminants are apparent in the film.

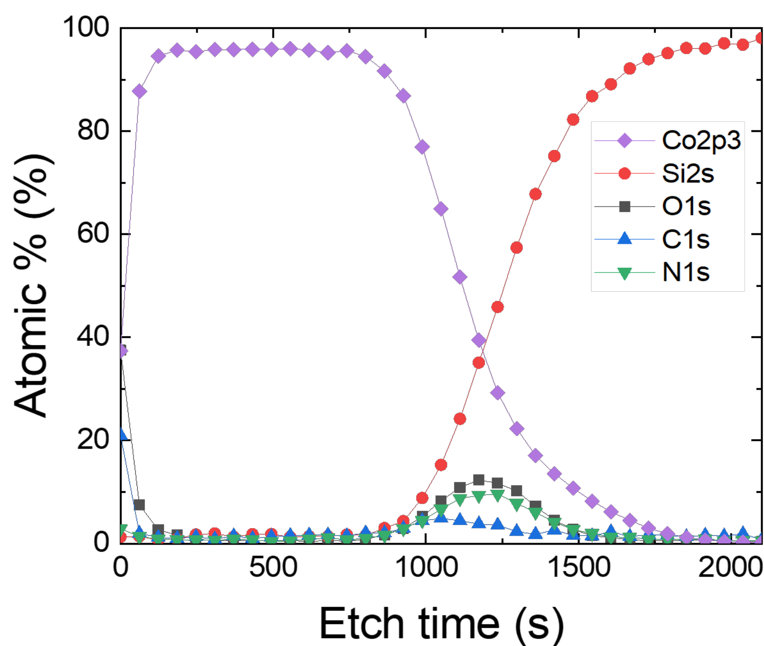


**Figure C.1:** XPS depth profile of the cobalt samples used for the experiments conducted.

# Appendix D

# Saturation of the $O_2$ plasma exposure for ALD of $SiO_2$

Investigation of the saturation for the $O_2$ plasma exposure in the $SiO_2$ ALD process. The $O_2$ plasma exposures was decreased, and the GPC is determined over 30 ALD cycles. The data shows that even for a 1 s $O_2$ plasma, the GPC of $SiO_2$ ALD is unaffected.

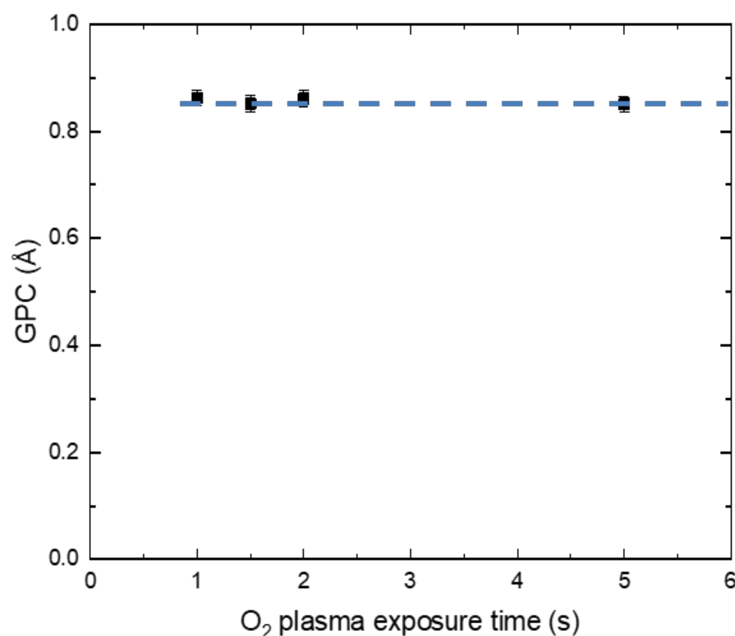


**Figure D.1:** GPC determined over 30 ALD cycles for different $O_2$ plasma exposure times. Even for a 1 second plasma exposure, the GPC remains equal.